

IN-SITU STUDY OF EMERGING METALLICITY AND
MEMORY EFFECT ON ION-BEAM BOMBARDED
STRONTIUM TITANATE SURFACE

BY HEIKO GROSS

A thesis submitted to the
Graduate School—New Brunswick
Rutgers, The State University of New Jersey
in partial fulfillment of the requirements
for the degree of
Master of Science
Graduate Program in Physics and Astronomy

Written under the direction of
Prof. Seongshik Oh
and approved by

New Brunswick, New Jersey

October, 2009

ABSTRACT OF THE THESIS

In-situ study of emerging metallicity and memory effect on ion-beam bombarded strontium titanate surface

by Heiko Gross

Thesis Director: Prof. Seongshik Oh

In this work we present an investigation of the occurrence of conductivity on the surface of SrTiO_3 due to argon ion bombardment. We created a model to describe this process and found that the temperature during the ion milling is a crucial factor for the conductivity. Depending on the temperatures we found surface carrier densities ranging from $n_s = 1.5 \times 10^{18}$ to $2.6 \times 10^{20} \text{ cm}^{-3}$ by just analyzing the conductivity behavior.

Clustering of vacancies goes along with temperature and affects the conductivity significantly. Furthermore we found that ion milling is a gentle way create vacancies because the clustering rate is small compared to annealing samples in high vacuum. The amount of clusters at room temperature was measured to be around 3-4 times higher than at -140°C .

We found that samples with a conducting surface change their resistance over time at room temperature due to the ongoing process of oxygen vacancy clustering. This effect may be suppressed by decreasing the temperature.

The bistable switching behavior in oxygen deficient SrTiO_3 is shown without any additional doping. The vacancy migration is the major mechanism behind this memory effect. Comparing this behavior with annealed samples in high vacuum shows that the therein present amount of vacancy clusters must be much larger and has a negative effect on the bistable switching behavior.

Acknowledgements

I want to express my gratitude to Prof. Seongshik Oh and his group. He was a very competent mentor to me and I want to thank him for enabling me to do such a great work in such a short time. It was a pleasure and an honor for me to work with him because I learned so many new things from him. I also want to thank our post-doc Yong Seung Kim for always having time for me to answer all my questions. Furthermore I want to thank Eliav Edrey, Namrata Bansal and Carlos Chaparro for helping me out and making my stay more enjoyable. Because of them, the atmosphere in the lab was always friendly and casual which made my work there worth while. I want to thank the “Amerika-Programm” of the University of Würzburg and Rutgers University, especially Prof. Ronald Ransome, Shirley Hinds, Prof. Fakher Assaad and the Deutscher Akademischer Austauschdienst for making my stay at Rutgers University possible.

I also want to thank my parents Manfred and Ute and my sister Sandra for always being there for me when I needed them and for giving me the necessary freedom to do my work. I couldn’t have done it without their constant love and support throughout my whole life. I want to thank my girl-friend Anna who always shared my feelings and gave me the strength to do my work every single day. Thanks for accompanying me through this rough year.

Last but not least I want to thank my friends Fabian and Christoph for sharing this wonderful year at Rutgers.

Dedication

To my family.

Table of Contents

Abstract	ii
Acknowledgements	iii
Dedication	iv
List of Tables	viii
List of Figures	ix
1. Introduction	1
2. Theory	2
2.1. Strontium titanate	2
2.1.1. Ionic model	3
2.1.2. Covalent mixing	6
2.2. Conductivity in STO	8
2.2.1. Impurity doping	10
2.2.2. Oxygen Vacancies	10
2.3. Ion milling	12
2.4. Metal-semiconductor junction	12
2.4.1. Schottky Barrier	13
2.4.2. Ohmic contact	15
2.5. Oxygen vacancy diffusion	16
2.5.1. Unlimited vacancy source	17
2.5.2. Limited vacancy source	18
2.6. Ionic conductivity	19

3. Experimental setup	21
3.1. Vacuum chamber	21
3.2. Temperature stage	22
3.2.1. Medium temperature and low oxygen pressure range	23
3.2.2. Low temperature	25
3.2.3. High temperature and high oxygen pressure range	26
3.3. Contact rod	27
3.4. Thermocontroller and power supply	28
3.5. Ion source	29
4. Measurement technique	32
5. Metallicity on STO by Ar⁺ ion beam irradiation	35
5.1. Ion milling energy	35
5.2. Process of oxygen removal	40
5.3. Measurement setup	42
5.4. Conductance development during ion milling	43
5.4.1. Low temperature development	44
5.4.2. Room temperature development	53
5.4.3. High temperature development	56
5.4.4. Comparison between low and high temperature conductance	58
5.4.5. Summary	62
5.5. Time dependent studies	63
5.5.1. Preparation of measurements	64
5.5.2. Results and discussion	64
5.5.3. Summary	69
6. Memory Effect	70
6.1. Sample preparation and measurement	71
6.2. Results and discussion	73

6.2.1. Ion milled sample	73
6.2.2. Annealed sample	77
6.2.3. Summary	82
References	83
Appendix A. Drawings	88

List of Tables

5.1. Ratio of initial kinetic energy of argon to final kinetic energy of Sr, Ti and O	37
5.2. Average Madelung potential and E_{rem} for all three components of STO . .	38

List of Figures

2.1. Perovskite structure of SrTiO_3	3
2.2. Electrostatic potentials of ions on each other	5
2.3. Octahedron cluster of one titanium ion and six oxygen ions	7
2.4. Splitting of orbital levels by covalent overlaps	8
2.5. Schottky barrier formed by a metal and an n-typed doped semiconductor without any bias	13
2.6. Schottky barrier formed by a metal and an n-typed doped semiconductor for forward a reverse bias	15
2.7. Diffusion of oxygen vacancies with constant surface concentration	18
3.1. Sketch of the whole experimental setup	23
3.2. Sample stage	24
3.3. Sample stage with tungsten filament	25
3.4. Silicon heating element	26
3.5. Silicon heating device with titanium pieces	27
3.6. Contact rod	28
3.7. Temperature control setup	29
3.8. Sketch of an end-Hall ion source	30
4.1. 4-probe measurement sketch	33
4.2. Labview program	34
5.1. AFM image of STO	39
5.2. Milling rate over discharge voltage	40
5.3. Illustration of the ion milling process	42
5.4. Decay of vibration energy	45
5.5. Development of <i>steady-state</i>	47

5.6. Saturation of conductance for the discharge currents 1A and 2A	49
5.7. Switching conduction in STO due to changing discharge voltage at low temperature (small difference)	51
5.8. Switching conduction in STO due to changing discharge voltage at low temperature (big difference)	52
5.9. Comparison between different discharge voltages	55
5.10. Conductance during ion milling at 300°C	57
5.11. Sheet resistance as a function of temperature	59
5.12. Comparison of low and high temperature milling measurements with mobility conversion	59
5.13. Influence of oxygen vacancy clustering on the conductance of SrTiO ₃	60
5.14. Comparison of low and high temperature milling measurements with cluster correction	62
5.15. Diffusion and clustering of oxygen vacancies with interval measurement . .	65
5.16. Gaussian distribution of carriers	66
5.17. Diffusion of oxygen vacancies at low temperatures	68
6.1. Setup of memory effect experiment	72
6.2. Measurement of Schottky barrier	74
6.3. Formation of a conductive path on the surface of ion milled and oxidized STO	74
6.4. Conductive state on STO	75
6.5. Memory effect on ion milled STO sample	75
6.6. Multiple hysteresis loops at 100°C	76
6.7. Temperature dependence of the threshold voltage	77
6.8. Comparison of two different Schottky barriers	78
6.9. Formation of a conductive path on the surface of annealed and oxidized STO	78
6.10. Setup for measuring the memory effect on the surface of annealed SrTiO ₃ .	79
6.11. Hysteresis on the surface of vacuum annealed SrTiO ₃	80
6.12. Switching between high conducting and low conducting state	81
A.1. Drawing of stage	88

A.2. Drawing of substrate plate	89
A.3. Drawing of bottom titanium piece	90
A.4. Drawing of top titanium piece	90
A.5. Drawing of bottom ceramic piece	91
A.6. Drawing of top ceramic piece	91

Chapter 1

Introduction

When the first mineral with a perovskite structure was discovered back in 1839, people didn't know what they have really found. In the second half of the 20th century, it was found that there are many materials with this structure and they all show exciting properties. All types of electronic, magnetic and optical characteristics were found to exist in these materials. And not just that, very small deviations from the original structure may have a significant consequences for these properties. Among all these interesting effects, there is one aspect that might be the most crucial one: The perovskite structure is one of the most promising candidate for the replacement of silicon as material in integrated circuits. Many see an end of the silicon era already very soon and that the famous law of Gordon Moor, that the number of transistors per area double every couple of years, will no longer be valid any more. Great effort in research has been done and is still going on in order to get a better understanding of the highly complex process that makes perovskite structures so versatile. There have been already reasonable results that these materials might win the race as the successor of silicon. If they do succeed, it would be a huge breakthrough and a spectacular improvement of computer performances. How long this will take, nobody can say that for sure, but the number of reports of discoveries and improvements of memory devices based on perovskites has been significantly increased in the last years.

In our work we show how one of the most common perovskites, SrTiO_3 , is performing an insulator-metal transition due to loss of oxygen by bombardment of argon ions. We found a model how this mechanism can be explained and how it can be controlled. This process is one of the first steps to show the ability of SrTiO_3 being used as a memory device. Later on, we were able to use the ionic motion within our sample, to create a simple resistive switch that can be seen as a one bit memory.

Chapter 2

Theory

2.1 Strontium titanate

All the measurements in this work are performed on a single type of material: strontium titanate. This material with the chemical formula SrTiO_3 belongs to the family of perovskite oxides with transition metal ions. The perovskite structure is a hot topic these days because it shows a broad spectrum of functional properties. For instance the high-temperature superconductivity in cuprates, the colossal magnetoresistance in manganites and the ferroelectricity in perovskite materials in general are some of the features which make this structure one of the candidates which could replace semiconductors in future electronic devices. The basic chemical formula of a perovskite is ABX_3 ; a subclass of it is the transition metal oxide perovskite with B =a transition metal ion and X =oxygen. A picture of the crystal structure can be seen in figure 2.1. Most of the perovskites have a simple cubic structure with five atoms per unit cell. The transition metal ion is located in the middle of the cube in the center of an octahedron of oxygen anions. The A anion can be found at each corner of the cube. In terms of atomic layers, perovskites consist of BX_2 layers and AX layers.

Strontium Titanate, denoted as STO, is one of the most studied perovskites. It also was the first discovered to exhibit superconductivity [1]. Above 100K it has a cubic structure with a crystal constant of $a = 3.905 \text{ \AA}$; below that temperature it develops a tetragonal shape. It acts as a good insulator, due to the large band gap of $E_{gap} = 3.25 \text{ eV}$ [2]. The most common process to grow epitaxial SrTiO_3 films is by pulsed laser deposition (PLD) [3][4][5]. It has various advantages compared to other techniques, e.g. the ability to grow films in a wide range of pressures [6]. But also rf magnetron sputtering has been recently

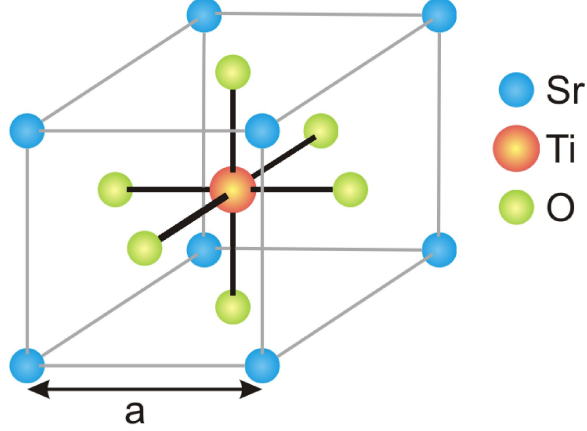


Figure 2.1: Perovskite structure of SrTiO_3 . The size of the ions is not the actual size. The crystal constant is about $a = 3.905 \text{ \AA}$.

successfully used to grow epitaxial films [7]. Due to its diverse special properties it can be used in many applications such as field effect transistors or memory devices [8][9][10].

2.1.1 Ionic model

Looking at the ionic model, the Sr and Ti cations have to donate electrons to the oxygen anions in order to form O^{2-} . The ionic state of the Ti ion is not clear because of the transition metal properties. Assuming charge neutrality and by using the stoichiometric composition of STO one can calculate the ionic configuration of Ti. With three 2-times negative charged oxygen ions ($Q_{\text{O}_2} = -6$) and one 2-times positive charged Sr anion ($Q_{\text{Sr}} = +2$) and the charge equilibrium

$$Q_{\text{O}_2} = Q_{\text{Sr}} + Q_{\text{Ti}}, \quad (2.1)$$

titanium ends up to Ti^{4+} . So the original $[\text{Ar}]3d^24s^2$ configuration changed to just $[\text{Ar}]$. This means titanium loses all its d-electrons and that's why STO is also known as a d^0 oxide with an empty conduction band [11]. In this ionic model every ion has the closed-shell configuration which means SrTiO_3 has insulator properties. Furthermore it is noted, that the two different atomic layers in STO, Sr-O and Ti-O₂, are neutrally charged which is an important property at the interface to other perovskite materials [12].

But there are also other aspects which are important to consider when the electric characteristics are studied; for example, the interaction between the ions due to their electrostatic fields. The electric potential at a site in the lattice is given by

$$V(\vec{x}) = \sum_{\vec{q}} \frac{Q(\vec{q})}{|\vec{q} - \vec{x}|}, \quad (2.2)$$

where \vec{q} are all the lattice points and $Q(\vec{q})$ denotes the ionic charge. The most important electrostatic effect, which is the potential at a specific lattice site due to all other ions in the crystal, is the Madelung potential [13] which is defined by

$$V_M(\vec{x}) = \sum_{\vec{q} \neq \vec{q}_0} \frac{Q(\vec{q})}{|\vec{q} - \vec{x}|} \quad (2.3)$$

for a specific lattice site \vec{q}_0 . In the case of STO, the Madelung potential for a specific oxygen ion $\vec{R}_{O_2}^0$ would be

$$V_M(\vec{R}_{O_2}^0) = \sum_{\vec{R}_{Ti}} \frac{4e}{|\vec{R}_{O_2}^0 - \vec{R}_{Ti}|} + \sum_{\vec{R}_{Sr}} \frac{2e}{|\vec{R}_{O_2}^0 - \vec{R}_{Sr}|} - \sum_{\vec{R}_{O_2} \neq \vec{R}_{O_2}^0} \frac{2e}{|\vec{R}_{O_2}^0 - \vec{R}_{O_2}|}, \quad (2.4)$$

where \vec{R}_{Ti} , \vec{R}_{Sr} and \vec{R}_{O_2} are the ion lattice sites and e is the electron charge. The actual Madelung potential energy of an electron is $V_M(\vec{R}_{O_2}^0) \cdot (-e)$. In figure 2.2b the order of the Madelung potentials are shown. Due to high ionic charges the Madelung potentials in perovskites are very high and also the reason for the stability of the crystal. In the absence of the Madelung potential, the second electron of the oxygen ion would be more likely to bond to titanium and form a Ti^{3+} ion. But since there is this high Madelung potential, the binding energy for a d-electron in STO is effectively +2.6 eV and is therefore unbound.

To study the effect of the electrostatic field on the orbitals near each ion site, the whole potential has to be considered. This means the Madelung potential of an oxygen ion and the potential of this ion itself at that particular spot can easily be described by

$$V(\vec{r}) = -\frac{2e}{|\vec{r} - \vec{R}_{O_2}^0|} + V_M. \quad (2.5)$$

Expanding the potential into spherical harmonics around $\vec{r} = \vec{R}_{O_2}^0$, one can find the first term (monopole) to be Madelung potential itself [14]. This seems reasonable since it is generated by the whole crystal and therefore almost constant in a small range around

$\vec{r} = \vec{R}_{O_2}$. This causes shifts of the electron energies as shown before on the ability of oxygen forming a O^{2-} ion despite the fact that it is not energetically favorable. The higher-order multipoles forces the orbitals to split in different symmetry groups [14] which are still degenerate.

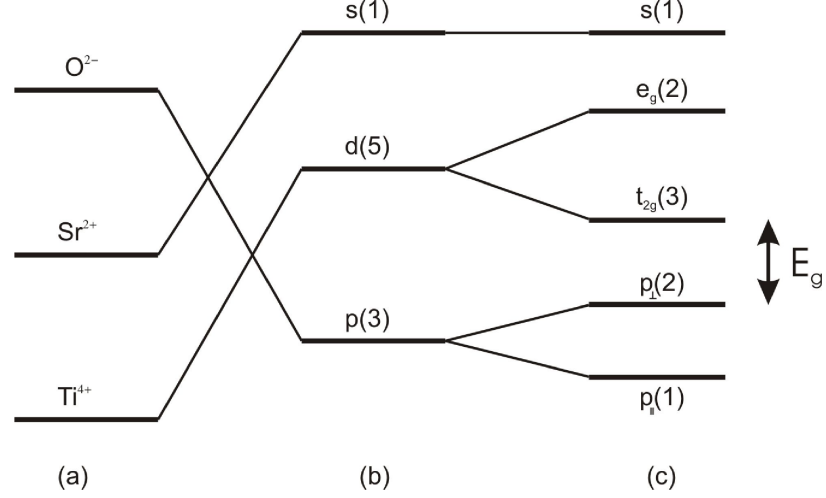


Figure 2.2: The electrostatic potentials of the ions and their influence on each other. The energies of the free ions (a) are shifting due to the Madelung potential (b). These states are degenerate and are splitting because of the electrostatic field of the higher-order multipoles. All the energy magnitudes are not actual size. The energy E_g is almost equal to the energy gap.

As demonstrated in figure 2.2c, the p-orbitals of oxygen, for instance, split into a doubly degenerate state p_{\perp} and a non-degenerate level p_{\parallel} with respect to the axis between the oxygen and the nearest two titanium ions. This can be explained by considering the orientation of the different orbitals relative to the location of the titanium ions. The parallel p-orbital is pointing with two lobes directly towards the positive charged titanium cations which makes it energetically more favorable than the perpendicular orbitals whose lobes are right in the middle between the two cations. The same applies to the d-orbitals of titanium. Due to the cubic electrostatic field the fivefold degenerate d-state splits into the doubly degenerate e_g group with angular symmetry and the threefold degenerate t_{2g} group¹. Here, the orbitals

¹The designations e_g and t_{2g} originate from group symmetry. The e and t denote the degeneracy of two and three, respectively. The g means *gerade* (german for even) and indicates the symmetry to the center. In contrary, the index u means *ungerade* (odd) and indicates antisymmetry. The subscript 2 (1) means that the state is antisymmetric (symmetric) under rotation to a different axis than the principal one.

with the lobes which are not directly pointing towards the oxygen ions, namely t_{2g} orbitals, are energetically more favorable because the anions are negatively charged and repel the lobes.

As mentioned before, stoichiometric STO is a d^0 oxide, so it is insulating because there are no d-state electrons present. Therefore the energy difference between the occupied oxygen p_{\perp} states and the empty t_{2g} orbitals is almost equal to the band gap.

The strontium s-orbital is not affected by the multipole terms because of its spheric symmetry. Since this electron state has a very high energy, compared to the conduction band of STO, it is mostly unoccupied. Also the next lowest orbital of strontium, namely a p-orbital, is energetically much lower than the valance band of STO. This means that strontium has almost no effect on the electric properties. However, in terms of electrostatic potential, strontium has still a big impact due to the ionic charge which contributes to determine the energy of the valence and conduction band. Also the size of the Sr ion is important for the crystal structure to establish the ideal cubic form. But after fixing the crystal structure and ionic potentials, the influence of the strontium ions are more or less negligible on further investigations. Therefore they will be omitted from most of our further studies.

The ionic model is very simple and does not unveil all the properties of STO. The next step would be to investigate the covalent mixing of the ions.

2.1.2 Covalent mixing

Each ion has a set of different electron shells composed of one or more atomic orbitals. The orbitals from the outermost electron shell are the ones which act with other atomic orbitals from different ions. These interactions are called covalent bonds and affect the properties of perovskites significantly. It is mentioned, that the bonding between strontium and oxygen appears to be highly ionic. Conversely, the Ti-O bonds tend to be more covalent [15]. Considering a cluster of one titanium ion and six oxygen ions, as shown in figure 2.3, the wave function for the n-th covalent eigenstate can be described in the form

$$\psi^{(n)}(\vec{r}) = \sum_{\alpha} a_{\alpha}^{(n)} \varphi_{d\alpha}(\vec{r}) + \sum_{\vec{R}_i} \sum_{\beta} b_{i\beta}^{(n)} \varphi_{p\beta}(\vec{r} - \vec{R}_i), \quad (2.6)$$

where α and β denote the orientation of the d and p orbitals, respectively. $a_{\alpha}^{(n)}$ and $b_{i\beta}^{(n)}$ are coefficients for the amplitude of each atomic orbital and \vec{R}_i is the position of the oxygen ion relative to the titanium ion.

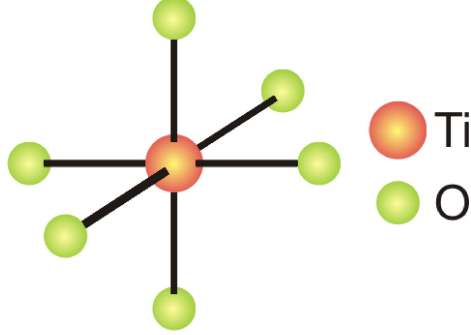


Figure 2.3: Octahedron cluster of one titanium ion and six oxygen ions.

It is noted, that for the ionic model one of the coefficients $a_{\alpha}^{(n)}$ and $b_{i\beta}^{(n)}$ is always zero to create either pure p or pure d wave functions. By looking at the different overlapping combinations one encounters three different combinations: First, the combination of e_g d-orbitals and p_{\parallel} p-orbitals which results in a so-called σ -bond. This is a strong bond and identified by the symmetry along the Ti-O bonding axis. The second mixing is out of t_{2g} d-orbitals with p_{\perp} p-orbitals which creates a π -bond. These bonds are weaker than σ -bonds mostly because their highest electron density is not on the bond axis. The symmetry is a plane which contains the bond axis. The combinations of t_{2g} and p_{\parallel} or e_g and p_{\perp} are vanishing by symmetry.

Due to the overlaps, the ionic states dissolve in 23 states which combine 5 d orbitals and 3-6 p-orbitals which is shown in fig. 2.4. The so-called crystal-field levels e_g and t_{2g} have mostly d-character and are split more than in the ionic model. The p-orbitals are splitting in seven different symmetry groups, most of them are degenerate. Only the same symmetry can lead to a hybridization. The overlap between the e_g and t_{2g} states lead to an electron accumulation on the bond axis. Therefore the positive ion cores are connected by the negative charge in between. This state is called bonding state. If there is a depletion of electrons between the cores, they repel each other, which leads to a so-called anti-bonding state. It was calculated that this bond has 70% p-character [14]. All the other overlaps

don't involve the d-orbital of titanium and therefore do not contribute the Ti-O bonding. This is why these kind of states are called anti-bonding.

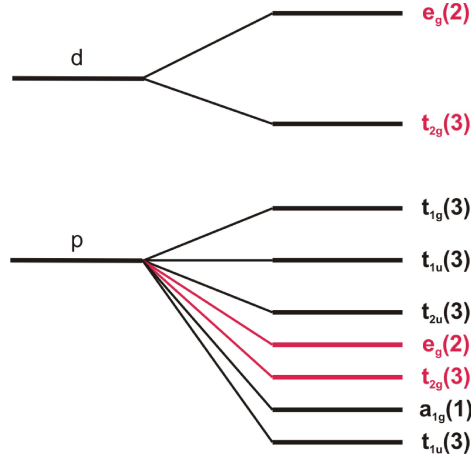


Figure 2.4: Due to the covalent mixing, the p and d-orbitals are split into different symmetry groups. Only the two red marked levels are contributing to the metal-oxygen binding. All the others are considered as non-bonding.

Despite unoccupied d-states in the ionic model, the covalency can make STO conducting due to mixing of filled p-states and empty d-states. In stoichiometric STO has a Fermi energy located right underneath the conduction band. However, the higher the covalent character, the smaller the band gap and vice versa. So the band gap reflects somehow the ionicity of perovskites. The next more complicated model would be the band model where the electron of a titanium ion can be transferred to a second one through an oxygen ion. This leads to the delocalization of the d-electrons which results in the formation of d-electron bands.

2.2 Conductivity in STO

The transition from insulating to conducting state is the primary feature that makes STO so interesting and is also the most studied one. There are basically two different ways to create this conducting phase: First, there is the option of doping STO with impurities in order to change the amount of electrons in the system. It can be compared with the doping of semiconductors, but there are some differences in terms of conduction mechanisms. The second technique of creating conductivity is producing oxygen vacancies, which also

act as impurities. Oxygen vacancies can be introduced by growing STO in oxygen reduced atmosphere, annealing stoichiometric STO at high temperatures while in vacuum or hydrogen atmosphere or bombarding the surface of STO with argon ions. In this chapter we want to give a brief introduction into the emergence of metallicity in STO due to different modification of the chemical composition.

SrTiO₃ undergoes an insulator-metal transition at, compared to other perovskite structures, very low carrier concentrations. We can estimate this critical carrier density by using the Mott criterion [16]

$$a_B n_c^{1/3} \approx 0.2, \quad (2.7)$$

where n_c is the critical electron concentration for which the transition occurs. The Bohr radius a_B is defined by

$$a_B = \frac{4\pi\hbar^2\epsilon}{m^*e^2}, \quad (2.8)$$

with the dielectric permittivity of the material ϵ and the effective electron mass m^* . The meaning of this criterion is rather simple. If the electron density is too low, the overlap of the wave functions is also small, so they can be considered as localized. The mean distance from each other, noted as $n^{-1/3}$, has therefore to drop below a certain threshold in order to make an reasonable overlap possible. The Bohr radius with the material specific parameters ϵ and m^* is a good approximation to estimate the distance of the outermost electron to the core. If the mean distance is small enough, the electron wave functions of two atoms can overlap with each other and conduction is suddenly possible. A numerical approach to this minimum distance is the Mott criterion.

To calculate the critical density we used the dielectric constant $\epsilon = 300\epsilon_0$ which our SrTiO₃ crystal vendor MTI provided. The effective mass is usually in the range of $m^*/m_e = 0.8 - 7.2$ [17]. If oxygen vacancies are used as n-type dopants and the amount of introduced electrons are two. Therefore the concentration is $\approx 6.6 \times 10^{16}$ to $4.8 \times 10^{19} \text{ cm}^{-3}$. These values are consistent with experimental results [18].

2.2.1 Impurity doping

As in semiconductors, n- and p-type doping is also possible in perovskites like STO to increase the conductivity significantly to a metallic state. For example, n-type doping can be done with lanthanum as a replacement for strontium which results in $\text{Sr}_{1-x}\text{La}_x\text{TiO}_3$ and introduces one extra electron per dopant. It has been shown that each La atom contributes with one electron to the conductivity [19]. Also substituting Ti with niobium or vanadium yields $\text{SrTi}_{1-x}\text{Nb}_x\text{O}_3$ or $\text{SrTi}_{1-x}\text{V}_x\text{O}_3$, respectively, and introduces one electron per dopant [19][20]. Due to the different ion radii there are slight changes in the lattice structure which doesn't effect the electrical properties noticeably. The additional electrons force the Fermi energy to shift into the conduction band, consequently giving the system a metallic ground state [21]. The amount of carrier concentration is extremely small for perovskites and metallicity has been reported for concentrations as low as $2.7 \times 10^{17} \frac{1}{\text{cm}^3}$ [18] and $10^{18} \frac{1}{\text{cm}^3}$ [22][23]. This value is several orders lower compared to typical minimum concentrations of other transition metal oxides. Furthermore even superconductivity below $T_C = 0.3 \text{ K}$ has been reported for a carrier concentration above $6.9 \times 10^{18} \frac{1}{\text{cm}^3}$ [20].

P-type doping is also possible. A known candidate for hole doping is scandium as a substitute for titanium yielding $\text{SrTi}_{1-x}\text{Sc}_x\text{O}_3$. Calculations show, that there are basically no changes in the valence band states because these originate mostly from oxygen p-orbitals and therefore remain almost like undoped STO [21]. Conversely the conduction band changes due to different d-states generated by Sc. The p-doping shifts the Fermi energy down to the valence band and evokes the electric conductivity. However, so far p-type metallicity has not been observed yet.

2.2.2 Oxygen Vacancies

Oxygen vacancy emerging in STO is the main issue of this work. Removing oxygen from a lattice site acts as a dopant, because the two electrons of the O^{2-} ion are left in the crystal and oxygen escapes as a neutral atom in order to conserve charge neutrality. Therefore creating an oxygen vacancy, also denoted by V_O , in STO is considered as n-type doping [15]. The two electrons don't necessarily remain in that empty oxygen site, nor lead to formation

of a Ti-Ti bond. They are absorbed by the two nearest adjacent Ti ions and occupy the empty $3d-e_g$ type defect states near the conduction band and become delocalized [15][21]. This shifts the Fermi energy into the conduction band and evokes the conductivity. Since the titanium is a transition metal, the Ti^{4+} ions can change their formal oxidation state to Ti^{3+} [24][25]. This, and the fact that oxygen is missing, leads to slight distortions from the cubic phase to the tetragonal phase [26]. Due to the lack of the negative oxygen ions, which kept the adjacent titanium ions in place, these are now moving away from the vacancy and, conversely, the distance to the next oxygen ion along the Ti- V_O -Ti line decreases [27][21]. The notation for oxygen deficient STO is $SrTiO_{3-\delta}$, where δ denotes the amount of removed oxygen and is usually in the range from 0 to 0.25. According to the ionic model, the highest vacancy concentration in STO would be $\delta = 0.5$. This can be explained by the fact that each oxygen vacancy transforms the oxidation state of two titanium ions from 4+ to 3+. If all titanium ions are reduced to 3+ then the maximum oxygen vacancy concentration is reached. To conserve the charge neutrality, the chemical compound formula has to change. Strontium and titanium have a charge of 5+ which has to be compensated by the two remaining oxygen ions per unit cell, yielding $SrTiO_{2.5}$. It has been found that there is an important difference of oxygen vacancy doping compared to impurity doping in terms of carrier concentration. Lanthanum doped STO for example, obtains one delocalized electron per impurity ion [28] which was also experimentally verified [19]. Whereas oxygen vacancy doped STO is expected to have 2δ electrons available for conduction which is not the case as proved by Hall measurements [29]. Therefore it was found, that for higher concentration of vacancies, the electrons don't remain delocalized. They accumulate into cluster which leads to the formation of localized midgap states within the band gap [30]. It was also suggested, that this is the reason for the blue color of $SrTiO_3$ when the vacancy concentration is very high. So only a part of the doped electrons contribute to conductivity while the rest is being trapped at a titanium ion site. It has been calculated that two vacancies on one titanium ions (also called divacancy) is energetically more favorable than to single vacancies [30]. Furthermore it leads to an increase of the migration energy. Calculations show that the activation energy of the thermal diffusion increases roughly by the factor of two [31][30][32].

2.3 Ion milling

The irradiation of materials by accelerated ions is also called ion milling. This process is usually being used as dry etching in order to remove impurity atoms from a surface. Another field of application is the patterning of shapes, e.g. in semiconductor structures, which is often used in conjunction with photolithography techniques. The types of ions that are used depends on the specific application. It has been known for a long time, that the bombardment of STO by Ar^+ ions creates conductivity on the very surface of the sample [33]. The reason for the utilization of argon is that this gas is inert and therefore doesn't react with SrTiO_3 . Exposing the surface to oxygen recovers the insulating state of STO. Therefore it was found that the ion beam irradiation leads to the removal of oxygen out of STO and the occurrence of vacancies. Further investigations show that the conductivity rises with irradiation time but the increase slows down over time [34]. The thickness of the oxygen deficient layer at the surface also increases with irradiation time which has been detected with cross-sectional TEM images [26]. However, there are a lot of details concerning the behavior of the oxygen deficient layer under different conditions that are not well studied. Therefore we investigated the occurrence of conductivity due to ion milling more accurately just by analyzing conductance.

2.4 Metal-semiconductor junction

In this section we will consider the contact between a metal and a doped semiconductor. We will assume, that the semiconducting material is the same throughout the whole structure and we therefore concentrate only on homojunctions. Using two different materials on each side of a junction usually results in a diode behavior. This is due to a so-called *Schottky barrier* similar to a pn-junction and acts as a rectifier. Under special conditions, this kind of junction is non-rectifying and provides current in both directions. These contacts are also-called *ohmic contacts* and they are used to make low-resistance contacts to semiconducting circuits.

2.4.1 Schottky Barrier

To understand the mechanism of a Schottky barrier one has to consider the energy-band diagram of the two materials after making contact. In fig.2.5 we show a typical diagram of a metal and an n-type doped semiconductor before and after making contact. Since oxygen vacancies in STO are considered as n-type dopants, we will concentrate on this type of doping.

Every material has a work function ϕ , which is the minimum energy needed to remove an electron from the atom. This energy is the difference between the Fermi energy E_f and the vacuum level E_{vac} , which is used as a reference. Each material has a different Fermi energy and therefore a different work function. In our case we assumed that the work function of the metal is higher than the one of the semiconductor, so $\phi_m > \phi_s$. Another important value is the electron affinity χ_s of the semiconductor, which is the energy difference between E_{vac} and the conductance band energy E_c . This energy is equivalent to the energy needed to remove an electron from a negatively charged ion.

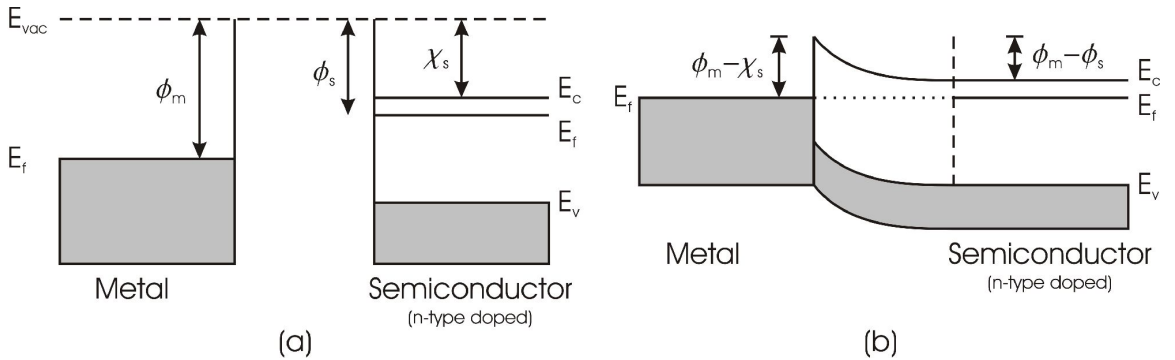


Figure 2.5: Schottky barrier formed by a metal and an n-typed doped semiconductor. Before the intimate contact (a), the Fermi energies are different. Once the contact is formed (b), the Fermi levels have to be the same in thermal equilibrium. Therefore band bending occurs and a Schottky barrier $V_S = \phi_m - \chi_s$ is formed.

Once the two materials make contact, the Fermi energies have to be constant throughout the whole system at thermal equilibrium. The only way this can occur is when charge carriers are moved. Therefore electrons from the semiconductor are moving into the metal until the Fermi energy is equal. This creates a layer in the semiconductor nearby the interface which has less electrons than usual, creating a charge depletion. This depletion

zone corresponds to a barrier, the so-called *Schottky barrier*, which electrons have to overcome in order to maintain a current. The barrier height V_S in the case of n-type doped semiconductor can be simply described by the following equation:

$$eV_S = \phi_m - \chi_s. \quad (2.9)$$

Another way to express the barrier height is by using the built-in potential. This potential is due to the different Fermi energy levels and therefore defined by:

$$eV_{built-in} = \phi_m - \phi_s. \quad (2.10)$$

This leads to the different expression

$$eV_S = eV_{built-in} + (E_c - E_f) \quad (2.11)$$

for the Schottky barrier height, where E_c and E_f are the energies for the conduction band and the Fermi level, respectively. Since the difference between E_f and E_c far away from the interface has to be the same as before the two materials were brought together, band-bending occurs at the interface on the semiconductor in order to match with the metal bands.

This situation can change significantly if the Fermi energies on each side of the interface are changed by an external voltage. Fig. 2.6 shows the band structure for different polarities. Applying a positive bias voltage $V_{forward}$ to the metal with respect to the semiconductor, forces the Fermi level of the semiconductor to increase and reduces the barrier height. We assume that the work function is not affected by the voltage and remains constant. The electrons effectively feel only the potential $V_{built-in} - V_{forward}$ which makes it easier to establish a current once the bias gets reasonable high. Furthermore, the depletion width decreases exponentially with the bias which also contributes to the current. The opposite happens if a positive bias $V_{reverse}$ is applied to the semiconductor with respect to the metal. In that case, the built-in potential gets enhanced by the applied bias due to the decreased Fermi energy of the semiconductor. The barrier height from the metal side to the semiconductor is not effected and the current is still determined by the tunneling current. Also the depletion zone increases which leads to reduction of the tunneling probability.

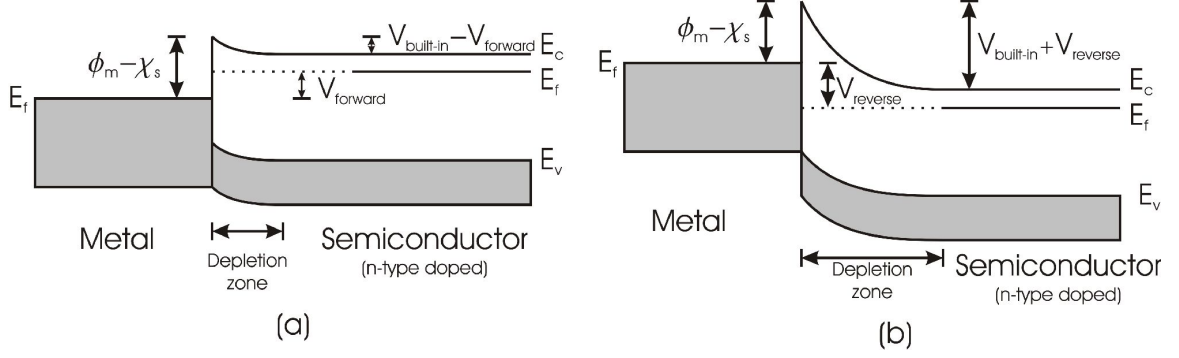


Figure 2.6: Behavior of a Schottky barrier by applying a bias voltage. In case (a), a forward bias is applied which decreases the barrier for electrons flowing from the semiconductor to the metal to $\phi_m - \phi_s - eV_{forward}$. Therefore the current increases. Applying a reverse bias does not affect the barrier for electrons flowing from the metal to the semiconductor, so the current remains very small.

2.4.2 Ohmic contact

To measure the electric properties of a semiconducting device, the current voltage relationship of the contact should be linear in order to obtain reliable data. Ohmic contacts are semiconductor-to-metal contacts without any rectifying capabilities. Ideally, they should provide a low resistance in both directions. Furthermore the current-voltage relation should be linear. The contact resistance for this kind of junction is given by [35]

$$R_C \propto \exp \left[\frac{2\sqrt{\epsilon_s m_n^*}}{\hbar} \cdot \frac{\phi_s}{\sqrt{N_d}} \right] \quad (2.12)$$

There are two ways to achieve an ohmic behavior at a semiconductor-metal junction. The first one is creating an interface with a very small barrier height. Since the barrier height is determined by ϕ_m and χ_s (see eq.(2.9)), these values have to be almost the same in order to reduce the barrier. But this is hard to accomplish because this simple picture does not take surface states into account. These can make significant changes to small barrier heights which results in rectifying contacts. A better way to create an ohmic contact is to increase the doping level of the semiconductor. By increasing the amount of dopant concentration N_d , the depletion width decreases exponentially. Therefore the tunneling current through the barrier is increasing which leads to a small contact resistance as seen in eq.(2.12). In other words, the higher the doping level, the better the ohmic contact.

2.5 Oxygen vacancy diffusion

Studying the effect of oxygen vacancies in STO needs not only knowledge about the amount of vacancies which are created in the crystal, but also about the location of them. Once they occurred, they constantly perform random motions. This is known as diffusion and therefore oxygen vacancies in STO can be treated like molecules in a gas trying to distribute as homogeneously as possible in the crystal. To understand these motions, we will give a brief introduction of diffusion theory.

We start by assuming an isotropic medium with a given non-uniform distribution of substance $c(\vec{r}, t)$ as a function of space and time. For simplification we concentrate only on one dimension. Considering, that no diffusion occurs, the distribution would not change with time, so

$$c(\vec{r}, 0) = c(\vec{r}, t > 0). \quad (2.13)$$

The theory of diffusion is based on the hypotheses, that the amount of diffusing substance through a unit area is proportional to the concentration gradient measured normal to this section, so

$$F = -D \frac{\partial c(\vec{r}, t)}{\partial t} \quad (2.14)$$

where F is the amount of diffused substance per unit area and D is the diffusion coefficient. The negative sign is because the direction of the diffusion is the opposite of the concentration gradient. Considering a stream of substance through a volume due to a concentration gradient, one can derive a time and space dependent differential equation [36], known as Fick's second law, that is

$$\frac{\partial c(\vec{r}, t)}{\partial t} = -D \Delta c(\vec{r}, t). \quad (2.15)$$

Simplified into one dimension yields

$$\frac{\partial c(z, t)}{\partial t} = -D \frac{\partial^2 c(z, t)}{\partial z^2}. \quad (2.16)$$

The diffusion coefficient is temperature dependent and can be described by

$$D(T) = D_0 \cdot e^{-\frac{E_a}{kT}}, \quad (2.17)$$

where D_0 is the maximum diffusion and E_a is the activation energy determined by the material. This energy can be seen in a simple model as the minimum kinetic energy needed to

switch from one lattice site to another. Note that the diffusion coefficient scales exponentially with temperature and that is why diffusion is so important for STO, since creating vacancies with one of the methods mentioned earlier may come along with higher temperatures and therefore has a major impact on the shape of the oxygen deficient region. In all following calculations we are going to use the diffusion coefficient [37]

$$D = 4.71 \times 10^{-3} \exp\left(-\frac{590 \text{ eV}}{kT}\right) \frac{\text{cm}^2}{\text{s}} \quad (2.18)$$

These numbers are only valid for diffusion of single vacancies. In case of divacancies (two vacancies at one titanium ion), the activation energy is roughly two times higher [30].

2.5.1 Unlimited vacancy source

We now want to solve eq.(2.15) for a semi-infinite sample of STO in the case of infinite-source diffusion. This means that the concentration of oxygen vacancies on the surface of one side of the sample is fixed, while the rest of the STO is stoichiometric. We will assume, that this picture applies for the diffusion process during the ion milling, when the change of conductivity is small. Therefore the concentration of mobile vacancies (that means not clustered) remains constant on the surface. The solution has to satisfy the boundary condition

$$c(0, t > 0) = c_0 = \text{const}, \quad (2.19)$$

and the initial condition

$$c(z > 0, 0) = 0, \quad (2.20)$$

where z is the direction into the sample perpendicular to the surface. Solving the differential equation yields the solution [36]

$$c(z, t) = c_0 \operatorname{erfc}\left(\frac{z}{2\sqrt{Dt}}\right), \quad (2.21)$$

which contains the complementary error function defined by

$$\operatorname{erfc}(z) = 1 - \operatorname{erf}(z) = 1 - \frac{2}{\pi} \int_z^\infty e^{-t^2} dt. \quad (2.22)$$

By using eq.(2.21) we can estimate at which temperature and after what time the vacancy concentration in a certain depth in the sample gets reasonable high to form a conducting

layer. In figure 2.7 the concentration of oxygen vacancies of a thin STO sample is shown after 10 min for different temperatures. Note, that since we are assuming that the boundary condition is a semi-infinite medium, the predicted diffusion is only valid until the vacancy concentration at the back of the sample is not negligible small.

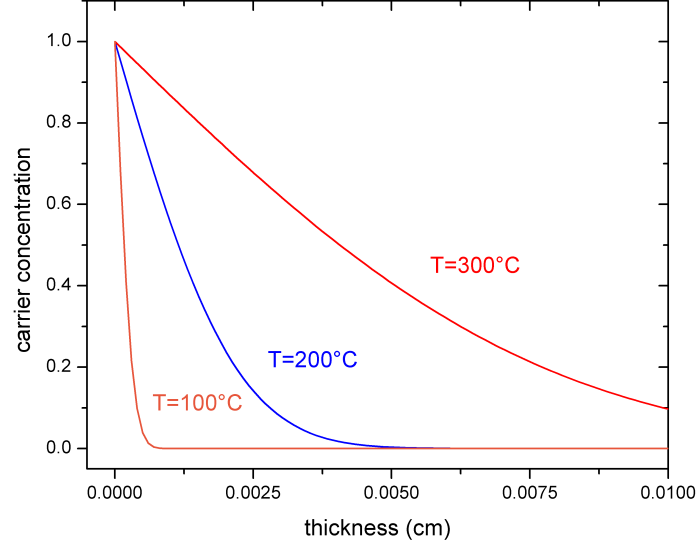


Figure 2.7: Diffusion of oxygen vacancies with constant surface concentration after 10 min for different temperatures. The diffusion depth depends exponentially on the temperature.

2.5.2 Limited vacancy source

For the case, that at a certain time the ion milling process stops, the vacancy concentration on the surface will not remain constant. The process of creating oxygen vacancies ended, so the total amount of vacancies remains constant. When starting from a fresh STO sample and ion milling below 100°C, most of the vacancies are located near the surface. The thickness of the oxygen vacant layer is thin compared to the sample thickness, we will assume that the initial vacancy distribution is zero for the whole sample except for the surface plane. So the initial condition can be expressed as

$$c(z > 0, 0) = 0 \quad (2.23)$$

and the boundary condition, for a semi-infinite crystal, by

$$c(z \rightarrow \infty, t) = 0. \quad (2.24)$$

Using these constraints to solve eq. 2.15 leads to the solution [36]

$$c(z, t) = \frac{A}{\sqrt{t}} e^{-\frac{z^2}{4Dt}}, \quad (2.25)$$

where A is some arbitrary constant. By evaluating the amount of oxygen vacancies V_{tot} in the whole substrate, which is defined by

$$V_{tot} = \int_0^{\infty} c(z, t) dz, \quad (2.26)$$

one can see that this is a constant. Executing the integral leads to

$$V_{tot} = A\sqrt{\pi D}, \quad (2.27)$$

which is independent of z. Using this as a normalization for our solution of the differential equation yields

$$c(z, t) = \frac{V_{tot}}{\sqrt{\pi Dt}} e^{-\frac{z^2}{4Dt}}. \quad (2.28)$$

The shape of the curve equals the Gaussian distribution. At the beginning, all the vacancies are concentrated in one thin layer at $z = 0$. This initial concentration drops very fast and the peak starts to broaden over time. It is noted, that at $z=0$, the vacancy concentration drops with \sqrt{t} and the exponential term vanishes, so

$$c(z = 0, t) = \frac{V_{tot}}{\sqrt{\pi Dt}}. \quad (2.29)$$

2.6 Ionic conductivity

Diffusion of oxygen is a very important feature in SrTiO_3 . As we pointed out in the previous section, temperature has a major impact on the distribution of oxygen vacancies, but this is not the only factor that has to be considered. Since an oxygen ion is charged two times negative, the corresponding oxygen vacancy (hole) has to have the opposite charge, so V_O^{2+} . The diffusion constant of oxygen is very high compared to strontium or titanium. So they can be easily moved not only by temperature, but also by applying an electric field. These mechanisms are basically the same, the difference is just the driving force of the ion motion. In the case of temperature, it is the concentration gradient, but in the case of electric field, it is the electric force. The fact that oxygen ions are doubly charged enhances this behavior.

In case of thermal equilibrium, a steady-state can be evoked by applying an electric field that compensates the flux of ions due to a concentration gradient. This can be expressed by

$$v \cdot c(z) = D \frac{\partial c(z)}{\partial z}, \quad (2.30)$$

where v is the velocity of the ions due to the electric field that is necessary to equalize the flux of the concentration gradient [38]. Solving this equation, under the condition of thermal equilibrium, leads to the Nernst-Einstein relation

$$D = \mu k_B T, \quad (2.31)$$

with the mobility $\mu = \frac{v}{F}$ of the oxygen ions, where F is the force on the ions due to the electric field E . Using Ohms law $j = \sigma E$, where j is the current of the ions, and the force $F = qE$, with q is the ionic charge, one can find the equation for the ionic conductivity

$$\sigma_{ion} = \frac{D n e^2}{k_B T}. \quad (2.32)$$

So therefore we can say, that diffusion of charged ions due to an electric field can be expressed as ionic conductivity. It can be compared to electrical current which is usually much higher because of a much bigger diffusion coefficient, owing to a greater mobility, and a higher carrier concentration. Therefore, ionic conductivity is usually just a small fraction of the total conduction and can be considered as negligible. In case of STO, things are a little bit different, because oxygen ions are, on the one hand, the particles which determine the electrical conductivity in a certain area, but, on the other hand, are charged and can be moved by electric fields. This means, electric conductivity can be modified by a voltage which is the necessary requirement to build memory resistors.

Chapter 3

Experimental setup

To execute our experiments we customized a simple high-vacuum chamber with a few upgrades which enabled us to perform very unique measurements. The main purpose is to make electrical in-situ measurements which means making contacts to the sample, running a current, reading a voltage and remove the contacts without leaving a trace on the substrate. This whole procedure needs to be performed in high-vacuum atmosphere and at substrate temperatures reaching from -200°C to 800°C . In addition, all the measurements should also be possible at high partial oxygen pressures up to atmosphere pressure which requires special heating capabilities. All these conditions require specialized tools which were designed for these kinds of measurements. The experimental setup contains the following components:

- vacuum chamber
- temperature stage
- ion source
- contact rod
- thermocontroller/power supply

The drawings of the customized parts can be found in appendix [A](#).

3.1 Vacuum chamber

The chamber is the place where all the measurements and ion beam irradiations are performed. A simplified sketch can be seen in figure [3.1](#). Equipped with a turbo pump the

minimum base pressure that can be reached is $p_{base} = 10^{-7}$ Torr. The pressure reading is accomplished by a standard ion-gauge. To introduce oxygen, a needle valve is attached for fine-tuning adjustments of the gas pressure down to 10^{-6} Torr. There are several feedthroughs for various jobs. On the top side there are two 1/4" tubes for supplying the sample stage with cooling water or liquid nitrogen. To power the heating of the temperature stage an electrical power feedthrough rated up to 15 A is located at the top of the chamber and a thermocouple Type K feedthrough for temperature measurements which also can be found also on the top. Furthermore there is a rotary feedthrough to control the stage shutter. The shutter is needed to cover the sample while the ion beam is adjusted and to time the exposure more accurate. On the bottom are the feedthroughs which are needed to perform electrical measurements. That is one linear motion feedthrough to guide the contact rod and an electrical multipin feedthrough to pass the signals out of the chamber.

3.2 Temperature stage

The requirements of the temperature stage are to keep the sample on an electrical insulating surface and heat it up to 800 °C or cool it down to -200 °C. The whole stage is produced out of OFHC (oxygen free high conductivity) copper to keep the outgasing rate at higher temperatures as low as possible. The stage has a small closed water panel, which is separated from the vacuum and a big opening, which is in vacuum and can be seen in figure 3.2. The water panel used to bear the cooling liquid, which is supplied by two tubes coming from the top of the chamber. The water panel was sealed by using a vacuum brazing technique. Figure 3.2(a) shows the stage with both tubes, which are also holding the whole stage in place. The opening at the bottom of the stage is where the heating takes place and where the SrTiO₃ sample is located. Therefore, there are two moly rods which are insulated electrically through the stage and provide the necessary power for the heating. Molybdenum was chosen because of the good electric conduction properties and the low outgasing rate at higher temperatures. Most of the electrically conducting metal parts on that stage are made of moly. There are three different configurations at the bottom of the stage depending in which temperature or oxygen pressure range the actual measurements take place.

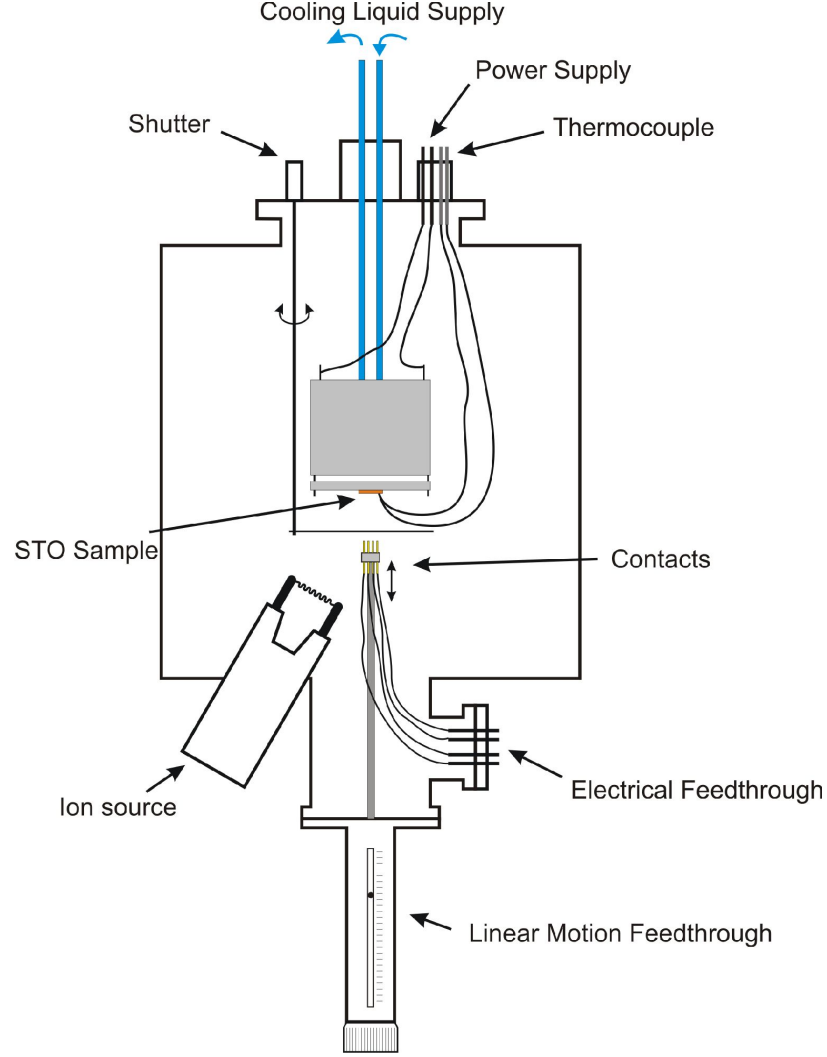


Figure 3.1: Sketch of the whole experimental setup. The stage is located in the center of the chamber. Heating power supply cable, cooling liquid and thermocouple wire are coming from the top. The sample is mounted underneath it and so its surface is exposed to the bottom of the chamber. That is where the ion source and the contact rod is located. The rod can move vertically to touch the sample with its four contacts.

3.2.1 Medium temperature and low oxygen pressure range

If the desired temperature range is between room temperature and around 350°C , we simply used a tungsten filament as heater. Starting with a tungsten wire with a diameter of $200\mu\text{m}$, we coiled up a length of 20 cm and placed it in the opening. The ends of the tungsten filament are attached at the two moly rods by squeezing them between two moly nuts which can be seen in figure 3.3. The sample is placed on a copper plate which is

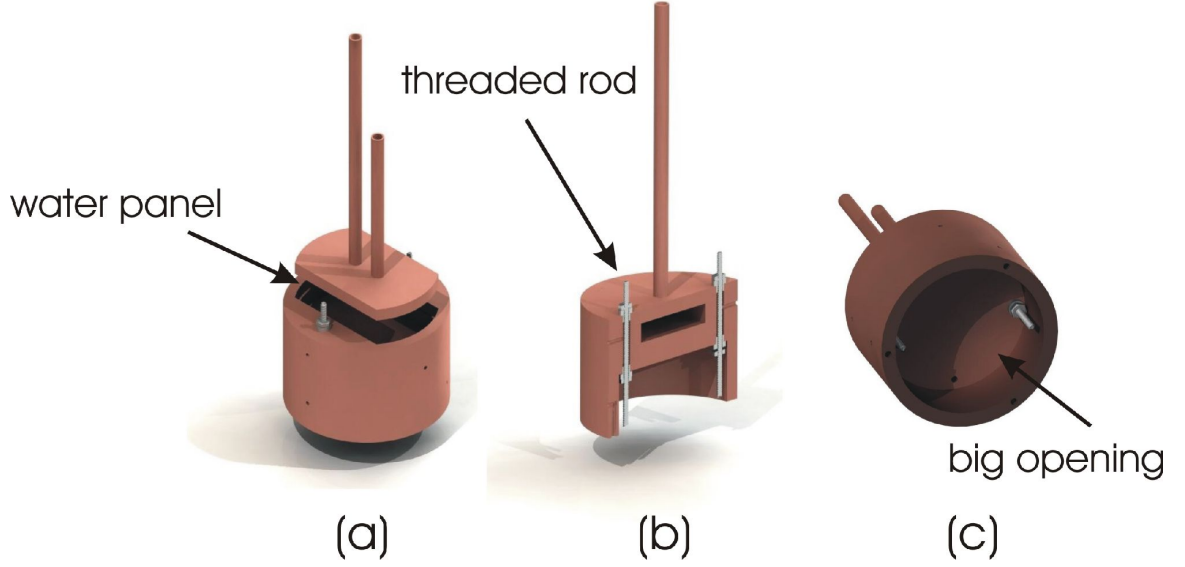


Figure 3.2: Different angles of the sample stage. Fig.(a) shows the cooling supply tubes separated from the rest to show the water panel. In the profile view of the stage in fig.(b), the threaded rods are clearly visible. They are electrically insulated by ceramic bushings. The big opening at the bottom can be seen in fig.(c).

mounted on three moly studs underneath the opening. The heat, which is radiated by the tungsten filament, is absorbed by the copper plate leading to the above mentioned temperature. The rest of the stage remains at lower temperatures by running cooling water through the water panel, in order to reduce the thermal stress on the brazing. Therefore there is a small gap between the stage and the copper plate. This heat dissipation through the moly studs is negligible small, which means that the only heat loss in the copper plate is by radiation. The sample is mounted on the copper plate by using silver paint as glue. This makes a good thermal contact but also electrical contact. Since the stage is grounded we have to prevent current running through the ground in order to perform accurate resistance measurements on the sample. Therefore we used a sapphire plate with a thickness of about 0.4 mm in between the copper and the STO sample. Sapphire is a very good insulator and has moderate thermal conduction properties above room temperature. Below room temperature the thermal conductivity increases. The temperature on the very surface is an important value for all of our experiments and has to be measured very precisely. Therefore

we attached the thermocouple tip in the edge of the SrTiO_3 surface and fixed it with a drop of silver paint. This way we can obtain the sample surface temperature with high accuracy.

This configuration can only be used in high vacuum because the thin tungsten wire can't persist any oxygen pressure.

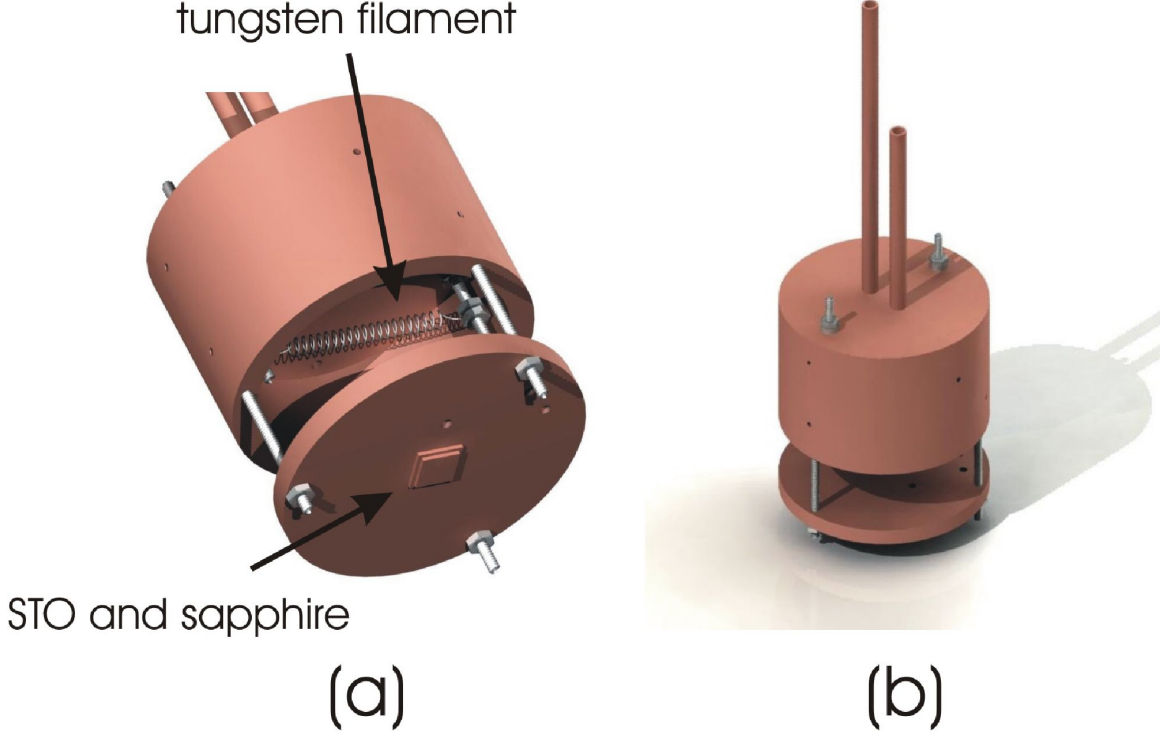


Figure 3.3: Sample stage with a tungsten filament mounted is shown in fig.(a). The sample plate is mounted on three moly studs and keeps the STO with sapphire in between. Fig.(b) shows the hole stage in vertical view. The actual distance between the stage and the sample plate is usually just 1 – 2 mm.

3.2.2 Low temperature

For measurements down to liquid nitrogen temperatures we used the same configuration as for the medium temperature setup, with the modification that the copper plate makes a tight contact to the stage. Therefore, the whole stage can be cooled down by introducing LN_2 into the water panel. Because of the good thermal contact between the copper plate and the stage, the temperature on the surface of the sample reaches around -200°C . In combination with a tungsten filament, it is possible to maintain the sample at temperatures

between -200°C and room temperature. It is noted, that using cooling water is also a possibility to stay at ambient temperatures.

3.2.3 High temperature and high oxygen pressure range

Reaching temperatures up to around 800°C requires a more sophisticated heating mechanism. At high oxygen pressures tungsten filaments can't be used because at a certain amount of oxygen the filament will get oxidized and break due to the high temperature. That's why we used a silicon wafer as heating device and have chosen to mount the sample directly on the wafer. Since the heat is transferred by conduction and no longer by radiation the temperature of the silicon can be much lower compared to tungsten. The silicon wafer is highly doped with boron with a resistivity of $0.01\Omega/\text{cm}$. Cutting the wafer in into a rectangular shape with the dimensions of $1\times 3\text{cm}$ we obtain a resistance range similar to the one of the tungsten filament. The desired temperature on top of our sample is around

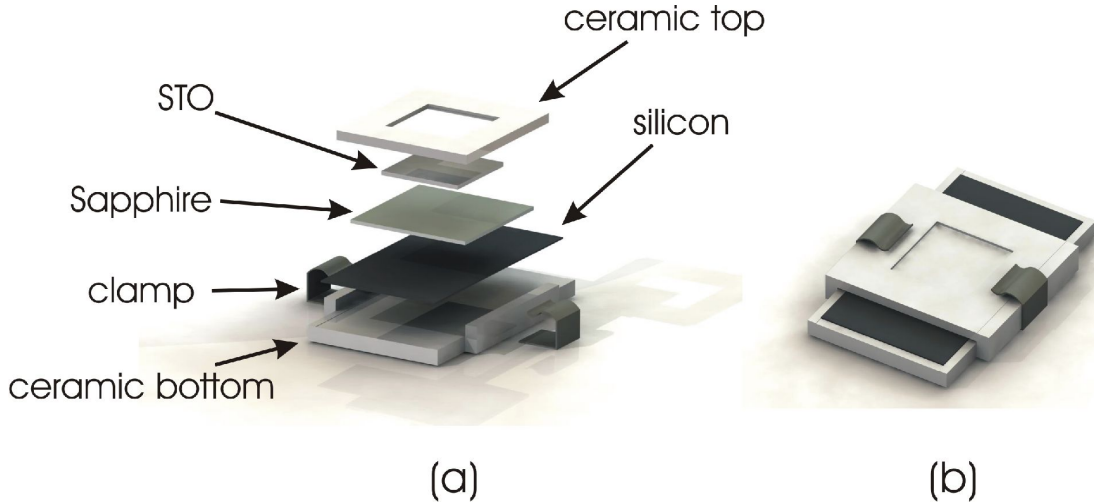


Figure 3.4: The composition of the different layers of the silicon heating device is shown in fig.(a). The STO sample is electrical insulated by the silicon through a sapphire plate. All three pieces are sandwiched by high temperature ceramic. The top ceramic piece is just a frame to increase the exposed surface of STO. Fig.(b) shows the device squeezed by two tantalum clamps.

700°C , which means that the silicon will be at least a couple of hundred $^{\circ}\text{C}$ higher. This is because the sapphire plate between the silicon and the sample which is needed for electrical

insulation is not a good thermal conductor at higher temperatures. There is also a temperature gradient between the bottom and the top surface of STO. Furthermore the use of silver paint as glue is no longer possible because above 650°C oxidation of silver occurs which reduces the sticky properties and the thermal conduction abilities of the paint instantly. Therefore we used two pieces of high-temperature ceramic to combine all three parts: STO as sample, sapphire as an electric insulator and silicon as a heater. Fig. 3.4 shows the stack of components before and after the assembly, respectively. To hold everything together, two clamps out of tantalum are attached at the sides to ensure a tight contact. Tantalum is suitable material for this kind of purpose, because it is exposed to high temperatures and has to have a low outgasing rate. Furthermore it remains springy capabilities in these temperature regimes. This compact heating device is squeezed between two titanium pieces on each side (fig. 3.5) which have holes to mount everything in the big opening of the stage on the moly rods. An image as the silicon heater is placed in the stage can be seen in fig. 3.5(c).

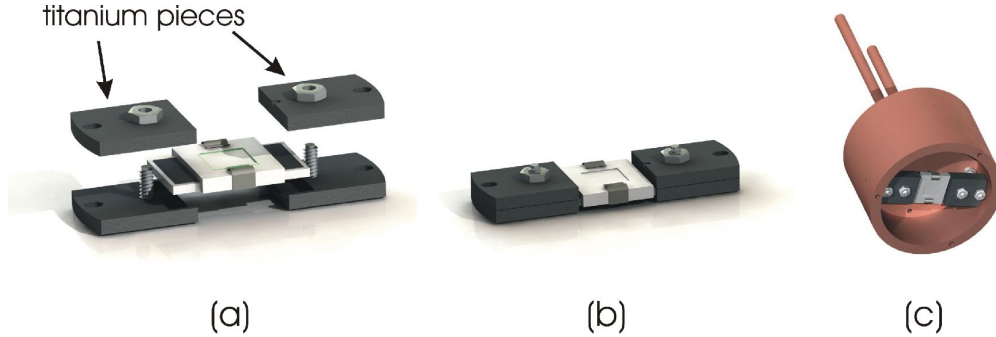


Figure 3.5: The silicon wafer on ceramic is squeezed between two titanium pieces, see fig.(a) and (b), in order to make it possible to mount in the stage. The whole ceramic heater in its stage can be seen in fig.(c).

3.3 Contact rod

Doing in-situ resistance measurements means making electrical contact with the sample in the vacuum. In our case, we have to be able to remove the contact without changing the sample. Therefore we used spring contacts aligned in a straight line and fixed in a ceramic block which assures electrical insulation of each contact. The spring contacts are gold coated

and have a diameter of 0.66 mm with a round tip. The distance between each contact is 2 mm. Due to the springs we are capable of making a soft contact without damaging the surface of the sample. This is an important criterion because the conducting layer in our case can be as thin as 100 nm. The ceramic piece is mounted on a rod which is attached to the linear motion feedthrough located at the bottom of the vacuum chamber. Each spring contact is connected through a polyimide coated copper wire to the multipin feedthrough also located at the bottom of the vacuum chamber. Due to the tungsten filament of the ion source, the whole vacuum chamber gets tungsten coated. This is a problem, because this coat can get thick enough to establish an electrical connection from one contact to the other. Therefore the spring contacts are shielded by a metal frame, which blocks most of the direct tungsten deposition.

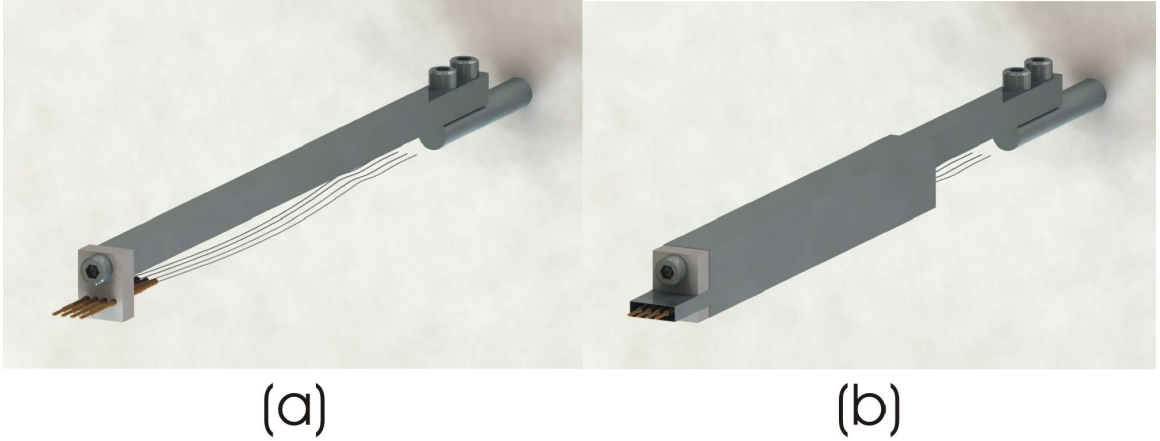


Figure 3.6: In fig.(a) the contact rod is shown without any shields. At the front, the four spring contacts are mounted in a line on a ceramic block. Fig.(b) shows the contact rod with shields to prevent any short-circuit between each contact due to the constant tungsten coating during the ion milling.

3.4 Thermocontroller and power supply

To monitor the temperature we used a Eurotherm 2408 Thermo Controller to read out the signal of the Type K thermocouple. This device has a PID controller which is connected to the Sorensen DLM 600 W power supply with a maximum voltage of 40 V and a maximum current of 15 A. A sketch of the temperature control setup can be found in fig.3.7. When supplying the silicon heating, the preferred sourcing is current driven because the resistance

of the silicon wafer changes significant with temperature. When the intrinsic region of the doped silicon is reached the resistance drops with temperature instead of increasing. With a voltage driven sourcing it is impossible to maintain a stable current beyond this temperature. When using the tungsten filament as heating device both, current and voltage driven sourcing, are applicable because of the monotone increasing resistance.

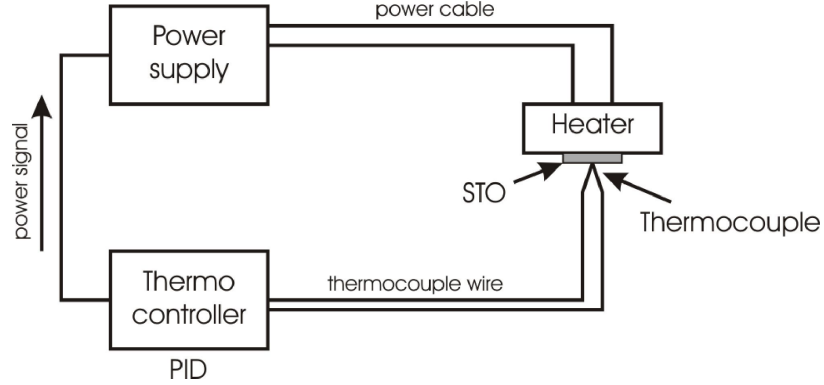


Figure 3.7: Sketch of the temperature control setup. The thermocontroller is adjusting the power signal of the heater according to the temperature and its change over time. The internal PID settings are calculating the necessary power.

3.5 Ion source

To produce an ion beam we used the EH200 ion source by Kaufman and Robinson. This source is without a grid and designed for low ion energy and high currents. These kind of sources are sometimes also called end-Hall ions source, which comes from the fact that the beam leaves at the end of the magnetic field [39]. There are several advantages compared to gridded ion sources. The most important one is that low energy ions tend to damage the etched surface less than high energy ions. So for sensitive applications it is better to use lower energetic ions which can not be achieved with gridded sources. Another aspect are the low costs and the easy maintenance efforts. Also there are only three control parameters you have to take care of compared to five with a gridded source. For a general understanding we explain the basic operating principle of an ion source [40]. In figure 3.8 we present a sketch to make the following easier. Due to the high cathode current I_C the cathode filament is glowing and emits electrons. These are flowing to the grounded ion source which can be read

as an emission current I_E . By applying a discharge voltage V_D between the ion source and the anode, the electrons of the cathode are accelerated towards the anode. The magnetic field of a permanent magnet prevents them from directly hitting the anode. The introduced working gas argon is bombarded near the anode by the energetic electrons which results in ions. The advantage of argon gas is the fact that it is a noble gas and does not chemically react with other molecules. Since the amount of electrons and ions is approximately equal,

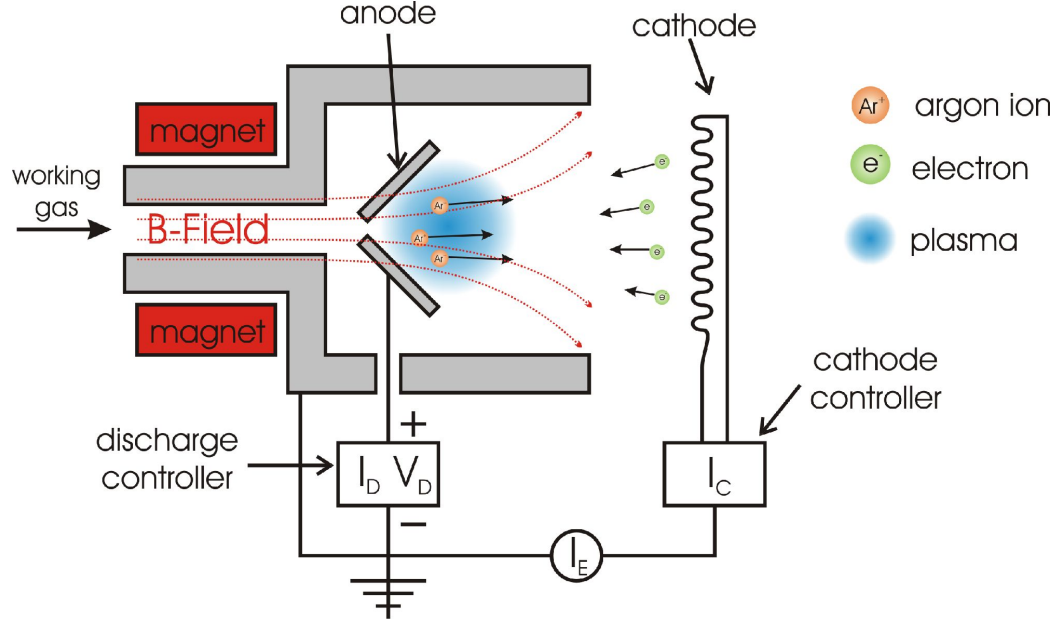


Figure 3.8: Sketch of an end-Hall ion source. Electrons are emitted by the cathode (I_E) and accelerated towards the anode due to the discharge voltage V_D . Inhomogeneous magnetic field increases the probability of hitting and ionizing the argon atoms (working gas) and creating a plasma. Potential difference due to interactions of the magnetic field with the electrons accelerate the argon ions towards the cathode.

a neutral plasma occurs in the anode region. The movement of the electrons within the magnetic field generates circular motions which is called a Hall-Current. The interaction of the electrons with the non-uniform magnetic field produces an electric field with the same direction as the magnetic field in order to maintain a uniform plasma density. This potential difference is the biggest contribution for the acceleration of the argon ions out of the plasma.

The ion beam has an energy of about 60 – 70 % of V_D and diverges to an angle of about 45° . With a fixed discharge current I_D the discharge voltage can be set by adjusting the

argon gas pressure. The higher the pressure the lower the voltage. The effective ion current is about 25 % of I_D .

Chapter 4

Measurement technique

To get reliable values we used the four-point measurement technique to obtain the sheet resistance of the surface of the sample. This technique is very convenient to get rid of any contact resistance which is very high in our case because our contact area has only a diameter of a few micrometer.

The reason why the 4-point measurement is a lot more accurate than using only two leads is because it allows us to apply current and read voltage at the same time over different pairs of wires. Fig. 4.1 shows how two of the four contacts are used to inject a current and the other two are utilized to read the voltage. The measured voltage V_{4P} is not affected by the contact resistance when the input impedance is sufficient big, so the current flowing through the voltmeter is negligible small. Therefore the voltage drop at the two voltage leads is also small and the main voltage drop occurs in the film (parallel circuit). The contact resistance of current leads is not important because the current is constant in a serial circuit.

The sheet resistance is used to characterize the resistance of very thin films of uniform thickness when the current is flowing parallel to the film. It is defined as

$$R_S = \frac{\rho}{t}, \quad (4.1)$$

where t is the thickness of the film and ρ the resistivity. The unit is the same as for the resistance which can be shown by expressing the resistance R in terms of R_S :

$$R = \rho \frac{l}{t \cdot w} = \frac{\rho}{t} \frac{l}{w} = R_S \frac{l}{w} \quad (4.2)$$

where w is the width and l the length of the film. To distinguish the sheet resistance from the usual resistance it is also common to use the unit $\frac{\Omega}{\square}$. That is because the resistance of a square shaped, thin layer of material measured two opposite edges is independent of width

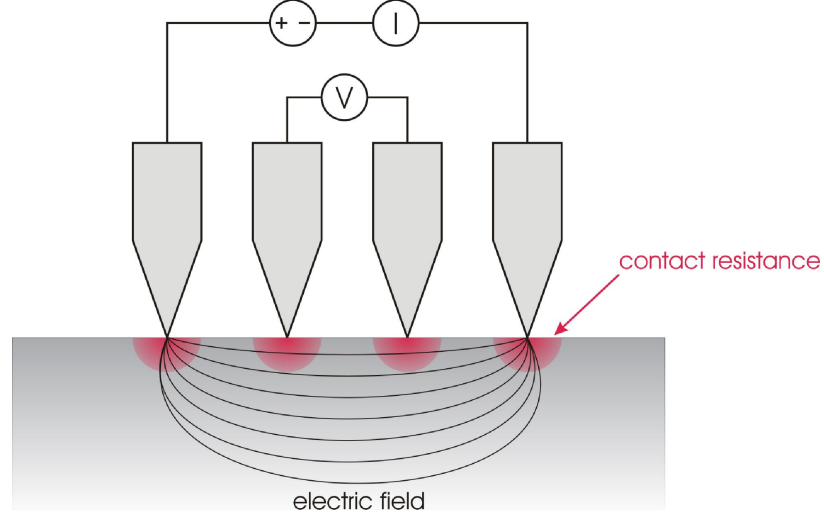


Figure 4.1: Sketch of the 4-point measurement to avoid the influence of the contact resistance. Because the current through the voltmeter is so tiny (very high impedance), there is almost no current flowing through the voltage probes. Therefore the contact resistance does not affect the voltage reading.

or length, as long as they are equal. For a semi-infinite extended material, the conductivity can be directly measured with the a 4-point probe. In can be shown, that the resistivity for this case can be described by [41]

$$\rho = 2\pi s F \frac{V}{I}, \quad (4.3)$$

where s distance between the equally spaced probes, which are aligned in a straight line. Furthermore I is the current injected by the outer two leads and V is the voltage measured by the leads in the middle. The factor F denotes the correction for an arbitrary shaped sample. This correction factor is usually a product out of multiple independent factors like sample thickness, extension in lateral direction or location of the 4-point probe array with respect to the edges of the sample. By approximating that the sample is very thin and that the thickness is also smaller than the half of the lead distance s, the equation for the resistivity changes to

$$\rho = \frac{\pi}{\ln 2} t \frac{V}{I}, \quad (4.4)$$

with t as sample thickness. Now it is possible to measure the sheet resistance of the STO sample, by plugging equ.4.4 into equ.4.1:

$$R_S = \frac{\pi}{\ln 2} \frac{V}{I} \quad (4.5)$$

This formula, however, is subject to another correction in terms of sample shape. In our case, the sample is a perfect square with the dimensions $a = d = 10$ mm. With this information and the spacing of the contacts, one can look up the correction factor in a table [42][43], which leads to the final equation

$$R_S = 3.5098 \frac{V}{I} \quad (4.6)$$

For all the sourcing and sensing operations we used a KEITHLEY 2636A sourcemeter with two channels. Channel A was utilized to establish the current and to read out the 2-point voltage V_{2P} , the purpose of Channel B was to read the 4-point voltage V_{4P} . By monitoring both, V_{2P} and V_{4P} , and taking their relative behavior into account, one can collect even more information about the electrical properties of the measured sample. All the electrical measurements were performed with a self-made LabView program using the GPIB protocol. An image of the program interface can be seen in fig. 4.2. When measuring

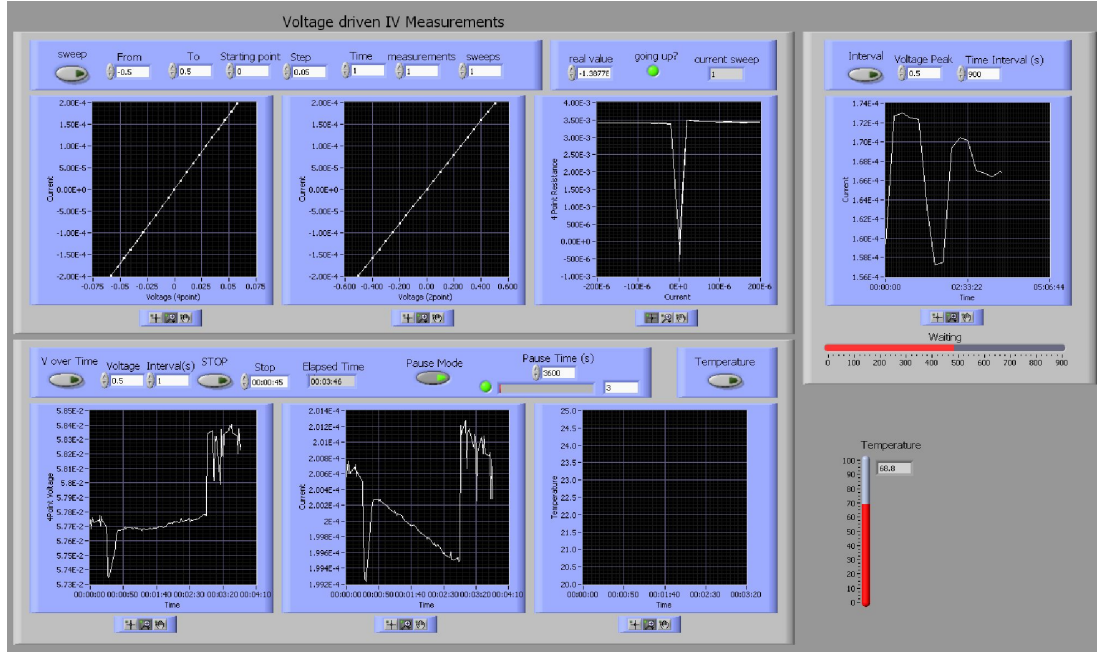


Figure 4.2: LabView program to control the KEITHLEY 2636A over the GPIB protocol.

the sheet resistance, we made an IV sweep in the range of -0.5 to 0.5 V and calculated the slope at zero bias. That way, the errors from off-sets in the voltage are eliminated.

Chapter 5

Metallicity on STO by Ar^+ ion beam irradiation

There are very few details that are known about the conductivity of STO after irradiating the surface with Ar^+ ions. The technique of growing STO in reduced oxygen environment has been preferred, since it is believed that the crystal structure does not change and the vacancy concentration can be well defined. On the other hand, producing oxygen vacant STO from scratch is a very complicated process and needs a lot of experience. Using an ion source to produce the vacancies on a pure STO substrate is a lot easier. There are much less parameters that have to be set, since there is basically only the ion beam and the temperature of the substrate that can be changed. Furthermore, a usual high vacuum chamber with a base pressure of 10^{-8} Torr is good enough to use an ion source and to maintain a reasonable clean atmosphere.

This is the motivation we had to investigate the behavior of a conducting film on STO during the occurrence and its development under various conditions.

5.1 Ion milling energy

One thing that always has to be considered, is that oxygen is not the only ion that is removed from the target substrate. Also are strontium and titanium affected by the bombardment of the argon ions, which leads to a constant removal of the topmost layer. The process of removing an ion from the lattice can be considered as an elastic scattering of spheres. The kinetic energy of the argon ions can be modified and, at least the mean energy, is well known. The energy needed to remove an ion from the lattice is mostly determined by the Madelung potential. Since these energies are very high compared to other materials, it can be expected that the milling rate is relatively low.

Using the simplification, that the elastic scattering can be used to model the removal of the ions we first have to calculate the maximum energy transfer from argon to one of the target ions. The reason for the existence of a maximum energy transfer is because the ions have different masses. Only if the masses are equal, all the energy can be transferred to the target ion. Elastic scattering implies conservation of momentum

$$p_{ar,i} = p_{ar,f} + p_{t,f} \quad (5.1)$$

where p is the momentum, the index ar denotes the argon ion and t the target ion. The subscripts i and f mark the initial and final condition, respectively. The initial momentum of the target ion is assumed to be zero. Furthermore the total kinetic energy is conserved which can be described by

$$E_{kin,ar,i} = E_{kin,ar,f} + E_{kin,t,f}, \quad (5.2)$$

where E_{kin} is the kinetic energy and the same subscripts as in equation 5.1 are used. The kinetic energy of the target ion is also assumed to be zero. Using these two equations leads to the solution

$$\frac{E_{kin,t,f}}{E_{kin,ar,i}} = \mu \cdot \left(\frac{2}{1 + \mu} \right)^2, \quad (5.3)$$

with the mass ratio

$$\mu = \frac{m_{ar}}{m_t} \quad (5.4)$$

where m_{ar} and m_t are the mass of the argon and the target ion, respectively. The energy ratio in equation 5.3 denotes the maximum energy that can be transferred from the argon ion to the target ion. Note that for $\mu = 1$, the bombarding ions have the same mass as the target ion and the energy ratio is unity. Therefore all the energy is transferred to the target ion. With this simplification we can at least give an upper boundary for the energy gain of the bombarded ion. The mean energy, however, is lower because the perfect head-on collision is not very likely. Using the atomic masses for argon and the ions that appear in STO leads to the result which is summarized in table 5.1.

The values are reasonable, because the maximum energy ratio has titanium which is due to the small mass difference of titanium to argon.

Target ion	Energy ratio
Sr	0.860
Ti	0.992
O	0.817

Table 5.1: Energy ratio of strontium, titanium and oxygen which determines the maximum kinetic energy of the ion after being hit by an argon ion.

In the next step we have to estimate the energy needed to remove ions out of the solid. As mentioned before, the main contribution to the binding energy in STO is the Madelung potential [14]. This potential is not constant throughout the whole crystal. There is a slight deviation at the surface because the ions are missing their next neighbors (unsaturated bonds) and due to the abrupt change to the vacuum potential. Furthermore it depends, whether the terminating surface is an Sr-O or Ti-O₂. Since the surface structure, after several minutes of irradiation with argon ions, is not any more well defined, we took the average Madelung potential of the two different terminating surfaces.

The ions don't keep their charge when they are removed by argon. Either they gain electrons, in the case of Sr and Ti, or they lose electrons in the case of oxygen. So in our model, we remove the ion from the lattice and then neutralize it as long as the neutralization needs no energy. That way we can estimate a lower boundary for the removal energy. Adding electrons to strontium and titanium releases energy until they are neutral atoms again. Oxygen on the other hand, only releases one electron by itself, afterwards the electron affinity is actually negative, which means that keeping the other extra electron is energetically more favorable than losing it. Therefore, for oxygen we calculate the removal of only one of the electrons. The effective removal energy for a certain ion t can be described by

$$E_{rem,t} = q_t \cdot V_{Madelung,t} + E_{n,t}, \quad (5.5)$$

where $V_{Madelung,t}$ is the Madelung potential, q_t is the charge of the target ion and $E_{n,t}$ is the energy-gain by changing the oxidation state.

Table 5.1 shows the averaged Madelung potential for different types of surface terminations. It is noted, that strontium has an even lower energy than oxygen due to the high ionization energies of Sr. However, we are not able to measure the loss of strontium on

Target ion	avg. Madelung potential	E_{rem}
Sr	19.89 eV	24.44 eV
Ti	42.98 eV	85.96 eV
O	23.76 eV	44.27 eV

Table 5.2: We show the average Madelung potential for all three components of STO. There are different Madelung potentials because of two different types of surface endings. This potential times the charge determines the energy to move the ion to vacuum level which decreases by the release of energy due to gain or loss of electrons, leading to E_{rem} .

the surface, because it does not result in electrical conductivity. Conversely, the lack of oxygen results in conductivity which is easy to observe. The calculated value also matches to the observed behavior. Using a griddless ion source enables us to produce argon ion beams at low energies. Starting with a fresh STO sample, we were not able to measure any conductivity on the surface by using a discharge voltage lower than 90 V, even after several tens of minutes of ion milling. As we explained before, the actual kinetic energy is around 60 – 70 % of the discharge voltage with an error of about one third. Furthermore we have to consider the maximum energy transfer from oxygen to argon from table 5.1. Therefore the experimental result of the minimum kinetic energy of argon ions that is needed to create conducting STO is about

$$E_{min} = 48.5 \pm 16.0 \text{ eV}. \quad (5.6)$$

It is noted, however, that the energy transfer correction we use is just for the case of head-on collisions which is almost impossible. Furthermore the incident angle of the argon ions is of about 45° which means that there is a chance that they just bounce off the STO without removing anything.

Therefore, we investigated the milling rate dependent on the discharge voltage. By covering one half of the STO sample with high-temperature clean room tape, only the other half was exposed to the ion beam. The covered area was not ion milled which results in a step on the surface after removing the tape. By using an atomic force microscope (AFM), we were able to measure the height of the step. In fig. 5.1 we show an image of the AFM measurement for 300 V, where the step is clearly visible in the middle and the height is indicated by colors. The small bright spots are due to dust particles on the surface. The

step height, divided by the total irradiation time, equals the milling rate which is usually expressed in nm/min.

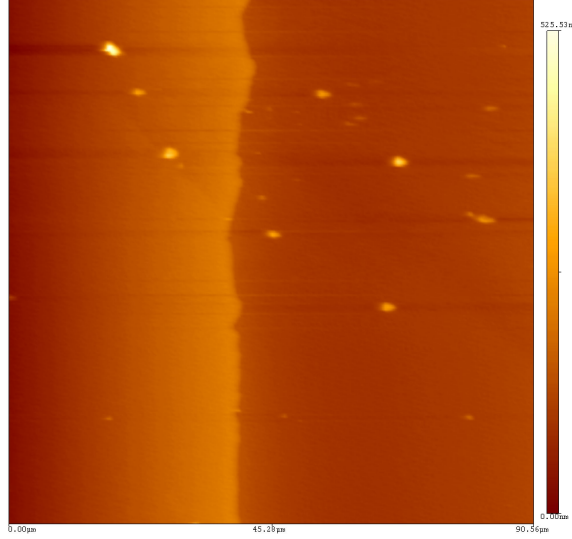


Figure 5.1: AFM image showing a step on STO caused by ion milling, where a tape has covered one half of the sample during the milling process. The voltage was 300 V and the height of the step after 30 min irradiation was 171 nm. The small bright spots are caused by dust particles.

A behavior of the milling rate as a function of discharge voltage can be seen in fig. 5.2. The discharge current was constant at 1 A which leads to a current density of 0.5 mA cm^{-2} . The obtained milling rates are consistent with previous reports [44]. At around 80 V the milling rate starts to rise with increasing milling time. This measurement roughly confirms the previously made observation that there was no conductivity below 90 V. Nevertheless, the experimental obtained value for energy of the argon ions at $V_D = 90 \text{ V}$ is slightly higher than the calculated potential energy for oxygen of 44.27 eV (see tab. 5.1), which is a reasonable result.

Even though titanium seems to have a very high binding energy, it does not mean that it can not be removed at small discharge voltages. Once some ions are removed from the lattice, it is not a perfect crystal structure any more. The binding energies are based on a semi-infinite lattice, so with constant removal of a few ions on the surface, the Madelung potential can deviate significantly from the values given in tab. 5.1. Therefore the binding

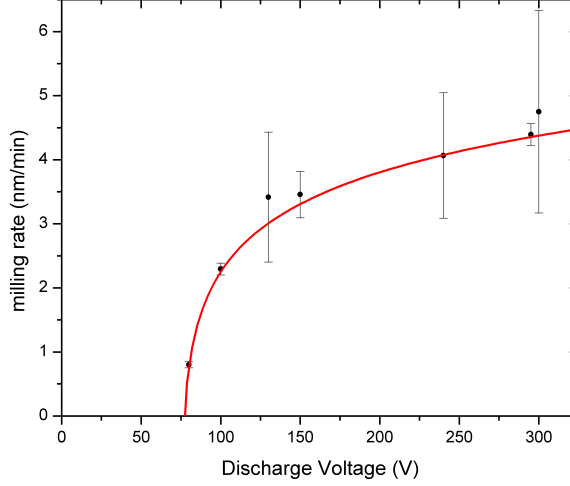


Figure 5.2: Milling rate as a function of the discharge voltage for SrTiO_3 . The discharge current was constant at 1 A. The milling rate was calculated by measuring the milling depth after 30 min. According to the power law fit, the minimum voltage is roughly around 80 V which is consistent with the fact that we were not able to measure conductivity below 90 V.

energy of titanium may drop so it can be removed easily, because once some ions are missing, the whole unit cell might fall apart.

This picture might give rise to the idea that there is a high threshold energy that has to be overcome at the beginning for a perfect crystal. Once there are some holes in the crystal, minimum milling energy drops because of smaller binding energies and the process of ion milling is possible at lower energies.

5.2 Process of oxygen removal

The occurrence of conductivity in STO is due to lack of oxygen. As this phenomenon was first discovered, the fact that the resistance increases as the sample was exposed to oxygen, gave rise to the assumption of oxygen vacancies. When growing strontium titanate films in reduced oxygen environment, it is obvious that oxygen vacancies are produced. But the reason why ion milling introduces oxygen vacancies is not answered yet. Usually ion milling is used to clean surfaces (dry-etching) or to form patterns in the sample by using shadow masks. As we calculated in section 5.1, the binding energy is not the decisive factor, because in this case, strontium vacancies should occur much earlier. Also it has been shown,

that oxygen vacancies can be created within thicknesses of at least 20 nm [34]. The actual penetration depth L of argon ions can be estimated by using the equation [45]

$$L = 1.1 \frac{E^{2/3} W}{\rho (Z_i^{0.25} + Z_t^{0.25})^2}. \quad (5.7)$$

Thereby E denotes the energy of the argon ions in eV, W is the atomic mass of the target, the density of the target is denoted by ρ , and Z_i and Z_t are the atomic numbers of the ion and target, respectively. SrTiO_3 is a compound of different ions so to calculate the atomic mass of the target, we used the weighted average. Since our ion source has a maximum discharge voltage of 300 V, the mean effective argon energy can not exceed the limit of roughly 200 eV, so the maximum penetration depth L is always smaller than 2 nm. This, and the fact that oxygen vacancies have been found beyond the penetration depth leads to the conclusion, that diffusion has to be the essential factor in terms of vacancy creation by ion beam irradiation.

The diffusion coefficient of strontium and titanium in STO is not known, but there are several reasons why it should be much lower than the one of oxygen. The most important aspect is the mass difference. Oxygen is much lighter than strontium and titanium and therefore more mobile. Assigning all particles the same thermal kinetic energy $E_{\text{thermal}} = \frac{1}{2}mv^2$, oxygen should have a much higher velocity and should therefore be able to jump to an empty lattice site much more easier. Another aspect is the distance to the next empty lattice site. The distance from one oxygen to another is only $d_O = \frac{1}{\sqrt{2}}a$, which is small compared to the value $d_{\text{Sr,Ti}} = a$ of strontium and titanium. Free line of sight is also a reason why the diffusion rate should be higher for oxygen than for titanium. For a Ti vacancy, there is no direct straight path to the next adjacent titanium ion, because an oxygen ion is always in between. This is not the case for the oxygen vacancy, where there are always several other oxygen ions in sight. Furthermore might be the amount of covalent bonds an important factor in terms of diffusion, because each bond has to be broken in order to move to another lattice site. Oxygen has two titanium ions as nearest neighbors which have covalent bonds. However, the covalent interaction between two oxygens is not zero, but comparably small. Titanium, on the other hand, has six oxygen ions as nearest neighbors and therefore has three times more covalent bonds than oxygen. Strontium has

almost no covalent character so there is only the ionic bond to oxygen. Since covalent bonds are usually stronger than ionic ones [46], this contribution can be disregarded. In summary, we will make the assumption, that the diffusion coefficient of titanium and strontium is negligible small, which makes oxygen the only ion that is able to move in the lattice.

During the ion milling process, the atoms are constantly removed from the surface, preferable strontium before oxygen and titanium. In fig. 5.3 an illustration of this process is shown. Oxygen has one important different property which is after one is removed from the surface, another oxygen ion from the sublattice is moving upwards to the surface. In another way one can say, that the vacancy on the surface moves into the lattice. This is the important advantage oxygen has in contrary to strontium and titanium in order to create large amounts of vacancies nearby the surface.

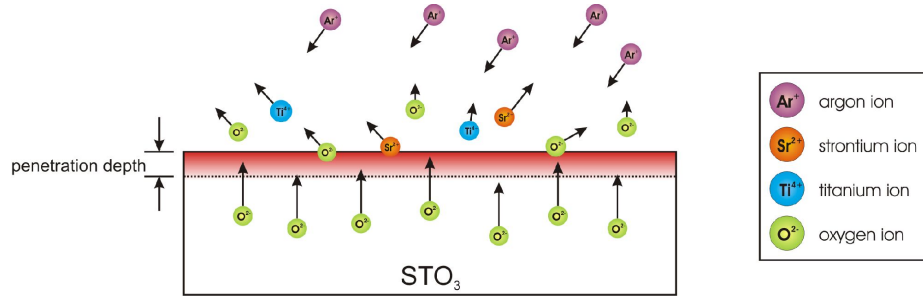


Figure 5.3: The surface layers are getting removed during the argon ion bombardment. The region where ions are actually removed is within the penetration depth. Oxygen has, in contrary to titanium and strontium, the ability to diffuse to the surface. This leads to the conclusion that, relative to the stoichiometric composition, more oxygen is removed.

Since the temperature contributes exponentially to the diffusion, the cooling power is a crucial factor in determining the conductivity of the sample.

5.3 Measurement setup

The experiments were performed at various temperatures so different sample mounting setups were used. To keep the STO sample at room temperatures as good as possible, we used the configuration with a copper plate directly in contact with the rest of the stage (see setup in chapter 3.2.2). Cooling water at a temperature of constant 20°C with a flow rate of approximately $3 \frac{1}{\text{min}}$ was used to establish a reasonable heat dissipation. To get lower

temperatures, we replaced the water with liquid nitrogen in the same stage configuration. The advantage is that the sample can remain in vacuum while switching between two different temperature regimes. Furthermore we investigated the conductivity without any cooling, so we monitored the heat generated by the ion beam itself. Therefore we choose the configuration with the ceramic heater, but without actually running a heating current (see setup in chapter 3.2.3). The heat dissipation through the moly rods is very small, so all the heat induced by the ion beam remains in the sample.

Before starting the ion milling process, the vacuum pressure has to be at least of about 1×10^{-6} Torr before introducing argon gas to a pressure around 5×10^{-4} Torr. Otherwise the amount of impurities is too high and affects the conductivity. Furthermore closing the shutter is necessary to determine the dose of argon ion irradiation with high accuracy. To start the ion beam, we increase the cathode current of the filament I_C to about 15 – 18 A in order to get an initial emission current I_E of about 0.15 A. This current is high enough to ignite the plasma by applying a discharge voltage V_D with a discharge current $I_D \approx 0.1$ V. Then I_D is increased to the desired value of 1 A while keeping the emission current always slightly higher than the discharge current in order to maintain a stable plasma. After setting the current, the discharge voltage can be changed by resetting the argon pressure. For these fine adjustments we used the gate valve in front of the turbo pump to manipulate the effective pumping speed. A higher pressure in the chamber results in a lower discharge voltage at constant I_D and vice versa.

5.4 Conductance development during ion milling

There have been only few studies about the occurrence of metallicity due to ion bombardment. The fact that conductivity is established and that oxygen vacancies are created was more or less accepted but the reason why this is happening or exactly how this phase from insulator to metal is developing was never really investigated. Therefore, we made several measurements under various conditions and studied the conductivity developing with increasing irradiation time. By just reading the conductivity, we developed a model which explains how the phase transition occurs and what the major contributions are. We found

that temperature, and therefore diffusion, are the main aspects when irradiating a STO surface.

To get a detailed picture of the increase of conductivity in STO, it is important to start from a fresh STO sample with high stoichiometry. Used samples have some history in terms of oxygen vacancies and crystal failures so they can not represent reliably the conductance due to the ion milling process. As we pointed out, the diffusion is a major reason for introduction of oxygen vacancies, so we investigated this process at different temperatures, beam currents and beam energies to see how the conduction behaves under these different conditions. With these measurements, we were able to create a model that shows development of the oxygen vacancy concentrations over time.

5.4.1 Low temperature development

Diffusion of oxygen vacancies has a major impact on the occurrence of conduction in SrTiO_3 . Cooling the STO sample down to -170°C decreases the diffusion rate significantly. The calculations are based on eq.(2.21), assuming that the surface concentration is constant. Supposing that these magnitudes are valid, we assume that the thermal diffusion can be neglected at these low temperatures. With eq.(2.21) we can estimate how deep the vacancies can diffuse into the crystal. We find that for -100°C and after one minute, the concentration in a depth of $3 \times 10^{-9}\text{ cm}$ is only 10% of the surface concentration. So we can safely say that the diffusion is zero because it is orders of magnitudes smaller than the milling rate. For comparison, at room temperature the vacancies reaching $1 \times 10^{-5}\text{ cm}$ into the surface until they reach 10%.

The surface bombardment by argon ions causes not only a continuous removal of the crystal, but also there have to be vibrations in the lattice due to sudden distortions from the perfect crystal structure at the surface. Each time an argon ion hits the surface, it squeezes the topmost unit cells which will be carried on to the sublayers, reducing the intensity for each layer until it dies out. This vibration can cause an oxygen ion to migrate to the surface. Conversely one can say, that a recently created vacancy can drift into SrTiO_3 by using the vibrational energy released during its creation. The depth of the vacancy migration is dependent on the argon ion energy and we can assume that the total

amount of vacancies decays exponentially with the depth, which is shown in fig. 5.4. The higher the energy, the deeper the vibration will penetrate. Therefore the thickness of the vibration layer, also called *hot-zone*, is determined by a certain threshold E_{thresh} of vibration intensity, which marks the effective thickness of this vibrating surface. A reasonable order of magnitude for the threshold would be the activation energy for diffusion of oxygen vacancies in STO (see eq.(2.18)). These lattice oscillations are different from phonons, because

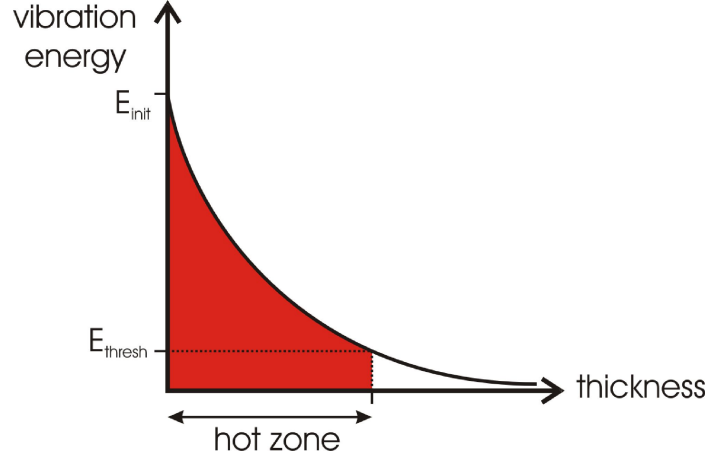


Figure 5.4: Decay of vibration energy on the surface. We define the thickness of the *hot zone* between the surface and the point where the initial vibration energy E_{init} reached the threshold energy of $E_{thresh} = 1/e \cdot E_{init}$. In this layer, the actual sample temperature is not the critical factor which is causing the diffusion.

the incoming argon ions do not have the same energy, but rather a broad distribution of different energies. The fact that the collisions are randomly distributed and not coherent creates a big spectrum of vibration frequencies on the crystal surface. These vibrations interfere with each other which causes a small penetration depth. A good approximation is usually $E_{thresh} = \frac{1}{e} \cdot E_{init}$. These vibrations can be considered as a very localized *hot zone* which does not behave like usual heat and that's why this *pseudo-temperature* will dissipate exponentially into the crystal. Furthermore it is only a movement of the oxygen ions and also mostly perpendicular to the surface. Therefore the lattice vibrations remain at the very surface and cause significantly enhanced diffusion of oxygen vacancies. That means, as soon as the ion milling process occurs, the oxygen vacancy concentration in this *hot zone* starts to increase very fast. Because of the ion bombardment, the surface layers are removed continuously, which prevents a divergence of the carrier concentration. There

is a so called *steady-state*, that occurs when the effective thickness of the *hot-zone* is ion milled away for the first time. After that, the carrier concentration profile at the surface does not change any more and the conductance caused by vibrations remains constant.

Since the profile of the vibration intensity is assumed to be exponential (see fig. 5.4), the vacancy profile should also have an exponential shape with an effective thickness d_0 . This carrier concentration profile $\Delta n(x, \Delta t)$ after time Δt can be described by

$$\Delta n(x, \Delta t) = \frac{dn_s}{dt} \Delta t e^{-\frac{x}{d_0}}, \quad (5.8)$$

where $\frac{dn_s}{dt}$ is the increase of carrier density on the surface per time due to creation of oxygen vacancies and d_0 is the effective thickness of the conducting layer. The whole carriers after time Δt can be calculated by performing the integral. An important factor is the milling process, which does occur during that time. The milling rate r , defined as the thickness of the layer which is removed per time, so after Δt has past, a layer with the thickness $r \cdot \Delta t$ has been removed. A simplified picture of the process is shown in fig. 5.5. The total amount of carriers $N(t = \Delta t)$ after Δt equals the amount at $t = 0$, which is the integral from $x = 0$ to ∞ (see fig. 5.5(a)), plus the same integral, but starting at $x = r \cdot \Delta t$ (see fig. 5.5(b)), because this part corresponds to the removed layer due to ion milling. This can be described by

$$N(t = \Delta t) = \underbrace{\int_0^{\infty} \frac{dn_s}{dt} \Delta t e^{-\frac{x}{d_0}} dx}_{\text{part 1}} + \underbrace{\int_{r\Delta t}^{\infty} \frac{dn_s}{dt} \Delta t e^{-\frac{x}{d_0}} dx}_{\text{part 2}}. \quad (5.9)$$

The two different parts are labeled in fig. 5.5(b). For a different time t this can be written as

$$N(t + \Delta t) = N(t) + \int_{rt}^{\infty} \frac{dn_s}{dt} \Delta t e^{-\frac{x}{d_0}} dx, \quad (5.10)$$

which can be expressed by

$$\frac{N(t + \Delta t) - N(t)}{\Delta t} = \int_{rt}^{\infty} \frac{dn_s}{dt} e^{-\frac{x}{d_0}} dx. \quad (5.11)$$

For arbitrary small Δt we get the time derivative of the total amount of carriers per area

$$\frac{dN(t)}{dt} = \int_{rt}^{\infty} \frac{dn_s}{dt} e^{-\frac{x}{d_0}} dx. \quad (5.12)$$

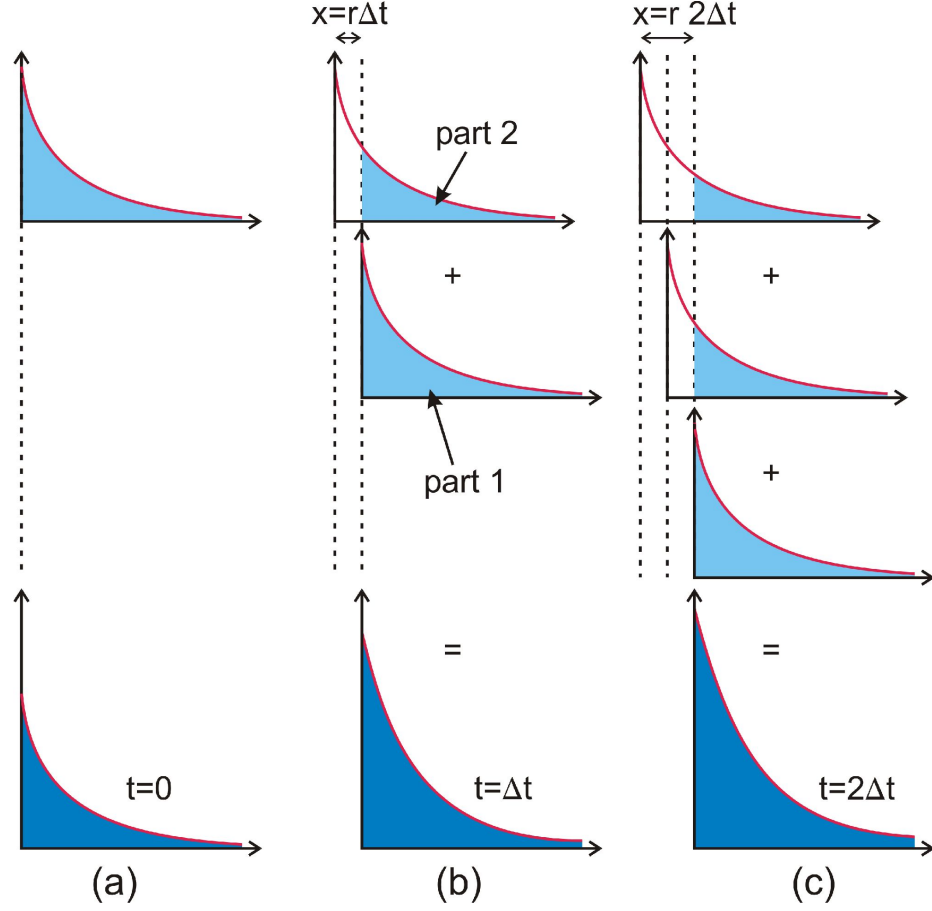


Figure 5.5: This sketch explains the occurrence of the steady state. (a) At time $t = 0$, the carrier concentration distribution forms an exponential shape according to the decay of the vibration energy in the *hot zone*. (b) After a time interval Δt , the process of ion milling removed layer with the thickness $r \cdot \Delta t$, where r is the milling rate. So the carrier concentration profile moves about this depth further in addition to the remaining part of the previous profile. The total amount of carriers for this case is calculated in eq. (5.9). (c) This process continues until the original profile from the very surface is removed. At that point, the carrier density profile remains constant and the *steady-state* occurred.

By executing the integral and solving the obtained differential equation, we get the result

$$N(t) = \frac{dn_s}{dt} \frac{d_0^2}{r} \left(1 - e^{-\frac{r}{d_0}t}\right), \quad (5.13)$$

with $\frac{dn_s}{dt}$, the increase of carriers per time and volume, the effective thickness of the conducting layer d_0 and the milling rate r . This equation describes the behavior of the carrier

concentration per area without any thermal contribution. It is noted, that the amount of introduced carriers per time and area N_{total} can be described by

$$\frac{dN_{\text{total}}}{dt} = \frac{dn_s}{dt} d_0 \propto r \quad (5.14)$$

and should be proportional to the milling rate r . This is a reasonable approximation because the faster the surface layer is removed, the more vibrations are induced into the crystal. This increases the amount of oxygen coming out of SrTiO_3 and therefore the carrier concentration rises. Plugging this assumption into eq. (5.13) leads to

$$N(t) \propto d_0 \left(1 - e^{-\frac{r}{d_0}t}\right). \quad (5.15)$$

This shows that the saturation value of the carrier concentration is proportional to the thickness of the conducting layer. The ratio of the thickness and the milling rate determines, how fast this saturation value will be reached. The thickness of the layer scales with the energy of the argon ions which is determined by the discharge voltage V_D . Changing the discharge current does have an impact on the amount of argon ions and therefore on the milling rate. There should be no difference in the saturation value for ion milling with the same discharge voltage but different currents. The only difference is the time needed to saturate. In fig. 5.6 we show the experimental result of ion milling a fresh SrTiO_3 sample with two different discharge currents and the same discharge voltage. It is obvious that the plot with 3 A saturates faster, as predicted, but the saturation conductance is much higher than for the 1 A case. The deviation from the predicted scenario shows that (5.13) is missing an important effect, the clustering of oxygen vacancies. As mentioned before, we assumed that the induced vacancies in the *hot-zone* are not able to move parallel to the surface. Of course, this is just the ideal case. Some vacancies are able to move around in the surface layers and once two of them meet around the same titanium ion, they form a cluster and are trapped. The amount of electrons contributing to the conduction therefore decreases from 4 to 2, leaving two electrons localized at the titanium ion. So the probability of two vacancies forming a cluster increases with time. Considering the case for 1 A and 3 A we have the same *hot-zone* thickness due to equal ion energies, but different milling rates (roughly factor of 3). Therefore the *hot-zone* in the 1 A case remains three times longer than in the 3 A case, giving the vacancies three times longer to form a cluster. The ratio of

the saturation values in fig. 5.6 is about two, which means that the milling rate ratio is not exactly three or that the clustering probability is not proportional to time. Because it is

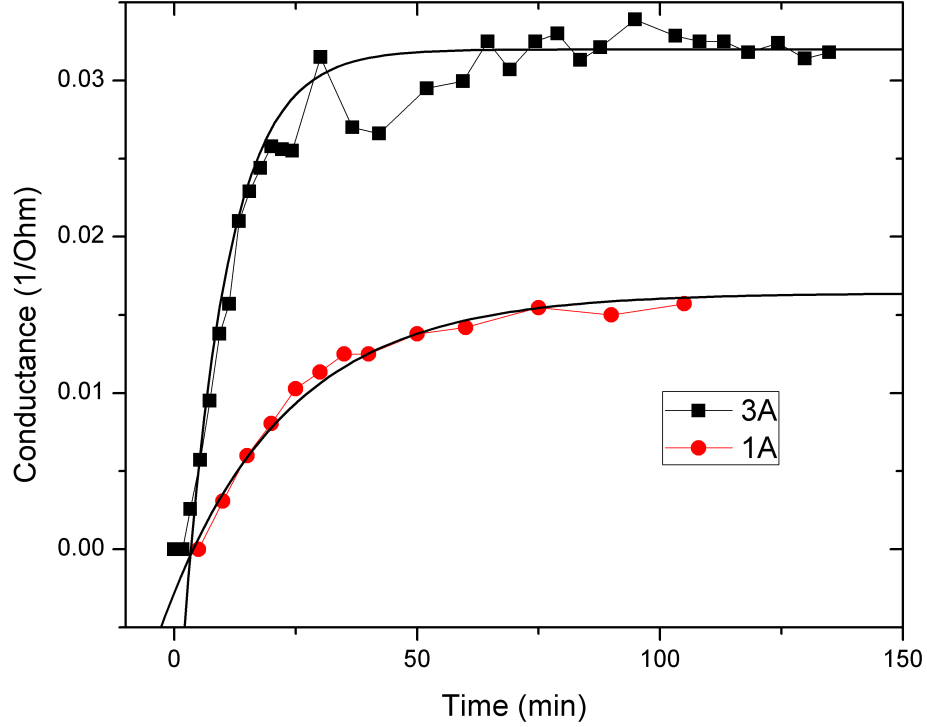


Figure 5.6: Conductance of SrTiO_3 versus ion milling time for different discharge currents. The temperature was measured at -140°C . According to our model, the thickness of the conducting layer should be the same (confirmed by the faster saturation of the 3 A plot) and therefore the saturation value for the conductance. The higher amount of oxygen vacancy clusters in the 1 A plot explains the lower conductance.

unclear how much clustering occurs during the ion milling at low temperatures, we are not able to calculate exact values. But by fitting the measured data with eq.(5.13), we can at least extract a lower boundary for several unknown factors. However, the fitting parameter of the exponent can be used to confirm that the thickness of the *hot-zone* is the same for different argon ion currents. We found that the fitted decay time for 1 A is roughly three times larger than in the 3 A fit. We therefore assume that this difference is rather due to the milling rate r than due to the depth of the conducting layer. The thickness d_0 can be calculated by using the fitted value and the milling rate r for a discharge voltage of 100 V of fig. 5.2. Therefore we found the effective thickness of the conducting layer to be

$$d_0 = 57 \text{ nm.} \quad (5.16)$$

Furthermore, the increase of carrier density per time and the saturation concentration on the surface can be calculated. Since the clustering must be lower in the 3 A case, we will use the fitting parameters from this plot. First, we have to convert the carrier concentration per time and area to the actual measured conductance G , which is defined by

$$G = \sigma \frac{A}{l} = \sigma \frac{d_0 \cdot l}{l} = \sigma d_0, \quad (5.17)$$

where $A = l \cdot d_0$ equals the cross-sectional area of the conducting surface with the length l , and the conductivity σ is given by

$$\sigma = \mu e n, \quad (5.18)$$

with the electron mobility μ , the carrier concentration n and the electron charge e . This leads to

$$G = \mu e \underbrace{n d_0}_{N(t)} = \mu e N(t), \quad (5.19)$$

which is the conversion equation from conductance to carrier concentration per area. This is justified because n is almost constant over a wide doping range [18]. The electron mobility at a temperature of -140°C can be found in the literature and was estimated to $\mu = 49 \frac{\text{cm}^2}{\text{Vs}}$ [47]. With the value obtained from the fit, we found that the increase of carriers on the surface is

$$\frac{dn_s}{dt} = 5.2 \times 10^{17} \frac{1}{\text{cm}^3\text{s}}. \quad (5.20)$$

With this result, we can calculate the carrier concentration of the conducting surface, which has a thickness of $d_0 = 57 \text{ nm}$. This concentration can increase, as long as the *steady-state* is not reached yet. The time to reach this state can be calculated out of the milling rate $r_{100\text{V}} = 2.3 \frac{\text{nm}}{\text{min}}$ and d_0 . Therefore, the saturated surface concentration is

$$n_s = \frac{dn_s}{dt} \cdot \frac{d_0}{r_{100\text{V}}} = 2.6 \times 10^{20} \frac{1}{\text{cm}^3}. \quad (5.21)$$

It is noted, that the fit has an off-set in order to match more accurately to the measured data. This off-set is not reflected in eq.(5.13), because there are different factors that lead to this behavior. The most important reason for an off-set is the fact, that we are measuring conductance and not the carrier concentration. Above a critical carrier concentration, conductance suddenly occurs [22] (insulator-metal-transition). The electron mobility is

almost constant after the transition over a wide doping range [18], therefore our model seems to be a good approximation. Furthermore we note, that we calculated only the lower boundary. The actual carrier density is higher, but these carriers are trapped at the titanium sites in the vacancy clusters.

The electric conductivity occurs at low temperatures only on the surface at nanometer scales, because the thermal diffusion is suppressed by the liquid nitrogen cooling. Therefore the milling rate has a significant impact on the development of the conducting layer. The parameters of the argon ion beam have also an influence on the behavior of the conductance with increasing milling time. These are the reasons why it is even possible to decrease the conductance by irradiating SrTiO_3 with argon ions. In fig. 5.7 we show the conductance of STO with alternating ion beam energy. The discharge voltage is switched between

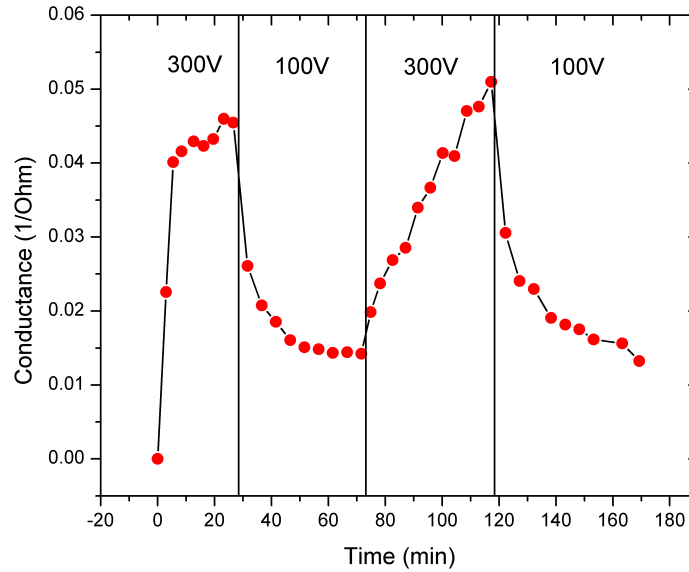


Figure 5.7: Conductance of SrTiO_3 at -130°C with switching ion beam energy at a constant current of 1 A. Higher voltage causes a thicker *hot-zone* which is more conducting. Switching back to 100 V causes a conduction decrease because the conducting layer is getting thinner. The occurrence of oxygen vacancy clusters leads to different shapes of the plot during the transition from low conducting to high conducting state.

300 V and 100 V at a constant discharge current of 1 A. A higher voltage leads to a thicker *hot-zone*, because the vibrations on the surface are reaching deeper into the crystal. After starting the ion milling at 300 V, the conductance increases very fast and tends to saturate. Switching to the lower voltage shows an exponential decay to a third of the initial conduction

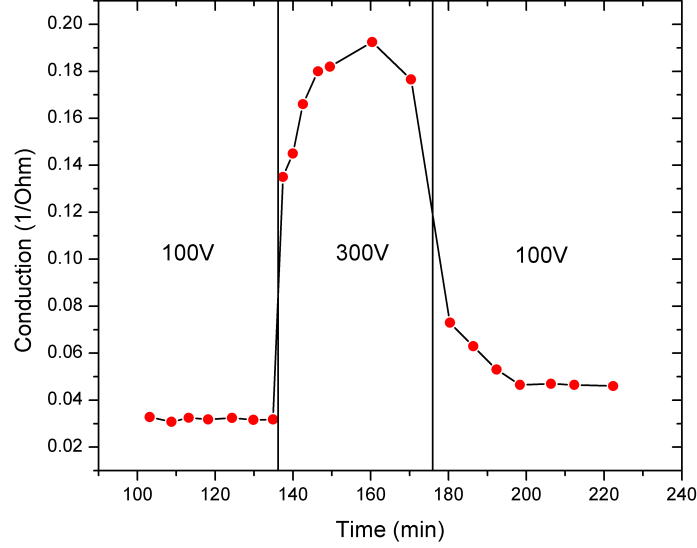


Figure 5.8: Similar behavior of switching conductance due to different ion milling voltages. The absolute values are different from the ones in fig. 5.7, because the milling history of the samples is different. Dependent on the ion beam properties of previous irradiations on the sample, the conductance difference between 100 V and 300 V may be vary.

value. Alternating back to 300 V shows a slower increase than at the beginning. This is the point where the history of the surface has a significant impact on the conductance development.

The exact behavior is difficult to predict due to the combination of various effects. The most important factor is, besides the increasing surface roughness, the influence of oxygen vacancy clusters. The current and the energy of the beam determines the amount of vacancy clusters on the surface. In fig. 5.8 we show a similar but much higher switching of the surface conductivity. The different amount of increases must be related to the ion milling history of the sample. However, it is not clear what kind of ion milling has to be done before switching from 100 V to 300 V in order to get a large increase. Our obtained data might suggest, that a higher ion beam current decreases the amount of clusters. Furthermore it seems that higher energy also leads to less clusters and might also have the ability to break clusters apart. However, these hypotheses are not well confirmed since it is not easy to measure the exact amount of vacancies in relation to the amount of carriers. Further measurements have to be done in order to get a better understanding of the present circumstances.

5.4.2 Room temperature development

The contribution of temperature to the conductance can be suppressed, as shown in the previous section, by cooling the sample down to -140°C , in order to study the contribution of the surface vibrations. The calculated surface concentration of about $2.6 \times 10^{20} \frac{1}{\text{cm}^3}$ is located in the surface layer with a thickness of less than 100 nm. Beyond that layer, the carrier density is several orders of magnitudes lower. This fact changes drastically, when the SrTiO_3 temperature increases. Our calculations show, that this concentration gradient decays within seconds due to thermal diffusion at ambient temperatures. Therefore we conclude that the surface concentration at room temperature must be much lower, even during the ion milling process. However, the amount of carriers at the surface has to be constant in the *steady-state*. There is an equilibrium of oxygen vacancy flux entering the surface layer through the process of ion milling and the flux leaving the surface into the bulk due to thermal diffusion. With this picture we created a model to describe the behavior of the conductance with increasing ion milling time.

Once the *steady-state* is reached, the carrier concentration on the surface n_S is assumed to be constant. The shape of the carrier density as a function of depth is described by the complementary error function (see (2.21)), so

$$n(x, t) = n_S \operatorname{erfc} \left(A \frac{x}{\sqrt{t}} \right), \quad (5.22)$$

where $A = \frac{1}{2\sqrt{D}}$ is a constant, involving the diffusion coefficient D . To calculate $N_{\text{total}}(t)$, the whole carrier concentration per area, we do the space integral over $n(x, t)$, which yields

$$N_{\text{total}}(t) = \int_0^\infty n_S \operatorname{erfc} \left(A \frac{x}{\sqrt{t}} \right) dx = n_S \underbrace{\int_0^\infty \operatorname{erfc} \left(A \frac{x}{\sqrt{t}} \right) dx}_{d_{\text{eff}}(t)}. \quad (5.23)$$

The integral has the unit of a length and can be considered as the effective depth of the conducting layer. By substitution of $A \frac{x}{\sqrt{t}}$ with y , which leads to

$$dx = \frac{\sqrt{t}}{A} dy \quad (5.24)$$

we can simplify this term to

$$d_{\text{eff}}(t) = \int_0^{\infty} \text{erfc}(y) \frac{\sqrt{t}}{A} dy = \frac{\sqrt{t}}{A} \underbrace{\int_0^{\infty} \text{erfc}(y) dy}_{\frac{1}{\sqrt{\pi}}} = \frac{1}{A\sqrt{\pi}} \sqrt{t}. \quad (5.25)$$

That shows, that the effective thickness of the conducting layer scales with \sqrt{t} , the same dependency that should apply for the conductance. So finally, we can present the equation

$$N_{\text{total}}(t) = \frac{2n_S\sqrt{D}}{\sqrt{\pi}} \sqrt{t}, \quad (5.26)$$

which describes the total amount of carriers per area as a function of time. It is noted, that it only depends on time and temperature (contained in the diffusion coefficient D). The milling rate is small compared to the diffusion rate, so it does not change the conductance much. By using eq.(5.19), we can extract the carrier density out of the fit from fig. 5.9. The temperatures are different due to different discharge voltages. The power of the 300 V ion beam is three times higher than for the 100 V beam. We used the sample stage configuration with the copper plate in tight contact to the stage and used water as cooling liquid (see setup in chapter 3.2.2). The temperature at the end of each ion milling cycle for 100 V and 300 V reached a maximum value of 65 °C and 80 °C, respectively. The equation that has to be used to fit the measured data has to represent the conductance. Therefore eq. (5.26) is converted by using eq. (5.19) which leads to

$$G(t) = \frac{2n_S\mu e\sqrt{D}}{\sqrt{\pi}} \sqrt{t}, \quad (5.27)$$

where μ is the electron mobility and e the electron charge. With the fitting parameters from fig. 5.9, we can calculate the surface carrier concentration for the two different cases. As it can be seen on the plot, the shape within the first 20 min is different than the rest. This is the phase when the *steady-state* is not reached yet and the concentration on the surface is still changing. Once it is constant, our assumptions for eq. (5.26) are valid and the conductance increases with \sqrt{t} . The fitting parameter for the amplitudes yields

$$n_{S,100\text{ V}} = 1.8 \times 10^{18} \frac{1}{\text{cm}^3} \quad \text{and} \quad n_{S,300\text{ V}} = 1.5 \times 10^{18} \frac{1}{\text{cm}^3}. \quad (5.28)$$

This surface concentration is small compared to the concentration due to vibrations (see eq.(5.21)) at low temperatures. This shows that the temperature diffusion has a significant

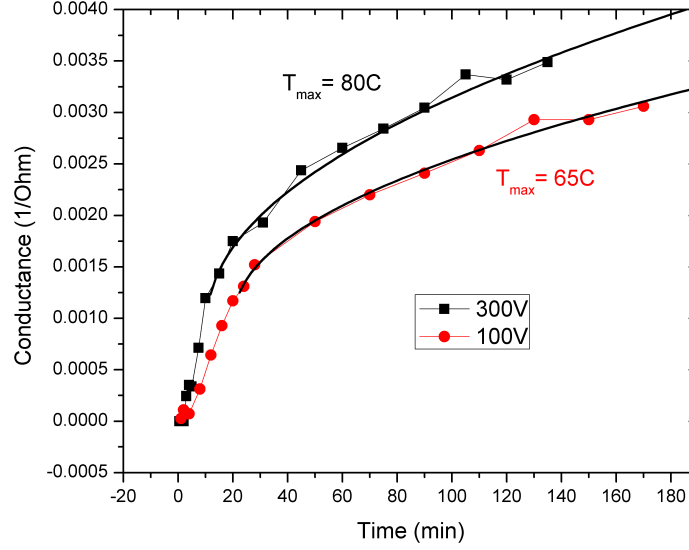


Figure 5.9: Conductance over milling time for two different discharge voltages. The behavior is completely dominated by thermal diffusion. Due to a constant oxygen vacancy source on the surface, the dependence goes with \sqrt{t} . The stronger increase of conduction for 300 V is not due to the voltage different but because of the higher temperature. At these conditions, the thickness difference of the *hot-zone* for different voltages has no effect on the conductance. The actual temperature during the conductance measurement was 30 °C.

impact on the conductance, because the carriers can penetrate the crystal a lot deeper than in the case of vibrations, which is only around 100 nm. It should be mentioned, that the concentration for 300 V is smaller than for 300 V. This is due to It is noted, that the surface concentration is roughly one order of magnitude above the necessary density to perform the insulator-metal transition. A rough estimation of the effective thickness can be done by using eq. (5.25). After 100 min, for instance, the effective thickness is

$$d_{\text{eff},100\text{V}} = 2.4 \mu\text{m} \quad (5.29)$$

for the 100 V case, and

$$d_{\text{eff},300\text{V}} = 3.7 \mu\text{m} \quad (5.30)$$

for the 300 V measurement. These values are much larger than at low temperatures. Therefore the milling rate is almost negligible and does not change the thickness significantly. This is the reason why we weren't able to control the conductivity by changing the discharge voltage as in fig. 5.7 and fig. 5.8. The carriers are spread over a great depth, which increases

with time, so even if the surface concentration is lower, the diffusion due to temperature will dominate the conductance after a certain amount of time.

The temperature of the sample effects the behavior of the conductivity after the concentration in the *hot zone* saturated. However, the amount of oxygen vacancies is not known exactly, but we assume it has to be a few factors higher than the carrier concentration. Due to the temperature the probability of vacancy clustering is much higher.

5.4.3 High temperature development

Increasing the temperature of SrTiO_3 during the ion milling process to high temperatures, that means reducing the cooling power, can result in very high conductive samples. For this type of measurement we used the silicon heating device (see setup in chapter 3.2.2), in order to reduce the heat dissipation. We did not run any current through the silicon, so the whole heating energy came from the Ar^+ beam and the filament of the ion source. The temperature was measured with the thermocouple directly on the STO sample. For a better thermal contact, we used a tiny drop of silver paint.

In this configuration, the temperature saturated during the ion milling after a certain amount of time at around 300°C . This means, the contribution of the diffusion due to temperature dominates the vibration effect, so we can neglect the existence of the *hot-zone*. In fig. 5.10 the conductance at a measurement temperature of 30°C is shown as a function of time. The plot shows the expected much stronger increase of conduction compared to a temperature of 60°C in fig. 5.9. Nevertheless, the shape of the curves are somehow different. There are mainly two reasons, why the behavior is different from the \sqrt{t} shape. The slow increase of conductivity at the beginning ($t < 50$ min) can be explained by the way the data was recorded. The interval between each measurement is smaller, which means the milling time was shorter. This results in a temperature lower than 300°C at the end of the milling process, so the oxygen vacancy diffusion is smaller. Furthermore, the time to cool down to the measurement temperature is shorter, so the total exposure time to heat was even shorter. Therefore this range of the plot has to be handled differently than the rest. After that, the conduction follows a \sqrt{t} shape, that lasts until around $t = 400$ min. At that point, the assumption of a semi-infinite system, which the \sqrt{t} dependence is based on,

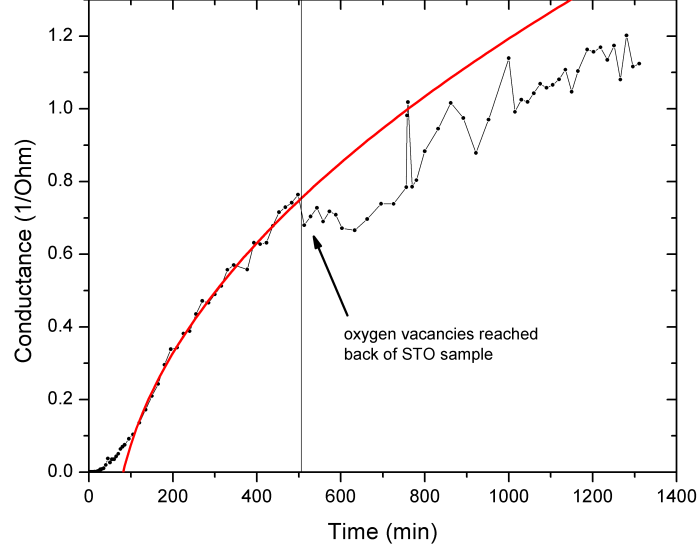


Figure 5.10: Conductance as a function of time with an ion milling temperature of 300 °C. The measurement temperature is 30 °C. The conductance is dominated by the temperature diffusion after the first 50 min. The square root fit (red curve) is performed between 100 min and 400 min, because after long milling times, the sample can not be considered as a semi-infinite medium. At the beginning, the fit is not accurate, because the temperature was lower than 300 °C.

is not valid any more. This can be roughly estimated by using eq. (2.21) from the diffusion model of a constant surface carrier concentration. This equation deviates from the real diffusion at the time when the concentration at the back side of the sample gets reasonable high. So by calculating the ratio between the front surface concentration ($z = 0$) and the concentration of the back side ($z = 0.05$ cm) yields

$$\frac{c(z = 0.05 \text{ cm}, t = 400 \text{ min})}{c(z = 0, t = 0)} = \text{erfc} \left(\frac{0.05 \text{ cm}}{2\sqrt{D \cdot 400 \text{ min}}} \right) = 0.19. \quad (5.31)$$

That means, after 400 min the concentration at the back side is around one magnitude smaller than on the front side. Since the thickness of the conducting layer is now limited, the increase of conductance is restrained. One might suggest, that the limited sample thickness might increase the conductance because the carriers are not able to leave the crystal. But increasing the concentration on the backside causes a decrease of the carrier density gradient that leads to a slower diffusion. This is the reason why the conductance increase slows down after 400 min.

By using the fitting curve in the valid range (between 50 min and 400 min), we can extract the carrier concentration n_S on the surface in the same manner as we did in the previous section. By using eq. (5.26) and (5.19) and the corresponding fitting parameter from fig. 5.10 we can calculate the surface concentration to

$$n_S = 8.8 \times 10^{19} \frac{1}{\text{cm}^3}. \quad (5.32)$$

This value is about four times higher than the concentration in the case of 60 °C. That factor is just for the surface density, but considering that the conducting layer is reaching into a great depth, it has a great impact on the whole conductivity of the sample. Furthermore we have to assume a very big amount of oxygen vacancy clusters in this SrTiO₃ sample. We observed a deep dark blue color on the surface after the milling process. This blue light emission is correlated with the localized state within the band gap which comes along with the vacancy clusters [30]. So we can say, the darker the sample, the more clusters are formed.

5.4.4 Comparison between low and high temperature conductance

In the previous section we prepared conducting SrTiO₃ samples by bombarding them with argon ions at different temperatures. For a small temperature range we could compare the impact of changing the current or the voltage of the ion beam. In order to compare the conductance for a wide range of temperatures we have to know the change of conductivity with temperature in oxygen deficient STO. By using this curve as an conversion reference, we can make a comparison of the conductance between differently prepared samples. Therefore we ion milled a sample at low temperatures and measured the development of the sheet resistance as a function of temperature. The clearly metallic behavior is shown in fig. 5.11. By fitting the plot with a power law, we found a dependence of $T^{2.7}$, which is consistent with other mobility measurements [34][18]. Applying this conversion to the low temperature measurements and converting the recorded values to 30 °C should lead to a reasonable comparison between low temperature and room temperature measurements. Fig. 5.12 shows the converted data for two different discharge voltages. It can be clearly seen that the conduction for 300 V at low temperatures is, compared to the conduction at

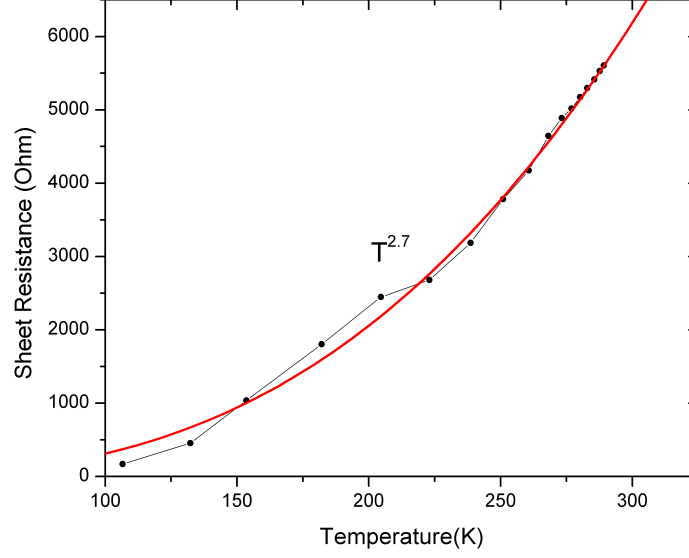


Figure 5.11: To compare the absolute resistance values of measurements performed at -140°C and 30°C , they have to be converted. This temperature dependence shows very good the metallic behavior, as the SrTiO_3 is getting more conducting at lower temperatures.

room temperature, much higher after a shorter time. This would suggest that the thermal diffusion would suppress the conductivity by reducing the amount of introduced oxygen vacancies. This conclusion is hard to explain and would be inconsistent with our model.

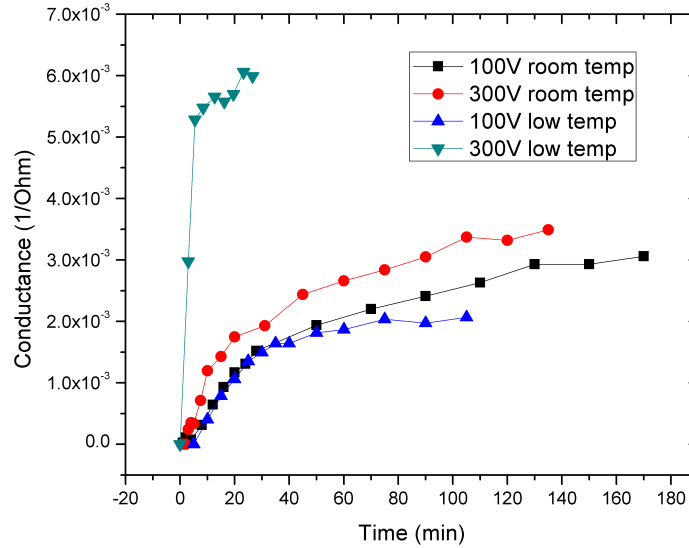


Figure 5.12: Comparison of low and high temperature measurements for different voltages at 30°C by using the conversion from fig. 5.11. It is obvious, that the 300 V measurement for low temperatures is still higher then the room temperature measurement even after the conversion, which is inconsistent with our model.

Therefore we did further investigations to explain this behavior. It turns out that this conversion is not representing the real resistance behavior. The conductivity $\sigma(T)$, usually defined by

$$\sigma(T) = n e \mu(T), \quad (5.33)$$

implies the mobility $\mu(T)$ as the only temperature dependent factor. In the case of high concentration of oxygen vacancies in SrTiO_3 , we measured an irreversible temperature dependence of the carrier density $n(T)$. Performing another cooling cycle after the warm up, we observed a low temperature conductance value a few factors higher than the initial conductance after the ion milling. In fig. 5.13 we show the behavior of the conductance during the second cool-down. Warming up a sample to 20°C , which was ion milled at tem-

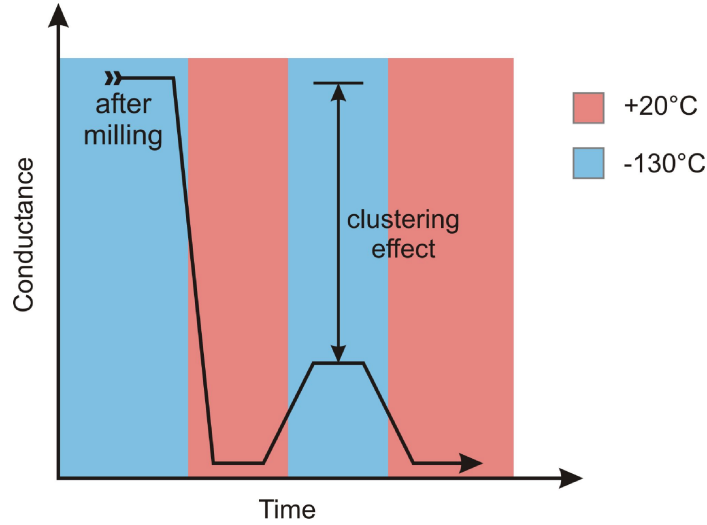


Figure 5.13: The different conductance values at low temperatures might suggest that changing the temperature is accompanied by an irreversible oxygen vacancy clustering process that lowers the conductance by a factor of 3-4. The vacancies are highly dense, but the lack of thermal diffusion decreases the ability to form clusters. Increasing the temperature leads to a higher diffusion rate and therefore a higher probability of two vacancies meet each other to form a cluster. A cluster of two vacancies decreases the amount of carriers contributing to the conduction from 4 to 2.

peratures around -100°C , leads to a reduced conductance due to a lower electron mobility. Increasing mobility at lower temperature suggests metallic behavior because the scattering at the lattice decreases. This is a reversible process and can not explain the behavior in fig. 5.13. This leads us to the conclusion that the carrier concentration has been irreversibly

changed. It has been reported that the clustering of oxygen vacancies decreases the amount of carriers contributing to the conduction [30]. To create a cluster of two vacancies, they have to meet at the same titanium ion. If there is almost no thermal diffusion, the chances for cluster accumulation is therefore very small. As soon as the temperature rises, the clustering occurs and carriers are getting trapped at the titanium site. This, and the lower electron mobility contribute to the lower conductivity. Cooling the sample down again shows that the conductivity does not increase to the previous value which shows that one of the mechanisms is not reversible. However, the ratio of the conductivity between the room temperature value and the one at low temperature after recooling the sample matches to the mobility ratio from the literature [47]. We therefore conclude, that the change of conductivity after recooling is not interfered by vacancy clustering.

The clustering factor κ , defined as

$$\kappa = \frac{G_{\text{init}}}{G_{\text{cluster}}}, \quad (5.34)$$

which is the ratio of the conductance with clusters G_{cluster} to the conductance after the ion milling process G_{init} . We can not say that the ion milling at low temperatures does not introduce any clusters. But since the thermal diffusion is significantly suppressed, it is reasonable that the clustering is proportional to the diffusion, and therefore scales exponentially with temperature. However, there has to be a saturation value if the amount of oxygen vacancies is finite, because at a certain point all vacancies might have formed clusters.

We measured κ for different ion milled samples. The result shows that the cluster factor is different for ion milling with 100 V or 300 V. Based on multiple measurements we found that

$$\kappa = 3 - 4 \quad (5.35)$$

which shows that the clustering has a significant impact on the conduction. These factors describe the clustering of oxygen vacancies below 20 °C. The dimension of this factor seems to be reasonable since similar values have been reported [29]. Using this factor and correcting the conversion from fig. 5.12 and artificially "adding" the cluster contribution to the low temperature plots by dividing them by κ leads to the new conversion shown

in fig. 5.14. This conversion seems more reasonable, because the mismatch of the 300 V

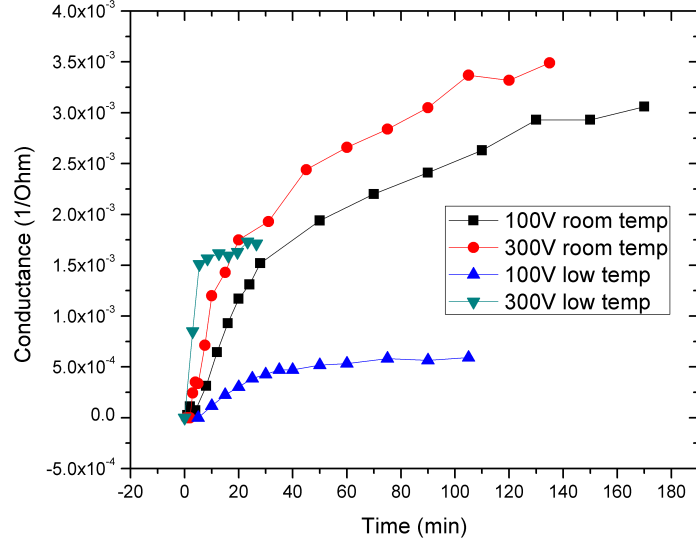


Figure 5.14: Comparison of low and high temperature measurements with cluster correction is shown for different discharge voltages. The ratios between the measurements of the same temperature are more reasonable. Considering that the actual temperature of the room temperature measurements is actually 65 – 80 °C suggests a still uncorrected even higher amount of clusters. This would shift the room temperature plots upwards.

plots almost disappears. The increase of conductance at the beginning is still higher for low temperatures which could be explained by the fact that the *steady-state* is not reached yet and the impact of the thermal diffusion is not crucial. However, the actual milling temperature of the room temperature milling plot was as high as 65 °C and 80 °C for 100 V and 300 V, respectively. If we assume that the cluster rate increases with temperature, the amount of clusters might be even higher than the amount we artificially added to the low temperature plots. Therefore one would have to make a correction for these plots too which would shift the conductance upwards.

5.4.5 Summary

Investigating the development of conductivity by ion milling was not well studied previously. It has been assumed that the decrease of resistance is getting smaller with time [26][34], but the exact behavior was not known. Also the mechanism of the oxygen vacancy occurrence due to ion bombardment was not reported. Based on our measurements we found a model

which shows that temperature has a huge impact on the development of the conductivity. The thermal diffusion at temperatures around -100°C and lower is almost completely suppressed but conductivity can still occur because of lattice vibrations caused by the ion bombardment. We found an almost constant conductance for a discharge voltage of 100 V after long time. The carrier concentration on the surface was found to $n_s = 2.6 \times 10^{20} \frac{1}{\text{cm}^3}$ with an effective thickness of $d_0 = 57 \text{ nm}$. We found that clustering of oxygen vacancies affects the conductivity and is higher for lower discharge currents. Going to room temperature and higher showed the significantly enhanced migration of vacancies due to thermal diffusion. The high concentration on the surface can not be maintained and drops to $n_{S,100 \text{ V}} = 1.8 \times 10^{18} \frac{1}{\text{cm}^3}$ and $n_{S,300 \text{ V}} = 1.5 \times 10^{18} \frac{1}{\text{cm}^3}$ for temperatures around $65 - 80^{\circ}\text{C}$ and a discharge voltage of 100 V and 300 V, respectively. The conductance, however, never saturates. The higher the temperature, the higher the increase of conductance. The carrier density at the surfaces increases to $n_s = 8.8 \times 10^{19} \frac{1}{\text{cm}^3}$ for milling temperatures of 300°C . We found that higher temperatures increase the amount of oxygen vacancy clustering and which leads to significant changes in the conductivity.

5.5 Time dependent studies

When measuring sheet resistances of oxygen vacant STO, it is well known, that exposing the sample to oxygen can has a significant impact on the resistance value due to oxidation [37]. Therefore in-situ measurements are the preferred way to perform these kinds of measurements in order to minimize any change of conductivity. What usually remains unconsidered is the diffusion of the oxygen vacancies. Especially for thin conducting layers, e.g. introduced by argon ion bombardment, where the vacancy concentration gradient is big, diffusion can have a great impact on the resistance. Therefore, we investigated the conductivity behavior as a function of time at different temperatures. Since temperature is the dominant factor for the speed of the diffusion, it should have a measurable effect on the conductivity.

5.5.1 Preparation of measurements

In order to show good diffusion effects, the initial conducting layer should be as thin as possible so that the concentration gradient of oxygen vacancies is reasonable big. Therefore we used configuration showed in section 3.2.2 with either water or liquid nitrogen as cooling fluid. The STO sample was mounted on the copper plate with a sapphire plate as spacer. Silver paint was used as glue in order to get a good thermal contact and the temperature was measured with a thermocouple tip directly mounted on top of the STO sample. To create vacancies, we used the ion source at a discharge voltage of 100 V and a current of 1 A in order to keep the milling temperature in a range of 60 °C after a milling time of 10 min. These ion milling cycles where repeated until the sheet resistance reached a value around 1 k Ω at 30 °C. After that, the four spring contacts were attached to the sample and a long-term resistance measurement in high vacuum was performed. Recording the temperature is an important factor, because a slight temperature change can cause a resistance change which can otherwise not be distinguished from a change due to diffusion. Furthermore, we applied a voltage of 0.5 V to measure the resistance. It is important to remain in low voltage ranges in order to keep the ionic conduction as low as possible.

5.5.2 Results and discussion

When measuring the current at constant voltage, we found that the current constantly drops, which means that the resistance constantly rises. To keep the effect of ionic conductivity as low as possible, we performed an interval measurement. Therefore, the voltage was only applied every 15 min so the change of resistance between each measurement point has to be completely due to diffusion. The behavior of the current at room temperature can be seen in fig. 5.15. The current change is very fast at the beginning (not really obvious in the plot because of the log scale) and then slows down after several hours. At the end of this measurement, slight vibrations of the chamber caused errors in the current reading. We observed a conductivity drop of 25 – 30 % after several hours. The actual conductivity decrease started much earlier before we started the measurement. Therefore the obtained percentage is only a lower boundary. The conductivity of the STO sample is dominated by

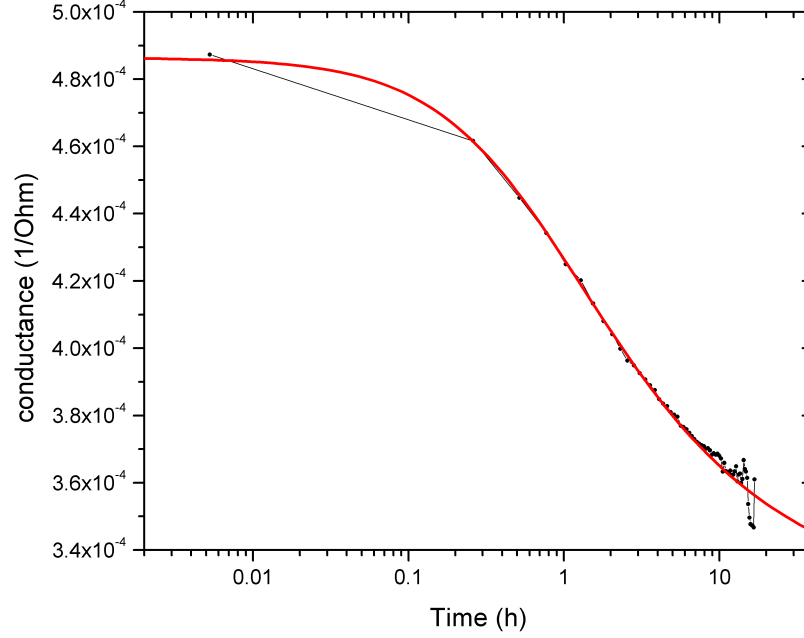


Figure 5.15: Diffusion and clustering of oxygen vacancies at room temperature. The voltage to measure the conductance was only applied every 15 min in order to prevent any effects due to ionic motion. Is mostly due to clustering of oxygen vacancies. The diffusion of vacancies deep into the sample and dropping below the critical density is rather a small contribution. The $t^{-0.5}$ fit is derived with diffusion theory.

the topmost layer where the concentration of vacancies is the highest and the most carriers are located. The diffusion causes a change of carrier distribution and weakens the vacancy concentration gradient between the surface and the bulk. Since the amount of vacancies is constant and at the beginning most of them are located on the surface, the diffusion can be described with the Gaussian distribution, derived in section 2.5.2. Over time, the highest carrier concentration will remain always at the surface, that means the main conduction occurs at $z=0$. This location has also the advantage, that the Gaussian distribution gets simplified because the exponential part vanishes (see eq.(2.29)).

However, the very first layer does not represent the behavior of the conductivity. It is the sum of all the carriers in the sample that are contributing to the conductivity. Therefore we did numerical calculations to see how the area underneath the Gaussian bell develops as a function of time. The conductivity is zero below a carrier density of roughly 10^{17} cm^{-3} , so we integrated from zero to that particular depth d_{max} (see fig. 5.16). We found that the behavior of this area over time is the same has the $t^{-0.5}$ dependence like eq.(2.29) after

the first 10 s. The absolute value differs only by a small factor. We therefore conclude that using eq.(2.29) is a good approximation to explain the behavior of fig. 5.15.

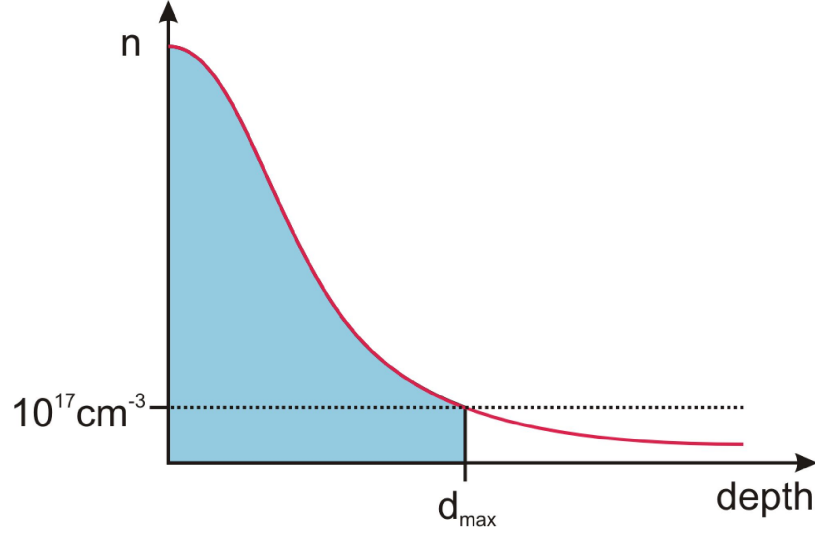


Figure 5.16: Gaussian distribution of carriers after the ion milling process. Only the carriers with a density higher than around 10^{17} cm^{-3} are contributing to the conductivity. Our numerical calculations show that the blue shaded area has also a $t^{-0.5}$ behavior. Therefore we are using eq.(2.29) as an approximation to determine the behavior of the conductance as a function of time.

Eq.(2.29) represents the carrier density as a function of time. Conversion with eq.(5.19) results in the conductance representation

$$G(t) = G_0 + \frac{\mu e N_{\text{tot}} d_0}{\sqrt{\pi D (t + t_0)}}. \quad (5.36)$$

Furthermore, we introduced a center coefficient t_0 and an offset G_0 , in order to be able to make a better fit. They also have a very important physical meaning. The factor N_{tot} is the total amount of carriers and d_0 can be considered as an effective depth. The center coefficient is necessary to consider the time delay between the end of the ion milling process and the begin of the conductance measurement. During that time, the resistance starts already to increase significantly and therefore the starting point of the measurement is when the carrier concentration is already relatively broad distributed. When fitting the measured curve, t_0 can be used to verify the lower boundary for the time which elapsed before the measurement started. It should be rather higher because the diffusion is higher after the ion milling process as the sample cools down to measurement temperatures. Because of t_0 ,

it is possible that the initial conductivity value is several factors higher than the one we measured at $t = 0$. Therefore the previous mentioned order of 25 – 30 % might be off by an order of magnitude.

As can be seen on fig. 5.15, the fit matches pretty well to the measured values. The from the fit extracted time delay t_0 is about 40 min, which is around four times the actual time delay of 8 min, but is still a good result when considering that the higher temperature enhances the conductivity drop. The fact that the resistance increases with time shows clearly, that most of the oxygen vacancies were concentrated at the surface. Furthermore it is shown, that the vacancy concentration tail of the Gaussian distribution does not contribute to the conductivity. So once the concentration density drops below the critical density of $n_c = 10^{17} \frac{1}{\text{cm}^3}$ [18], the conductivity vanishes.

Another important aspect is the observation of a very big off-set G_0 . If the decay would only due to the fact that oxygen vacancies are diffusing deep into the crystal where the concentration drops below n_c , then the conductance should drop to zero after infinite time. The fact that the conductance saturates at G_0 suggests a mechanism that maintains the conductance. We conclude that the clustering of vacancies might explain this observation. Clusters are less mobile than single oxygen vacancies and can be created easily at room temperature. So most of them remain at the surface and lead to a permanent conductivity. Therefore it can not drop to zero even after a long time. This explains the high offset in the conductance plot. The fact that the shape is proportional to $t^{-0.5}$, which originates from the thermal diffusion, confirms the suggestion which was made earlier, that the conductivity drop due to clustering has the same time dependence as the diffusion.

To understand the meaning of the product $N_{\text{tot}} d_0$ from eq.(5.36) one has to find a microscopic model that can explain the clustering. Since the clustering rate is dependent of many factors like vacancy density, time, temperature and maybe more, it is a really complex mechanism and not easy to understand. In the previous chapter we measured the carrier density ($1.8 \times 10^{18} \text{ cm}^{-3}$) of the surface and the effective depth ($2.4 \mu\text{m}$) for ion milling at room temperature with a discharge voltage of $V_D = 100 \text{ V}$. The product of them yields a carrier density per area of $4.3 \times 10^{14} \text{ cm}^{-2}$. Using this as N_{tot} and the obtained fitting parameter, we can get a rough estimation of $d_0 = 560 \text{ nm}$. The exact meaning of this value

is not clear, but we suggest it can be interpreted as a reduced depth due to clustering. In that case the clustering would decrease the depth by a factor of $\kappa = \frac{2.4 \mu\text{m}}{560 \text{ nm}} \approx 4$. This value of κ is similar to the one from the previous chapter.

To give more evidence, that the in fig. 5.15 observed behavior is due to diffusion, we performed the same measurement at low temperatures. To get the same initial conditions as for the room temperature measurement, we ion milled the STO sample until the sheet resistance was again around $1 \text{ k}\Omega$. After that, the stage was cooled with liquid nitrogen which decreased the temperature on the surface of STO to -163°C . This time the voltage remained at 0.5 V constant over the whole measurement and the current was measured every second. Fig. 5.17 shows, that this temperature was low enough, to suppress the diffusion completely. The fluctuations of the current are due to vibrations caused by the boiling liquid nitrogen in the stage. The change of resistance is smaller than roughly 5% over 17 hours.

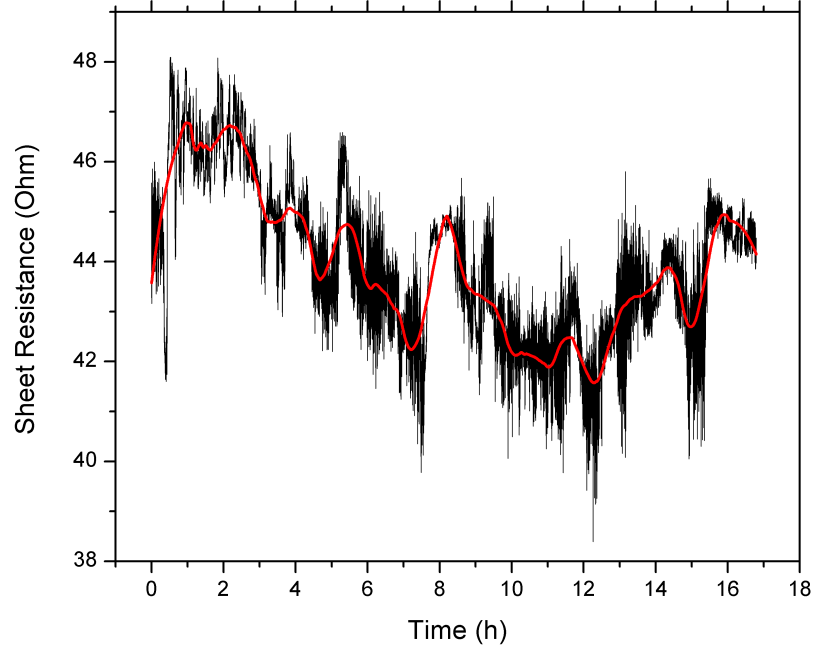


Figure 5.17: Sheet resistance of a conducting SrTiO_3 surface as a function of time at -163°C . The diffusion at low temperatures is significantly decreased which causes a lower clustering rate. Therefore the conductivity of the sample remains constant over several hours. The red line is a smoothed fit.

This is definitely a proof for the fact that thin conducting layers due to oxygen vacancies in STO diffuse at room temperature and are causing a significant change of resistance. The fluctuations during the measurements might be also due to small temperature deviations that changes the electron mobility.

5.5.3 Summary

We found that the conductivity of oxygen deficient SrTiO_3 is not constant over time. Once vacancies are introduced, they diffuse into the crystal and are able to form clusters. These clusters are contributing less carriers to the conduction band and therefore decreasing the conductivity [28]. Also vacancies can diffuse into regions where the density can drop below the critical vacancy density of $\approx 10^{17} \frac{1}{\text{cm}^3}$ [18]. A bigger impact has the effect of oxygen vacancy clustering, because these clusters are less mobile and remain on the surface. Therefore the conductivity will never drop to zero. The factor of conductivity loss was measured to be about 25 – 30 % after around 10 to 20 hours. We are assuming that the actual drop could be as high as 10 times the measured value because of the time delay between the end of the ion milling process and the begin of the measurement. We proved that the observed conductivity change is due to diffusion driven clustering because the low temperature measurement showed no change in resistivity.

We therefore can say, when making a statement about the conductivity of an oxygen vacant SrTiO_3 sample, the time delay since the creation of the vacancies is also very important. It has been assumed, that the storage in high vacuum preserves the electric properties of an oxygen deficient sample. We observed that this is not the case and even *in-situ* measurements are not always reliable.

Chapter 6

Memory Effect

Scaling microelectronics to more and more smaller sizes is one of the major demands in order to increase the the data volume of memory devices. There have been severe concerns about the future of semiconductors due to approaching the end of scalability of these materials and their charge storage capabilities. New kinds of materials, in particular perovskites, which provide the feature of bistable switching of the conductance from insulating to metallic state, are one of the candidates which might replace semiconductors in some time [48]. These devices, which are also known as resistance random access memory (ReRAM)[49], are one of the most prospective nonvolatile memories (NVM). Especially two-terminal NVMs are in special interest, because of their simple accessibility, by switching the resistance with a voltage pulse and reading the resistance with a very small bias that does not change the system [50]. Disconnecting the device has no impact on the state and it will remain over long time. The doping induced insulator-to-metal transition, and therefore localized inhomogeneities on microscopic scale, is a well known feature of titanates, zirconates or manganites [51][52][53][54]. Changing the resistance of BiFeO_3 by applying a voltage has also been reported [55]. This intrinsic behavior, the modulation of the local concentrations of oxygen, which is the origin of the special properties of the multinary oxide materials, can be used to build ReRAMs. Usually thin oxide films have been used to detect the bistable switching [56][57]. Theoretical models for these kinds of memories have already proposed [58].

SrTiO_3 itself has been also used to investigate the behavior of the memory effect [9]. Most of the studies utilized STO with dopants like chromium, to reduce the ratio between electric and ionic conductivity [3]. Without these kind of dopants, the bistable switching of resistance has only been rarely observed [9][59]. A bistable switching device has two states

which both are stable over long time, in our case, the insulating and the conducting state. This is a necessary requirement for building ReRAMS.

6.1 Sample preparation and measurement

To confirm the possibility of bistable switching in SrTiO_3 , we used two different measurement geometries and prepared our samples in two different ways. The principal setup for the first measurement is shown in fig. 6.1. The STO sample is highly conductive and has an insulating surface layer on the front. The back side is attached on a metal plate and a thin contact tip is placed on the insulating front. In our measurement, the metal plate is the copper plate of our stage which is grounded with the chamber. Silver paint between the sample and the back gate ensure a good electrical contact and the current is flowing perpendicular to the surface. Due to the charge of the oxygen vacancies, a conducting channel can be formed by applying a negative voltage on the tip. The negative oxygen ions are repelled by the electric field, which is very strong due to the small head of the contact. Once the conducting channel is formed, it can be plugged again by using a positive contact voltage. The vacancies are repelled, so the hole fills up with oxygen, and the insulating state is restored. The advantage of the back gate is its big area. The density of the electric field is much smaller than at the tip, because the field lines are homogeneously distributed over the whole area. So the field density ratio between the tip and the back gate is roughly proportional to the ratio of the contact areas.

To investigate the memory effect of STO, we also prepared different kind of samples. First, we annealed SrTiO_3 on the silicon heater stage in vacuum at different temperatures. This is a well known and the most used technique to create oxygen vacancies in the whole sample [60][9][61]. It does not destroy the surface structure (compared to conduction by ion milling) and the vacancies are homogeneously distributed. The temperature was measured directly on the surface of the sample with the tip of the thermocouple. We started at low temperatures and after each heating cycle the conduction was measured at room temperature. After 30 min at 500°C , there was no significant conduction noticeable. Keeping the sample at 600°C for the same time leads to a room temperature sheet resistance of

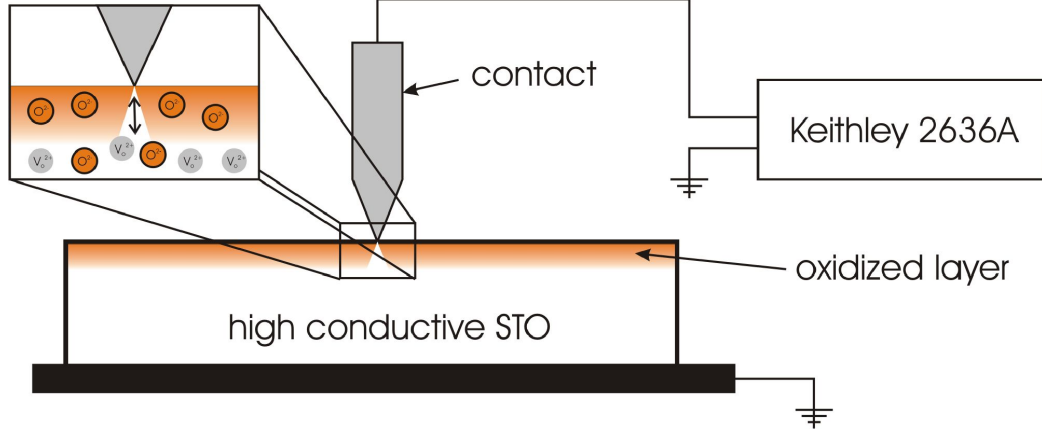


Figure 6.1: Setup of memory effect experiment. The high conductive sample is exposed to an oxygen environment for 1 hour to form an insulating layer. By applying a negative voltage at the contact with respect to the back gate, the oxygen ions are repelled and a conducting channel/path is formed (electroforming). With a negative bias voltage, the oxygen ions are attracted and the conductive hole in the surface gets plugged.

$R_{\square} = 109 \Omega$. Further heating cycles at 700°C and 770°C for similar times results in resistances of $R_{\square} = 12.5 \Omega$ and $R_{\square} = 3.3 \Omega$, respectively. We found that in this high conductive state, the usually transparent SrTiO_3 sample changed its appearance to dark blue. This is consistent with previous oxygen deficient STO studies [62][63]. Introducing oxygen into the chamber for 1 hour created an insulating layer on the top surface.

Furthermore, we used the highly conductive sample which was ion milled at high temperatures for around 20 hours. We found that the sample had the same dark blue color like the annealed one. The sheet resistance of this sample was measured *in-situ* and was about $R_{\square} = 3 \Omega$. It was capped with an oxygen layer after the ion milling process by exposing to an oxygen environment for 1 hour and the fact that the resistance even on the back side is very low makes the sample suitable for the measurement geometry shown in fig. 6.1.

So we have two highly conductive SrTiO_3 samples coated with an oxidized surface layer, but where reduced under different conditions. On one sample, the oxygen vacancies were introduced by annealing at high temperatures. On the other sample, the oxygen removal was enhanced by argon bombardment which led to the same conductance even at lower temperatures.

The other measurement configuration is more simple and is performed on the surface. The STO sample is insulated by sapphire on the copper plate and the contact is made on the surface with the contact rod. The current is flowing on the surface and not perpendicular to it. The sample was annealed at 770 °C for 30 min and has no oxidized layer and the measurement was done *in-situ*. In this setup, the electrodes are almost equal, so there is no preference which polarity leads to the conductive and which to the insulating state. This is decided by the tiny, but still decisive, asymmetry in the contact area of the contacts or by small differences of the oxygen vacancy densities underneath the contacts.

6.2 Results and discussion

6.2.1 Ion milled sample

Starting with the configuration shown in fig. 6.1 and the ion milled sample, we observed a diode behavior for low voltages. By doing a voltage sweep we obtained the plot in fig. 6.2, which shows high resistance for negative voltages and a strong increase on current for a positive bias. This behavior is due to the oxygen coating that creates a semiconducting layer. The oxidation of the surface caused a decrease of carrier concentration into the semiconducting regime. The contacts are gold coated so we created a metal-semiconductor interface which is also known as a Schottky barrier. Negative bias on the contact leads to an increased barrier height and therefore to a low conductance. Conversely, applying a positive voltage to the gold contact with respect to the back gate results in a high conductance because the barrier height is decreased.

This diode behavior can be destroyed if the voltage ranges are changed. We know that oxygen vacancies are two times positively charged and the surface layer has a lower concentration than the bulk. Applying a high negative voltage leads to the formation of a conducting channel due to repelling of oxygen from the surface into the bulk. Conversely, the accumulation of oxygen vacancies can be seen in fig. 6.3. With increasing bias, the current rises until it reaches the compliance current of 10 mA. This low resistance state is preserved even if the bias voltage is decreased. For small bias voltages, this state can be considered as an ohmic contact, because we increased the carrier concentration underneath the contact,

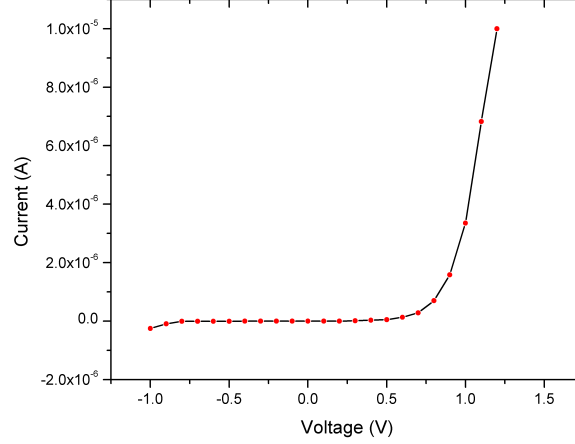


Figure 6.2: Initial IV characteristic on a high conductive STO sample with an oxidized surface. The metal-semiconductor interface (see measurement setup in fig. 6.1) shows rectifying behavior because of the increasing barrier height for negative voltage at the metal with respect to the SrTiO_3 sample.

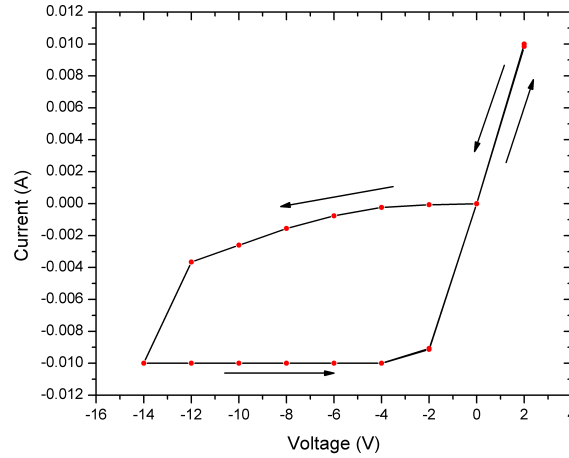


Figure 6.3: Applying a highly negative electric field attracts positively charged oxygen vacancies and therefore increases the carrier concentration. The conducting path persists after the voltage drops to zero. We set the compliance current to 10 mA.

so that the thickness carrier depletion layer at the interface dropped significantly. A low bias IV (fig. 6.4) shows the ohmic behavior and the Schottky barrier is barely visible. This conducting state can be switched back to the insulating state, by applying a positive voltage. Going back and forth, from highly negative to highly positive voltages, exhibits a permanent switching between the two states. A semi logarithmic plot of the absolute current versus the bias voltage can be seen in fig. 6.5. An IV measurement like this

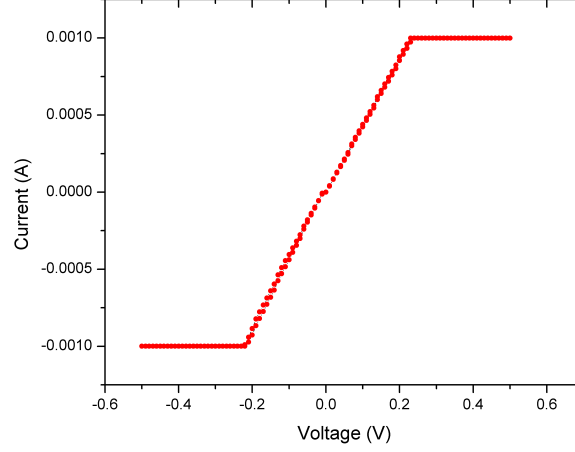


Figure 6.4: After forming a conducting path on the surface of the oxidized sample by applying a high negative voltage, the Schottky barrier vanishes which leads to an ohmic behavior for low voltages. Without creating high electric fields, this state will remain over really long times. The compliance current is set to 10 mA.

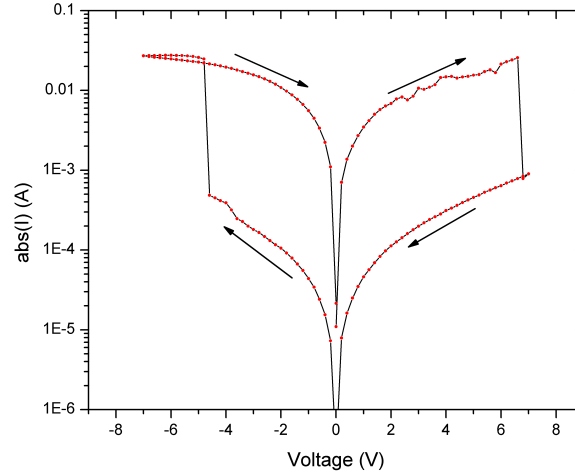


Figure 6.5: Memory effect on oxygen deficient SrTiO_3 . Reaching a certain positive or negative threshold bias voltage leads to a sudden increase or decrease of resistance, respectively. Below this threshold voltage, the system does not change. It is noted, that the resistance difference between the two states is almost two orders of magnitudes. The asymmetry of the plot can be explained by the fact that attracting the vacancies is easier than repelling them.

was reproducible over many sweeps with almost the same shape. We observed a significant difference in resistance between the two states (two orders of magnitudes). This means, it is fairly easy to detect the present resistance state by using a small bias voltage.

Another interesting fact is that the threshold voltage for an increase or decrease of resistance is not the same. The voltage for the drop is about 1.4 times bigger than the voltage needed to create the conductive state. This can be explained by the distance of the oxygen ions for each case. To get from insulating to conducting, the oxygen ions are directly underneath the contact where the electric field is strong ($\propto \frac{1}{r^2}$). That means that the electric force on these ions is also very high. Conversely, if there is a conducting path and the voltage is positive, the electric field has to reach into the bulk to attract the oxygen ions, in order to seal the channel. The greater distance causes a higher voltage needed to reach the insulating state again.

By installing a tungsten filament in the stage, we were able to heat up the stage and investigated the behavior of the threshold voltage at different temperatures. To get a better accuracy, we performed 20 sweeps and took the average of all the threshold voltages. In fig. 6.6 we show the multiple sweeps of the sample at 100 °C. Each loop has hysteresis behavior, but the resistance of the conducting state (red arrows) and the insulating state (blue arrows) is not always the same. Therefore the amount of vacancies or oxygen ions is not always the same after each loop. Furthermore is the positive threshold more confined than the negative one. By threshold voltage we refer to the critical voltage that leads to a jump from insulating to conducting state (+) and vice versa (-). We found that the threshold voltage \bar{V}_{+-} ,

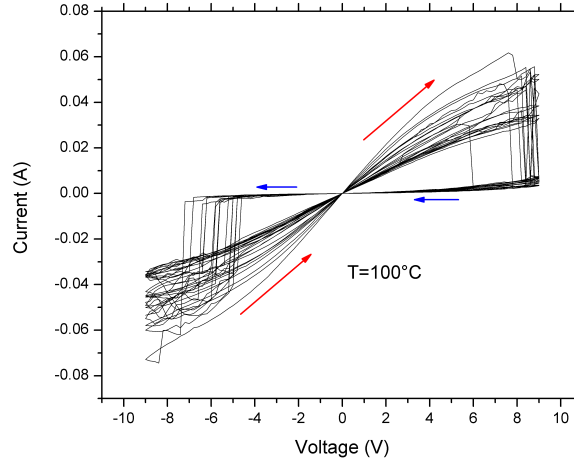


Figure 6.6: The hysteresis behavior for 20 loops is shown at 100 °C. Each sweep followed the hysteresis behavior which shows the consistency of this effect. The positive threshold is higher and more defined than the negative one.

which is the mean of the average threshold voltages \bar{V}_+ and \bar{V}_- , is dropping with increasing temperature. In fig. 6.7 we show the dependence of \bar{V}_{+-} as a function of temperature. The big error bars can be explained by the fact that the threshold voltage is not well confined for each hysteresis loop. But the overall trend to lower voltages with higher temperature supports the picture of the oxygen vacancy migration. The diffusion coefficient D (see eq. (2.18)) scales exponentially with temperature, so at 200 °C the vacancies are more mobile than at room temperature. This means the electric field strength can be smaller in order to switch from on state to the other.

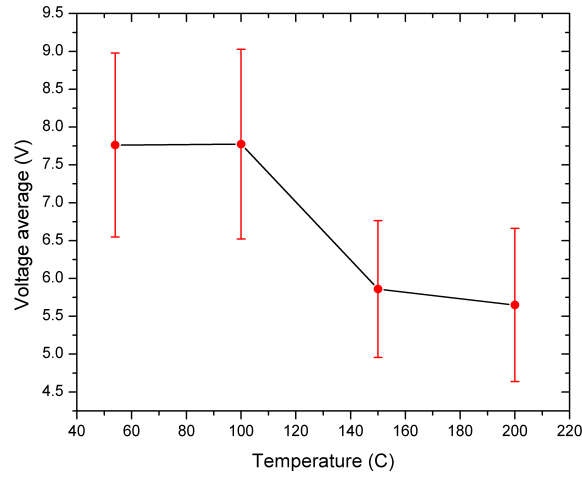


Figure 6.7: The tendency of the threshold voltage to drop with higher temperature gives evidence for the oxygen vacancy migration model to explain the bistable switching behavior of oxygen deficient SrTiO_3 . Higher temperatures enhance the diffusion of oxygen vacancies which makes them easier to move under the influence of an electric field.

6.2.2 Annealed sample

As mentioned before, we also prepared a sample by annealing at high temperatures with the same sheet resistance as the ion milled sample. Also oxidized in oxygen atmosphere, we have two electrically identical samples, which differed only by the preparation process. Using the measurement configuration as shown in fig. 6.1, we obtained a similar diode behavior as with the ion milled sample (see fig. 6.8). The only difference is the much faster increase of current with increasing bias voltage. Therefore the barrier height seems to be much smaller than for the ion milled sample. Applying a negative bias on the contact with

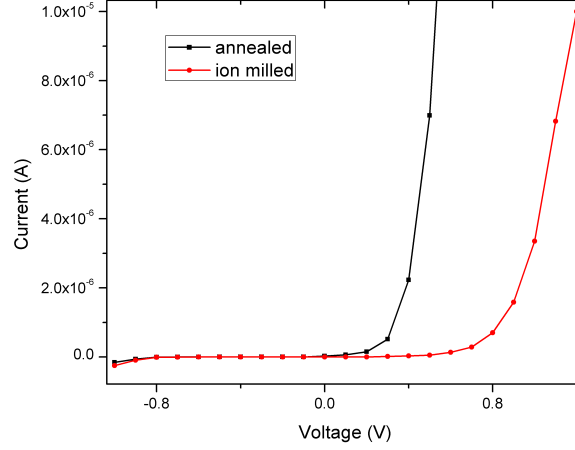


Figure 6.8: Comparison between two different Schottky barriers. Both samples have an oxidized layer which has semiconducting behavior. The current in the annealed sample increases much faster with increasing bias voltage than the ion milled sample. Therefore the Schottky barrier of the ion milled sample is smaller than for the annealed one.

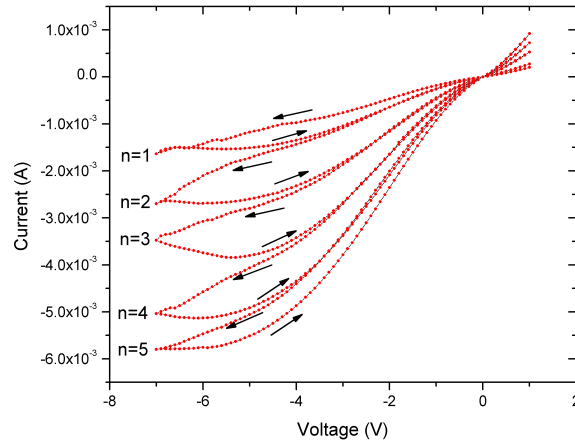


Figure 6.9: Forming a conductive path through the oxidized surface of annealed SrTiO_3 . After each sweep the conductance increases, because each time more vacancies are attracted underneath the contact.

respect to the back gate, we were able to form a conductive path. In fig. 6.9 we show how the channel increases its conductance with each sweep. However, bringing the sample back into the insulating state was not possible. It is easier to form the conductive state from the insulating state, because the current during the forming is low compared to the case when the path is conducting. Increasing the positive voltage might lead to very high currents. Even currents as high as 0.5 A and a bias of 10 V couldn't restore the insulating state. The reason for that might be less mobile oxygen vacancies. The annealed sample was exposed to

770 °C, so the diffusion rate was extremely high. Therefore the chances of oxygen vacancy clustering are much higher than for the sample which was ion milled ($T_{\max} \approx 300$ °C). It is known, that when two oxygen vacancies are combined into a cluster, each vacancy only contributes one electron to the conduction instead of two. Furthermore, clustered vacancies are less mobile because they try to stick together and therefore constrain each other to jump to another site [30]. Both samples have the same conductivity, so we conclude that the ion milled sample has less vacancies, but also less vacancy cluster. That might be the reason for the fact that we weren't able to switch between the conducting and the insulating state.

Surface memory effect

We were also able to measure the memory effect in the surface of the sample. The measurement setup is described in fig. 6.10. The sample was annealed in high vacuum and had a 4 probe sheet resistance of $R_{\square,4P} = 12.5 \Omega$. Due to the small contact area, the two probe resistance was several orders of magnitude higher. We measured therefore $R_{2P} = 25 \text{ k}\Omega$.

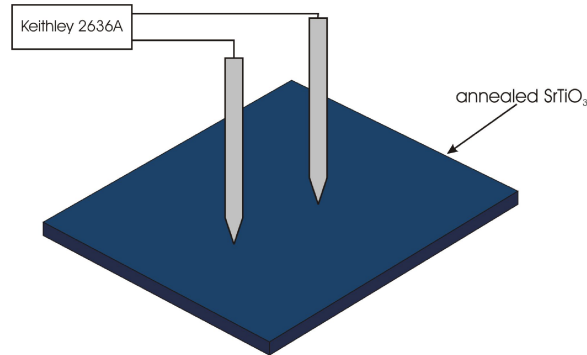


Figure 6.10: Experimental setup for measuring the memory effect on the surface of annealed SrTiO_3 . Depending on slight asymmetries at the tip of the contacts, the ions will move underneath the probe with the smaller area.

By increasing the voltage up to 10 V we observed a sudden jump to a higher current. Doing a complete sweep between -10 to 10 V brought the current back to the original value. The hysteresis behavior is shown in fig. 6.11. The shape was similar to the previous measurements in a different geometry on the ion milled sample. We assume that this behavior is also due to oxygen vacancies and their migration underneath the contacts. The movement of the vacancies, which can be considered as ionic conduction, can only occur in very high

electric fields. With eq. (2.32) we can make a rough estimation of this current due to ionic motion. The vacancy density can be estimated from the conductance and the thickness of the SrTiO_3 sample, assuming a homogeneous distribution of vacancies. This should be reasonable considering that the sample was annealed at high temperatures, so the vacancies were able to fill out the whole sample. Furthermore are the assumptions for the sheet resistance, which were made for eq. (4.1), still valid. That is, the sample can be still considered as thin even though it is macroscopic. With eq. (5.19) and a sample thickness of 0.05 cm we find a carrier density of

$$n = 4.0 \times 10^{17} \frac{1}{\text{cm}^3}. \quad (6.1)$$

The amount of oxygen vacancies is probably much higher but not contributing to the conductivity due to a lot of clustering. The uniform deep dark blue color confirms this conclusion. With the above calculated carrier density and using $2e$ for the electron charge because of two times charge oxygen vacancies, we find a minimum ionic conductivity of

$$\sigma_{\text{ionic}} = 4.9 \times 10^{-12} \frac{1}{\Omega \text{ cm}}. \quad (6.2)$$

This small conductivity explains why there is only ionic motion right underneath the electrodes.

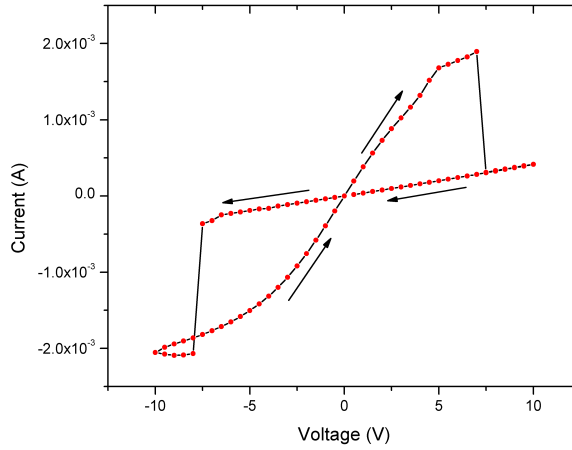


Figure 6.11: Hysteresis effect on the surface of vacuum annealed SrTiO_3 . The difference between the high and low conducting state is around one order of magnitude and therefore only half of the difference on the ion milled sample.

The main difference between this measurement and the previous ones perpendicular to the surface is the not pre-defined asymmetry of the contacts. Both contacts have the same

shape, so the electric field density is similar. Slight microscopic differences determine on which contact the oxygen vacancy attraction occurs. When measuring the sudden current increase, the electrode with the negative potential is the one with the smaller contact area. Underneath it is where the vacancies are gathered from the bulk so its contact resistance drops which leads to a current increase. On the other electrode, the field density is too weak due to a tiny difference in the contact shape. Therefore it can not move the vacancies as easy as the other electrode.

In this configuration, we were able to switch between the low conducting and high conducting state (LCS/HCS). By applying a short 8 V-pulse of less than one second can change the state depending on the polarity. This voltage is high enough to switch between the two states. The reading of the state occurred by measuring with a voltage of 1 V, small enough to leave the system in its state. Fig. 6.12 shows that the switching between the LCS and the HCS. The resistance in each state was reliable and constant over many cycles. Due to the difference of one order of magnitude, the states are easy to distinguish. The sheet resistance remained constant during the switching process which is another proof that the resistance change is underneath the contacts.

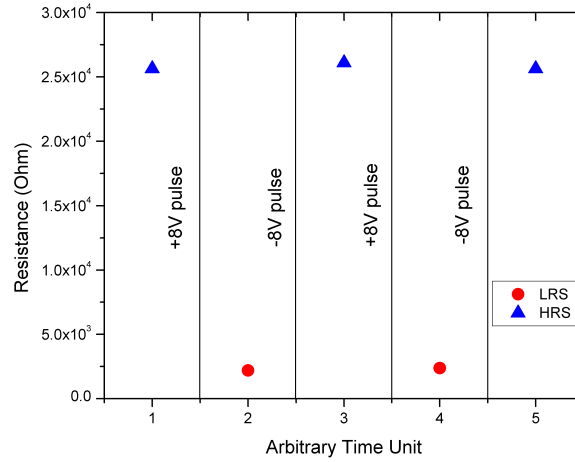


Figure 6.12: Switching between LCS and HCS. The resistance was measured with 1 V in order to maintain the state. Applying 8 V changes the state depending on the polarity. The states remain constant over time and are reliable after many switching cycles.

6.2.3 Summary

In conclusion, we were able to show that oxygen deficient SrTiO_3 can be used as a memory device in various geometries. The movement of oxygen vacancies due to the appliance of an electric field, can change the conductive properties significantly. So far, there have been no reports of memory effects in macroscopic scales without any dopants besides vacancies. We found that annealed samples show less switching capabilities at lower carrier densities, which might be related to the higher amount of vacancy clusters which are less mobile [30]. Therefore they require higher electric fields in order to migrate which might end up in to high electric currents. Since thermal annealing in high vacuum is the common way to introduce oxygen vacancies into stoichiometric SrTiO_3 , this might be the reason why there have been no reports so far. However, we observed the memory effect on the surface of an annealed sample with high carrier density. The difference between the high and low conductive states remained constant after many switching cycles.

An even higher difference between the two states was found on an ion milled sample. The conductivity changed at a critical voltage about two orders of magnitude. The temperature dependent measurements for the critical voltage showed a drop with increasing temperature. This effect is due to the enhanced diffusion rate of the oxygen vacancies, which are more easily to move. We suggest that the difference between the annealed and the ion milled sample is due to different amounts of oxygen vacancy clusters. Even though the sheet resistance was the same, the vacancies could not be moved with the same voltage. The clustering rate of the annealed sample was significantly increased while it was exposed to much higher temperatures than the ion milled sample. We therefore conclude, that amount of clusters has a severe impact on the ability of memory devices based on oxygen vacancies. Creating the vacancies, keeping the cluster rate as low as possible and therefore maintain a high vacancy mobility is the key to an effective resistive memory. Ionic bombardment might be the procedure to create these devices.

References

- [1] J. F. Schooley, W. R. Hosler, and M. L. Cohen, “Superconductivity in Semiconducting SrTiO_3 ,” *Phys. Rev. Lett.* **12** (Apr, 1964) 474–475.
- [2] K. van Benthem, C. Elsässer, and R. H. French, “Bulk electronic structure of SrTiO_3 : Experiment and Theory,” *Journal of Applied Physics* **90** (2001) no. 12, 6156–6164. <http://link.aip.org/link/?JAP/90/6156/1>.
- [3] Y. Watanabe, J. G. Bednorz, A. Bietsch, C. Gerber, D. Widmer, A. Beck, and S. J. Wind, “Current-driven insulator–conductor transition and nonvolatile memory in chromium-doped SrTiO_3 single crystals,” *Applied Physics Letters* **78** (2001) no. 23, 3738–3740. <http://link.aip.org/link/?APL/78/3738/1>.
- [4] D. A. Muller, N. Nakagawa, A. Ohtomo, J. L. Grazul, and H. Y. Hwang, “Highly conductive nanolayers on strontium titanate produced by preferential ion-beam etching,” *Nat. Mat.* **430** (2004) 657 – 661.
- [5] T. Fujii, M. Kawasaki, A. Sawa, H. Akoh, Y. Kawazoe, and Y. Tokura, “Hysteretic current–voltage characteristics and resistance switching at an epitaxial oxide Schottky junction $\text{SrRuO}_3/\text{SrTi}_{0.99}\text{Nb}_{0.01}\text{O}_3$,” *Applied Physics Letters* **86** (2005) no. 1, 012107. <http://link.aip.org/link/?APL/86/012107/1>.
- [6] R. Perez-Casero, J. Perrière, A. Gutierrez-Llorente, D. Defourneau, E. Millon, W. Seiler, and L. Soriano, “Thin films of oxygen-deficient perovskite phases by pulsed-laser ablation of strontium titanate,” *Physical Review B (Condensed Matter and Materials Physics)* **75** (2007) no. 16, 165317. <http://link.aps.org/abstract/PRB/v75/e165317>.
- [7] J. Son, J. Cagnon, and S. Stemmer, “Electrical properties of epitaxial SrTiO_3 tunnel barriers on (001) Pt/SrTiO_3 substrates,” *Applied Physics Letters* **94** (2009) no. 6, 062903. <http://link.aip.org/link/?APL/94/062903/1>.
- [8] T. Sato, K. Shibuya, T. Ohnishi, K. Nishio, and M. Lippmaa, “Fabrication of SrTiO_3 Field Effect Transistors with $\text{SrTiO}_{3-\delta}$ Source and Drain Electrodes,” *Japanese Journal of Applied Physics* **46** (2007) no. 21, L515–L518. <http://jjap.ipap.jp/link?JJAP/46/L515/>.
- [9] K. Szot, W. Speier, G. Bihlmayer, and R. Waser, “Switching the electrical resistance of individual dislocations in single-crystalline SrTiO_3 ,” *Nat. Mat.* **5** (2006) 312 – 320.
- [10] V. V. Zhirnov and R. K. Cavin, “Nanodevices: Charge of the heavy brigade,” *Nat. Nano* **3** (2008) 377 – 378.
- [11] P. A. Cox, *Transition Metal Oxides, An Introduction to their Electronic Structure and Properties*. Oxford Science Publications, 1992.

- [12] A. Kalabukhov, R. Gunnarsson, J. Börjesson, E. Olsson, T. Claeson, and D. Winkler, “Effect of oxygen vacancies in the SrTiO₃ substrate on the electrical properties of the LaAlO₃/SrTiO₃ interface,” *Physical Review B (Condensed Matter and Materials Physics)* **75** (2007) no. 12, 121404.
<http://link.aps.org/abstract/PRB/v75/e121404>.
- [13] R. E. Crandall and J. F. Delord, “The potential within a crystal lattice,” *Journal of Physics A: Mathematical and General* **20** (1987) no. 9, 2279–2292.
<http://stacks.iop.org/0305-4470/20/2279>.
- [14] T. Wolfram and S. Ellialtioglu, “Electronic and Optical Properties of d-Band Perovskites,”.
- [15] D. Ricci, G. Bano, G. Pacchioni, and F. Illas, “Electronic structure of a neutral oxygen vacancy in SrTiO₃,” *Phys. Rev. B* **68** (Dec, 2003) 224105.
- [16] N. F. MOTT, “Metal-Insulator Transition,” *Rev. Mod. Phys.* **40** (Oct, 1968) 677–683.
- [17] W. Wunderlich, H. Ohta, and K. Koumoto, “Enhanced effective mass in doped SrTiO₃ and related perovskites,” *PHYSICA B* **404** (2009) 2202.
[doi:10.1016/j.physb.2009.04.012](https://doi.org/10.1016/j.physb.2009.04.012).
- [18] O. N. Tufte and P. W. Chapman, “Electron Mobility in Semiconducting Strontium Titanate,” *Phys. Rev.* **155** (Mar, 1967) 796–802.
- [19] Y. Tokura, Y. Taguchi, Y. Okada, Y. Fujishima, T. Arima, K. Kumagai, and Y. Iye, “Filling dependence of electronic properties on the verge of metal Mott-insulator transition in Sr_{1-x}La_xTiO₃,” *Phys. Rev. Lett.* **70** (Apr, 1993) 2126–2129.
- [20] C. S. Koonce, M. L. Cohen, J. F. Schooley, W. R. Hosler, and E. R. Pfeiffer, “Superconducting Transition Temperatures of Semiconducting SrTiO₃,” *Phys. Rev.* **163** (Nov, 1967) 380–390.
- [21] W. Luo, W. Duan, S. G. Louie, and M. L. Cohen, “Structural and electronic properties of *n* -doped and *p* -doped SrTiO₃ ,” *Phys. Rev. B* **70** (Dec, 2004) 214109.
- [22] P. Calvani, M. Capizzi, F. Donato, S. Lupi, P. Maselli, and D. Peschiaroli, “Observation of a midinfrared band in SrTiO_{3-y},” *Phys. Rev. B* **47** (Apr, 1993) 8917–8922.
- [23] M. Imada, A. Fujimori, and Y. Tokura, “Metal-insulator transitions,” *Rev. Mod. Phys.* **70** (Oct, 1998) 1039–1263.
- [24] E. Choi, J. Kim, D. Cuong, and J. Lee, “Oxygen vacancies in SrTiO₃,”.
- [25] H. Cai, X. Wu, and J. Gao, “Effect of oxygen content on structural and transport properties in SrTiO_{3-x} thin films,” *Chemical Physics Letters* **467** (2009) no. 4-6, 313 – 317. <http://www.sciencedirect.com/science/article/B6TFN-4V2HJNK-1/2/e65f3168e3d80a192d37dfb8d55acb28>.
- [26] D. Kan, O. Sakata, S. Kimura, M. Takano, and Y. Shimakawa, “Structural Characterization of Ar⁺-Irradiated SrTiO₃ Showing Room-Temperature Blue Luminescence,” *Japanese Journal of Applied Physics* **46** (2007) no. 19, L471–L473.
<http://jjap.ipap.jp/link?JJAP/46/L471/>.

- [27] R. Astala and P. D. Bristowe, “Ab initio and classical simulations of defects in SrTiO_3 ,” *Computational Materials Science* **22** (2001) no. 1-2, 81 – 86.
<http://www.sciencedirect.com/science/article/B6TWM-440BMW0-H/2/5bb84f560cf8eaef24d28226fc566916>.
- [28] N. Shanthi and D. D. Sarma, “Electronic structure of electron doped SrTiO_3 : $\text{SrTiO}_{3-\delta}$ and $\text{Sr}_{1-x}\text{La}_x\text{TiO}_3$,” *Phys. Rev. B* **57** (Jan, 1998) 2153–2158.
- [29] W. Gong, H. Yun, Y. B. Ning, J. E. Greedan, W. R. Datars, and C. V. Stager, “Oxygen-deficient SrTiO_{3-x} , $X = 0.28, 0.17$, and 0.08 . Crystal growth, crystal structure, magnetic, and transport properties,” *Journal of Solid State Chemistry* **90** (1991) no. 2, 320 – 330. <http://www.sciencedirect.com/science/article/B6WM2-4B6NDF6-41/2/80fda3bf387d4a92e5a612f4609fa9ad>.
- [30] D. D. Cuong, B. Lee, K. M. Choi, H.-S. Ahn, S. Han, and J. Lee, “Oxygen Vacancy Clustering and Electron Localization in Oxygen-Deficient SrTiO_3 : LDA + U Study,” *Physical Review Letters* **98** (2007) no. 11, 115503.
<http://link.aps.org/abstract/PRL/v98/e115503>.
- [31] M. Cherry, M. S. Islam, and C. R. A. Catlow, “Oxygen Ion Migration in Perovskite-Type Oxides,” *Journal of Solid State Chemistry* **118** (1995) no. 1, 125 – 132. <http://www.sciencedirect.com/science/article/B6WM2-45S96C4-N/2/2bcba06c624e400bd5af10f2d213ba9a>.
- [32] F. Cordero, “Hopping and clustering of oxygen vacancies in SrTiO_3 ,” *Materials Science and Engineering: A* **521-522** (2009) 77 – 79.
<http://www.sciencedirect.com/science/article/B6TXD-4VT0X5D-12/2/8bbbf25f8d670edf7bf4a524779c5711>. 15th International Conference on Internal Friction and Mechanical Spectroscopy.
- [33] V. E. Henrich, G. Dresselhaus, and H. J. Zeiger, “Surface defects and the electronic structure of SrTiO_3 surfaces,” *Phys. Rev. B* **17** (Jun, 1978) 4908–4921.
- [34] D. W. Reagor and V. Y. Butko, “Highly conductive nanolayers on strontium titanate produced by preferential ion-beam etching,” *Nat. Mat. Lett.* **4** (2005) 593 – 596.
- [35] D. Neamen, *Semiconductor Physics And Devices*. McGraw-Hill Science/Engineering/Math, 2002.
- [36] J. Crank, *The Mathematics of Diffusion*. Oxford University Press, 1975.
- [37] P. Pasierb, S. Komornicki, and M. Rekas, “Comparison of the chemical diffusion of undoped and Nb-doped SrTiO_3 ,” *Journal of Physics and Chemistry of Solids* **60** (1999) no. 11, 1835 – 1844. <http://www.sciencedirect.com/science/article/B6TXR-3XH3V1H-C/2/4902b1b5aab843be55372a2cf9c3066c>.
- [38] H. Mehrer, *Diffusion in Solids: Fundamentals, Methods, Materials, Diffusion-Controlled Processes*. Springer, 2007.
- [39] H. R. Kaufman, R. S. Robinson, and R. I. Seddon, “End-Hall ion source,” *J. Vac. Sci. Technol. A* **5** (Jul/Aug, 1987) 2081–2084.
<http://scitation.aip.org/getpdf/servlet/GetPDFServlet?filetype=pdf&id=JVTAD6000005000004002081000001&idtype=cvips>.

- [40] H. R. Kaufman and R. S. Robinson, “End-Hall ion source,” *Patent Application* (August, 1989) . <http://www.freepatentsonline.com/4862032.html>.
- [41] D. K. Schroder, *Semiconductor Material and Device Characterization*. Wiley-IEEE Press, 2006.
- [42] F. Smith, “Measurement of Sheet Resistivities with the four-point probe,” *Bell Labs Technical Journal* **37** (1957) 711–718.
- [43] M. Yamashita and M. Agu, “Geometrical Correction Factor for Semiconductor Resistivity Measurements by Four-Point Probe Method,” *Japanese Journal of Applied Physics* **23** (1984) no. Part 1, No. 11, 1499–1504. <http://jjap.ipap.jp/link?JJAP/23/1499/>.
- [44] H. Q. Li, R. H. Ono, L. R. Vale, D. A. Rudman, and S. H. Liou, “A novel multilayer circuit process using $\text{YBa}_2\text{Cu}_3\text{O}_x/\text{SrTiO}_3$ thin films patterned by wet etching and ion milling,” *Applied Physics Letters* **69** (1996) no. 18, 2752–2754. <http://link.aip.org/link/?APL/69/2752/1>.
- [45] J. M. E. Harper, J. J. Cuomo, and H. R. Kaufman, “Technology and applications of broad-beam ion sources used in sputtering. Part II. Applications,” *Journal of Vacuum Science and Technology* **21** (1982) no. 3, 737–756. <http://link.aip.org/link/?JVS/21/737/1>.
- [46] J. E. House, *Inorganic Chemistry*. Academic Press, 2008.
- [47] H. P. R. Frederikse and W. R. Hosler, “Hall Mobility in SrTiO_3 ,” *Phys. Rev.* **161** (Sep, 1967) 822–827.
- [48] A. Kingon, “Perovskites: Is the ultimate memory in sight?,” *Nat. Mat.* **5** (2006) 251 – 252.
- [49] A. Sawa, “Resistive switching in transition metal oxides,” *Materials Today* **11** (2008) no. 6, 28 – 36. <http://www.sciencedirect.com/science/article/B6X1J-4SJJ2PJ-N/2/b76063f509d65a516c5d6e482b04dcd3>.
- [50] M. J. Rozenberg, I. H. Inoue, and M. J. Sánchez, “Nonvolatile Memory with Multilevel Switching: A Basic Model,” *Phys. Rev. Lett.* **92** (Apr, 2004) 178302.
- [51] R. Dong, D. S. Lee, M. B. Pyun, and M. Hasan, “Mechanism of current hysteresis in reduced rutile TiO_2 crystals for resistive memory,” *Applied Physics A Materials Science and Processing* **93** (2008) no. 2, 409–414. <http://www.springerlink.com/content/815051880622k514>.
- [52] J. R. Jameson, Y. Fukuzumi, Z. Wang, P. Griffin, K. Tsunoda, G. I. Meijer, and Y. Nishi, “Field-programmable rectification in rutile TiO_2 crystals,” *Applied Physics Letters* **91** (2007) no. 11, 112101. <http://link.aip.org/link/?APL/91/112101/1>.
- [53] P. Maksymovych, S. Jesse, P. Yu, R. Ramesh, A. P. Baddorf, and S. V. Kalinin, “Polarization Control of Electron Tunneling into Ferroelectric Surfaces,” *Science* **324** (2009) no. 5933, 1421–1425, <http://www.sciencemag.org/cgi/reprint/324/5933/1421.pdf>. <http://www.sciencemag.org/cgi/content/abstract/324/5933/1421>.

- [54] A. Sawa, T. Fujii, M. Kawasaki, and Y. Tokura, “Hysteretic current–voltage characteristics and resistance switching at a rectifying Ti/Pr_{0.7}Ca₃MnO₃ interface,” *Applied Physics Letters* **85** (2004) no. 18, 4073–4075. <http://link.aip.org/link/?APL/85/4073/1>.
- [55] C.-H. Yang, J. Seidel, S. Y. Kim, P. B. Rossen, and P. e. a. Yu, “Electric modulation of conduction in multiferroic Ca-doped BiFeO₃ films,” *Nat. Mat.* **8** (2009) 485 – 493.
- [56] A. Beck, J. G. Bednorz, C. Gerber, C. Rossel, and D. Widmer, “Reproducible switching effect in thin oxide films for memory applications,” *Applied Physics Letters* **77** (2000) no. 1, 139–141. <http://link.aip.org/link/?APL/77/139/1>.
- [57] A. Sawa, T. Fujii, M. Kawasaki, and Y. Tokura, “Interface resistance switching at a few nanometer thick perovskite manganite active layers,” *Applied Physics Letters* **88** (2006) no. 23, 232112. <http://link.aip.org/link/?APL/88/232112/1>.
- [58] D. B. Strukov, G. S. Snider, D. R. Stewart, and R. S. Williams, “The missing memristor found,” *Nature* **453** (2008) 80 – 83.
- [59] R. Waser and M. Aono, “Nanoionics-based resistive switching memories,” *Nat. Mat. Rev.* **6** (2007) 833 – 840.
- [60] K. Szot, W. Speier, R. Carius, U. Zastrow, and W. Beyer, “Localized Metallic Conductivity and Self-Healing during Thermal Reduction of SrTiO₃,” *Phys. Rev. Lett.* **88** (Feb, 2002) 075508.
- [61] G. I. Meijer, U. Staub, M. Janousch, S. L. Johnson, B. Delley, and T. Neisius, “Valence states of Cr and the insulator-to-metal transition in Cr-doped *SrTiO*₃,” *Phys. Rev. B* **72** (Oct, 2005) 155102.
- [62] H. D. Hwang, “Oxygen vacancies shine blue,” *Nat. Mat.* **4** (2005) 803 – 804.
- [63] J. Mannhart and D. G. Schlom, “The value of seeing nothing,” *Nature* **430** (2006) 620 – 621.

Appendix A

Drawings

The drawings of the customized parts for the vacuum chamber can be seen here.

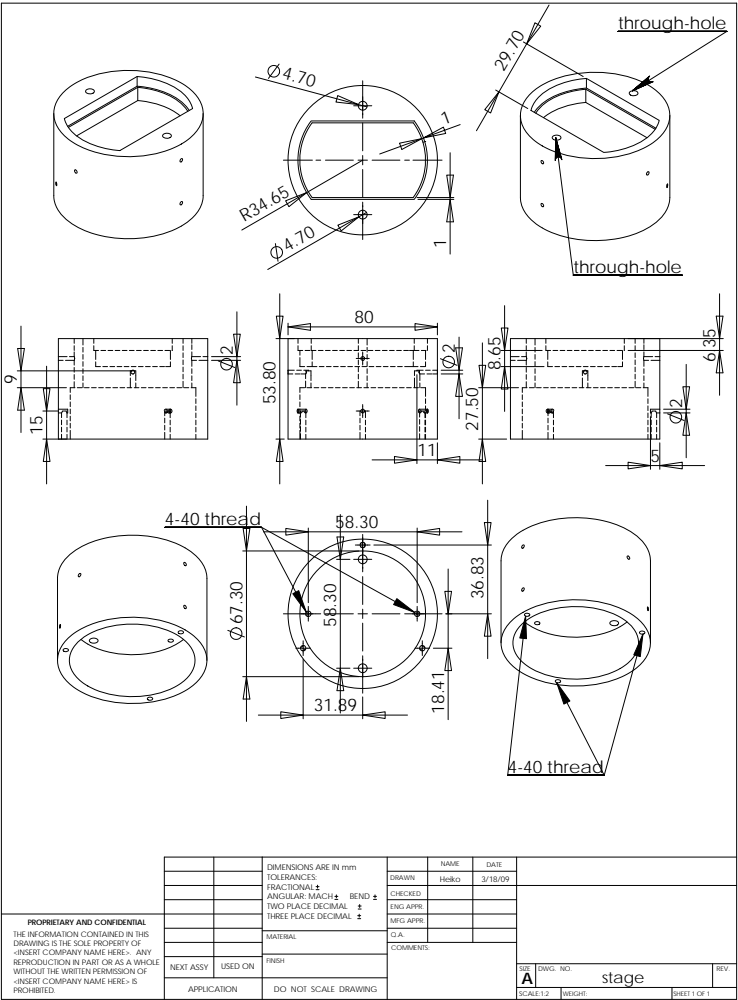


Figure A.1: Drawing of sample stage.

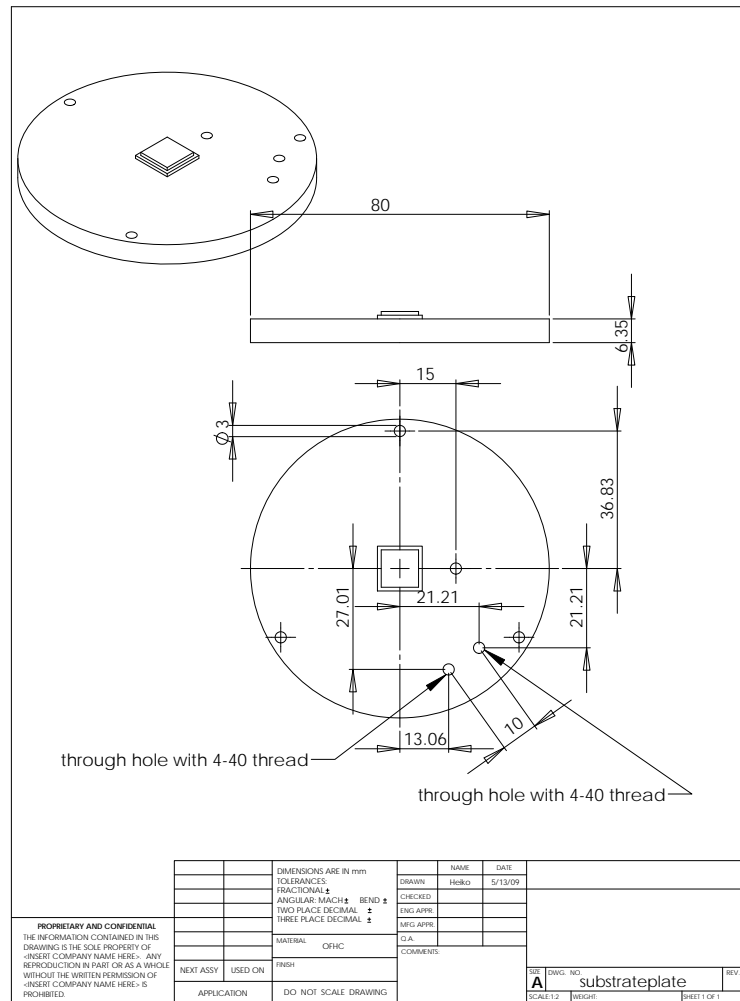


Figure A.2: Drawing of substrate plate which is located underneath the stage.

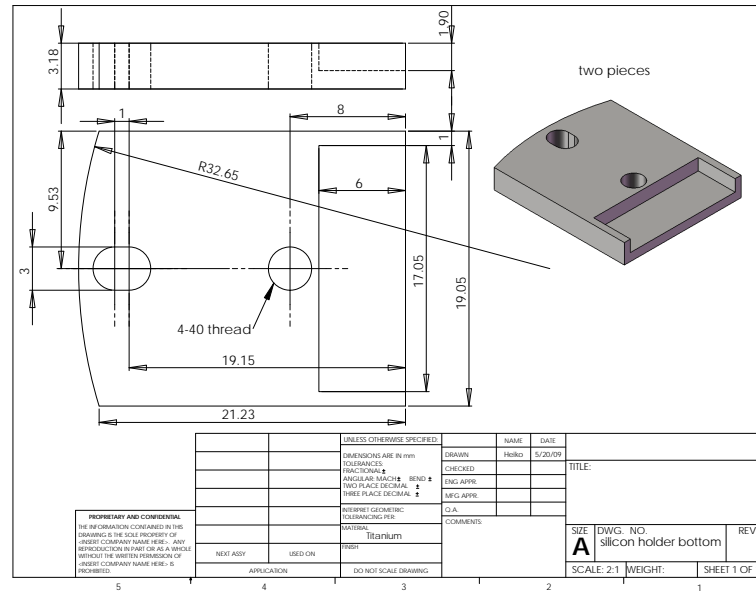


Figure A.3: Drawing of the bottom titanium piece to hold the silicon heater.

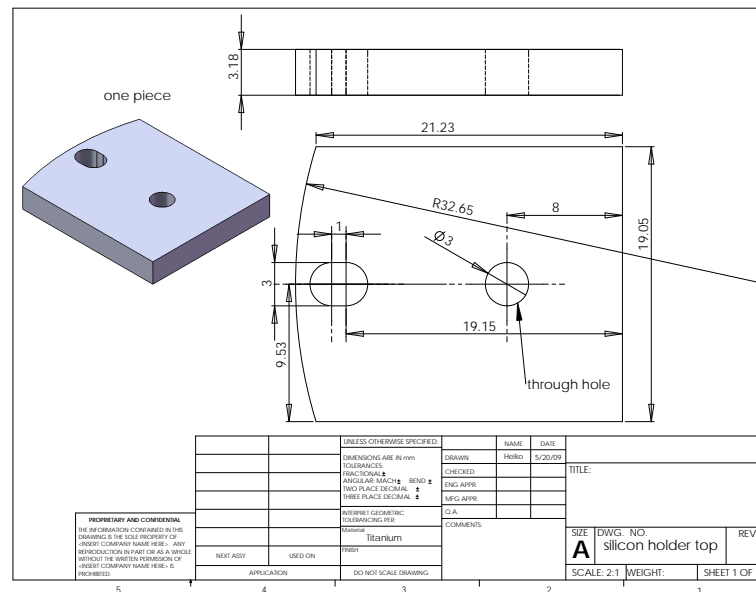


Figure A.4: Drawing of the top titanium piece to hold the silicon heater.

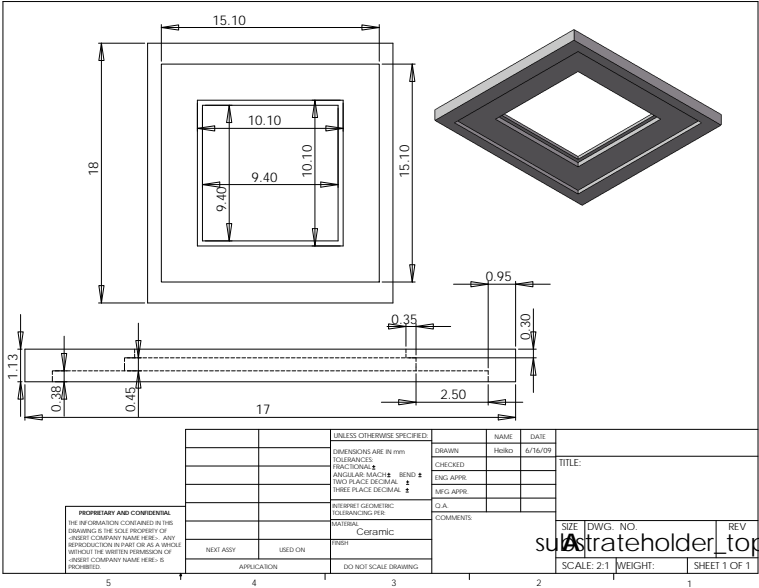


Figure A.5: Drawing of bottom ceramic piece.

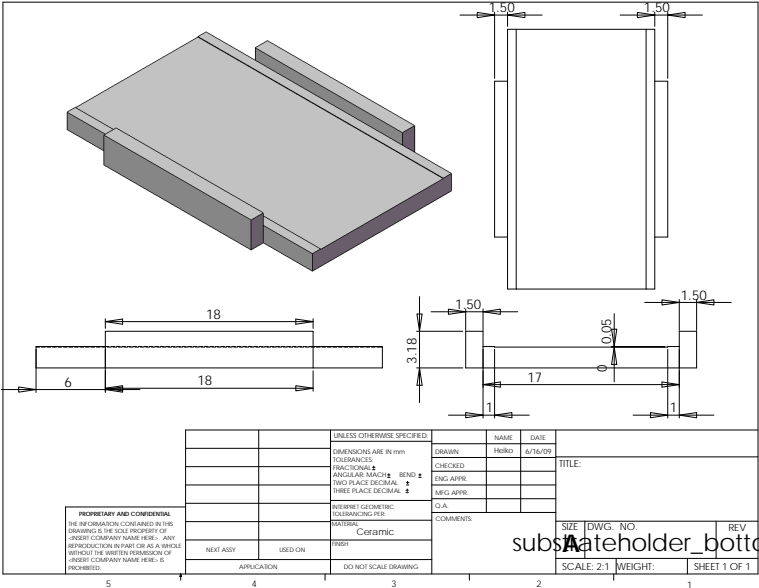


Figure A.6: Drawing of top ceramic piece.